Multi-lined Interferometric Stellar Oscillation Spectrometer *(MISOS)*

Christopher Robert Bell, B.Sc. A.R.C.S. M.Sc.

Blackett Laboratory, Imperial College of Science, Technology and Medicine, Prince Consort Road, London SW7 2BZ.

A thesis presented to the University of London
for the degree of Doctor of Philosophy
and to Imperial College of Science, Technology and Medicine
for the Diploma of Membership.

May 1991

Abstract

Imperial College Astrophysics Group have previously developed two radial velocity interferometers for detecting stellar oscillations, one based on a Michelson interferometer, and the other on a Fabry-Perot interferometer. They have both been shown to be photon shot noise limited.

This thesis describes a way of improving them both by enabling either of them to use many spectral lines. This was done by pre-dispersing the stellar spectrum, using an echelle spectrometer, and isolating the individual absorption lines using optical fibres. Then by feeding the individual lines into the interferometer, (set to a fixed gap/path difference), at the correct off-axis angle, all the lines could be transmitted simultaneously.

The design, manufacture/conversion and testing of both versions are discussed, with particular reference to the Fabry-Perot, and their problems highlighted. Preliminary tests on the Sun are shown. Their relative advantages are discussed, and suggestions for future developments made.

Additionally, as part of the development of the Fabry-Perot version, it was necessary to add an optical reference. This gave, on laboratory sources, an average noise level of ≈ 20 cm s^{-1} and a long term stability of ≈ 4 m s^{-1}.

Acknowledgements

I would like to thank everybody who has helped and advised me with this project. Particular thanks must go to all the members of the old *ISOS* group: Prof. Ring, Ken Reay, Andy Forest, Kris Pietraszewski, Mark Leeper, Robert Renton plus Ian East, Martin Wells and Tom Hicks; to the mechanical workshop: Joe Osborne, Bill Stannard, plus various apprentices; electrical workshop: Mick Bartholomew, Harry Vine, Mark Hooker, and Victor de Menzes; people who have assisted me computerwise, including Steve Hart, Sunil Sidher and Graeme Willoughby; and Dr. Quenby, for allowing me to use the facilities of the Astrophysics Group to complete this project. Others include RGO, for the spectrometer and Bob Airey, for re-coating the mirrors. Finally , I would like to thank my parents for their help and encouragement.

Contents

Preface 13

1 Stellar Oscillations 15

1.1 Asteroseismology 15

1.1.1 Solar Oscillations 15

What are the 5 Minute Oscillations? 17

1.1.2 Rapidly Oscillating Ap Stars 19

Observations of roAp Stars 20

HR 1217 20

γ Equ 20

α Cir 20

1.1.3 Main Sequence Stars 21

The Problem 21

Stellar Parameters from Stellar Oscillations; the Reason Why . . 23

Observations 25

ε Eri 26

α Cen 28

α CMi 29

2 Searching for Stellar Oscillations 31

2.1 Optimal Strategy 31

2.1.1 Length of Observing Time 31

2.1.2 Multi-Site Observations 32

2.1.3 Conclusion 32

A Caveat 32

2.2 Photometry versus Radial Velocity Measurements 33

2.2.1 Photometry 34
Reducing Photometric Noise 35
Telescope Diameter 35
Use of a Reference Star 35
"Clever" Methods 36
2.2.2 Doppler Methods 36
2.2.3 Summary 37
2.3 Methods of Measuring Radial Velocities 38
2.3.1 Grating Methods 38
The Griffin Radial Velocity Spectrometer 38
Improved Reference 39
2.3.2 Resonance Line Methods 41
Resonant Scattering Cells 41
Magneto-Optic Filters—*MOF* 42
2.3.3 Interferometric Methods 44
PEPSIOS 44
The Michelson *ISOS*—Interferometric Oscillation Stellar Spectrometer 45
Fabry-Perot *ISOS* 47

3 Defining the Instrument 49
3.1 The Need for Multi-lining 49
3.2 The Radial Velocity Spectrometer 52
3.2.1 Preamble 52
3.2.2 Some Methods for Multi-lining a Radial Velocity Interferometer . 53
Using Pre-dispersion with a Radial Velocity Interferometer . . . 53
3.3 Design Considerations 54
3.3.1 Maintenance of Phase with Radial Velocity Change 55
Fabry-Perot 55
The Michelson 56
3.3.2 Resolution-Luminosity Product—the Maximum Useable Input Aperture 57
The Fabry-Perot 57
The Michelson 59

3.3.3 Fibre Positioning Accuracy 60
The Fabry-Perot 60
The Michelson 64
3.3.4 Pre-disperser 65
3.4 Detailed Fabry-Perot Design Study 67
3.4.1 Optimum Fabry-Perot Resolution 67
3.4.2 Filter Width 68

4 The Pre-Disperser **71**
4.1 Optical Fibres 71
4.2 Interfacing the Telescope to the Input Optical Fibre 72
4.3 The Echelle 74
Choice of Dispersion 74
4.3.1 Interfacing the Input Optical Fibre to the Echelle 76
Input Optics 76
Correcting for Inherent Stellar Radial Velocity 77
4.3.2 The Output Mask from the Echelle 80
Selecting the Stellar Lines 80

5 The Interferometer **83**
5.1 The Michelson Interferometer 83
5.2 The Fabry-Perot 85
5.2.1 The Ideal Etalon for the Current Pre-Disperser 85
5.2.2 The Available Etalon 86
5.2.3 Building the Interferometer 88
Housing 88
The Collimator and Camera Lenses 89
Stabilization 89
Photon Counting 90
Increased Resolution in the Capacitance Micrometry 90
The Digital Control System 92
5.2.4 Controlling the Instrument 92
Chopping 92
The Reference Signal 93

Minimizing the Error in the ratio $(A-B)/(A+B)$. 96
Isolating the Stellar and Reference Light 97
The Chopping Software 97
Scanning 102
The Scanning Software 102
Finding the Star 104
Improving the Finesse 104

6 Instrumental Tests **107**

6.1 Stability Tests on the Single Line Fabry-Perot 107
6.1.1 Stability of the Cadmium Lamp 108
Problems with the 50 Hz mains frequency 108
6.1.2 Selecting the Optimum Gain and Drift Terms 108
Further Problems 109
A New Method of Handling the Drift, Plus Finding the Optimum Gain 110
6.1.3 Radial Velocity Stability Tests 112
Stability Without the Optical Reference 112
Initial Offset stability Tests 113
6.1.4 Tests with the 'New' Box 114
Stabilty without the Optical Reference, but with the 'New' Box . 114
Offset Stability With the 'New' Box 115
6.1.5 Effect of Temperature on the Offset Electronics 118
6.2 The Echelle Pre-disperser 119
6.2.1 The Filter Profile 119
Transmission Variations Across the Fibres 121
A Caveat 121
6.2.2 Positioning Accuracy of the Optical Fibres in the echelle. 123
6.3 The Multi-Lined Fabry-Perot 127
6.3.1 Selection of the Lines 127
6.3.2 Positioning the fibres in the Fabry-Perot 127
6.3.3 Line Profile Scans 130
Single Lines 130
Sensitivity variations across the photocathode 130

The Multi-Line Line Profile 134
6.3.4 Improvement in Signal-to-Noise. 134
6.3.5 Radial Velocity Measurements on the Sun 138
Detection of the Sun's Rotation 138
The 5-Minute Oscillation from Part of the Sun 139
6.4 Multi-Lining the Michelson 140

7 Conclusions and Future Developments **145**
7.1 The Single-Line Fabry-Perot 145
7.2 The Echelle Pre-Filter 146
7.3 The Multi-Lined Fabry-Perot 147
7.3.1 A Possible Multi-lined Fabry-Perot 147
7.4 The Multi-lined Michelson 148
7.5 Conclusion 149

Appendices

A Field-Widening the Michelson Interferometer **151**

B Discussion on the detection of the 5 minute oscillation 153

List of Figures

2.1 Typical power spectrum for all good photometric sites for 0.5–1 m telescopes. 35

2.2 The Birmingham resonant scattering spectrometer 42

2.3 The magneto-optic filter 43

2.4 The Imperial College Michelson *ISOS* 45

3.1 Triangular absorption line. 50

3.2 Keeping the phase constant for different wavelengths by introducing them at differing angles. 54

3.3 Errors in alignment of the fibres in the Fabry-Perot. 61

3.4 Effect of errors in the phase of the Michelson's $\cos^2$ fringes. 63

3.5 Convolution of input aperture with output aperture for differing size slits. 66

3.6 Sensitivity v. resolution for differing line profiles 67

3.7 Error in radial velocity v. filter drift for a fixed filter profile. 69

3.8 Error in radial velocity v. filter drift for a Gaussian filter profile. 70

4.1 Focal ratio degradation in a 200 μm A.S. fibre. 73

4.2 Interfacing the telescope to the optical fibre. 74

4.3 The Learner echelle in its original condition. 75

4.4 Altering the output focal ratio from the fibre. 76

4.5 Input optics to the echelle spectrometer. 77

4.6 Spring strips design for compensating for changes in radial velocity. . . . 79

4.7 Input fibre angle adjuster. 80

4.8 Output plate holder. 81

4.9 Output fibre mounting technique. 82

5.1 Use of a field lens in the Michelson interferometer to stop vignetting. . . 84

5.2 Positional tolerance for the available Fabry-Perot. 87
5.3 Difference in optical and capacitor gaps. 88
5.4 The Fabry-Perot radial velocity interferometer. 91
5.5 Errors caused by a constant drift. 95
5.6 Flow chart for a 'normal' reference point. 99
5.7 Timing of the interrupts for a 'normal' chop. 100
5.8 Timing of interrupts for the first two chops of each point. 101
5.9 Screen display for scanning routine. 104

6.1 FFT of the signal without the lamp frequency controller. 109
6.2 Finding the optimum gain and drift terms. 111
6.3 Radial velocity stability of the uninsulated etalon. 112
6.4 Offset stability over a 1 order chop for the uninsulated etalon. 113
6.5 Radial velocity stability of the etalon inside the 'new' box. 114
6.6 Radial velocity stability for a one order chop. 115
6.7 Radial velocity spectrum of figure 6.6. 116
6.8 Radial velocity stability for a six order chop. 117
6.9 Radial velocity spectrum of figure 6.8. 117
6.10 The effect of temperature on the offset electronics for a one order chop. 118
6.11 The effect of temperature on the offset electronics for a six order chop. . 119
6.12 The measured filter profile of the echelle for differing slit sizes. 120
6.13 Variations in transmission with input position in optical fibres. 122
6.14 Using a glass plate to correct for misalignment in the fibres. 125
6.15 Other methods of holding the fibres. 126
6.16 Scans of the on and off-axis line profiles, plus the filter profiles, of the lines eventually used. 131
6.17 Sensitivity variations in the E.M.I. side window photocathode 133
6.18 Addition of the lines. 135
6.19 Drifts across the Sun showing the Solar rotation. 138
6.20 Five minute oscillation from a small part of the Sun's surface 139
6.21 Five minute oscillation from a small part of the Sun's surface 140
6.22 Beating of the cadmium blue and green and mercury green lines in the Michelson *ISOS*. 141
6.23 Scans across the Sun using the Michelson + $\cos^2$ fringes. 143

A.1 Condition for field-widening 152

List of Tables

1.1 A selection of oscillating stars 16
1.2 Properties of oscillations of ZAMS models 22
1.3 Properties of oscillations of the models in a $1M_{\odot}$ evolutionary sequence. 22
1.4 Formal errors in inferred age t, mass M, initial hydrogen abundance Y and a mixing-length parameter, α 25
1.5 Transformation of the error matrix of Table 1.4, with g_s replacing Z/X 25

2.1 Comparison of radial velocity and photometric measurements of Solar p-modes 33
2.2 Comparison of Radial Velocity and Luminosity Measurements for Detecting Solar-Type Oscillations. 37

5.1 Specifications of an 'ideal' and the available etalons (at 5000 Å). 86

6.1 Alignment accuracy for the fibres in the echelle. 124
6.2 Calculated positions for the useable lines with the available etalon. . . . 128
6.3 Lines successfully used with the Fabry-Perot. 129
6.4 Radial velocity sensitivity of the Fabry-Perot. 136
6.5 Comparison of the sensitivity of the multi-lined Fabry-Perot. 137
6.6 Lines used with the multi-lined Michelson. 141
6.7 Improvement in sensitivity of the multi-lined Michelson. 142

7.1 Possible interferometer parts of a Fabry-Perot based multi-lined system 148

Preface

The discovery of the Solar '5 minute' oscillations has led to a greater understanding of the interior of the Sun. A logical extension of this work is to try and find the corresponding oscillations in other stars. Unfortunately, so far, the current generation of 'Stellar Seismometers' have failed to give conclusive results.

The Imperial College Astrophysics Group has developed two instrument for measuring stellar oscillations, based on Fabry-Perot and Michelson interferometers. A technique was suggested that could improve the signal to noise ratio by enabling them to use many lines. This could, theoretically, be used with either type of interferometer. It was, therefore, decided to investigate the practicality of using this technique with both interferometers to find out which would be the most suitable for further development.

Dr. K.A.R.B. Pietraszewski concentrated on the Michelson interferometer, whilst I was responsible for the pre-disperser (chapter 4) and the version using the Fabry-Perot. In addition, part of my work involved developing an optical reference for the Fabry-Perot and carrying out a series of test to illustrate the improvements in stability possible. Another colleague, M. Leeper, was responsible for providing the electronics used to provide extra resolution in the gap of the Fabry-Perot. The optical reference was, as well as being necessary for the multi-lined Fabry-Perot, equally applicable to a single line instrument.

Chapter 1

Stellar Oscillations

Many types of stars are known or are suspected to oscillate. Some have been observed indirectly, (for example, the effect on the chromosphere of late-type giants and super giants [1, page 15]), but most have been observed by direct methods, such as line profile variations, (e.g. β Cepheids [2]), photometry and spectroscopic methods.

Measured radial velocities in stars range from a few hundred kilometres per second down to the 15 $\mathrm{cm\,s^{-1}}$ seen in the Sun, with periods of several days to a few minutes. Table 1.1 gives several examples of oscillating stars.

1.1 Asteroseismology

Christensen-Dalsgaard [3] divides stars exhibiting intrinsic periodic photometric and/or radial velocity variations into two types. Those which exhibit only a few modes which he describes as *classical* variable stars and those with many modes the study of which he calls *seismology*. The latter is restricted to main sequence stars, (including the Sun), and rapidly oscillating Ap stars (roAp stars). The author, if only to keep this chapter to a finite length, intends to follow this convention and concentrate on asterioseismology.

1.1.1 Solar Oscillations

Solar oscillations were first discovered in 1960 by Leighton, Noyes and Simon at Caltech [4], whilst studying the surface velocity patterns of the Sun. Expecting incoherent patterns, they were surprised to find that parts of the Sun were seen to oscillate with periods of 5 minutes and velocities of $\approx 400\ \mathrm{m\,s^{-1}}$, lasting for about half an hour. At first, they were thought to be random responses to turbulence at the convective zone,

Table 1.1: A selection of oscillating stars

Type	Period	Velocity	Modes
β Cepheids	0.1–0.3 days	10–50 km s^{-1}	Radial & non-radial ($l \approx 2$), p_0 or p_1 or p_2
δ Scuti	0.02–0.3 days	$\approx$ 1–10 km s^{-1}	Radial & non-radial, p_0–p_4
Cepheids	1–50 days		Radial, possibly p_0 or p_1 or p_2
RR Lyrae stars	0.4–0.8 days	$\approx$ 50 km s^{-1}	Radial, p_0 or p_1, possibly p_2
roAp stars	4–15 min.	10–500 m s^{-1}	
Main sequence (the Sun)	$\approx$ 5 min.	$\leq$ 15 cm s^{-1}	Both high and low order p-modes, plus low order g-modes

but in 1970, Ulrich [5] and, independently, Leibacher and Stein [6], suggested that the Sun was an acoustic cavity and what was being seen were trapped acoustic waves. This was finally confirmed by Deubner [7] in 1975.

Possibly the first observations of 'global' 5 minute oscillations were made by Fossat *et al.* [8]. They were observing the Sun with differing diameter apertures, including one taking in the whole disk. They obtained a velocity of 2.4 ± 0.8 m s^{-1} from whole disk measurements.

Another type of global 'oscillation' was observed in 1976 by Brookes *et al.* [9] using a potassium resonance cell [10], (see section 2.3.2), and independently by Severny *et al.* [11], using a Solar magnetometer. Rather than acoustic waves with periods of 5 minutes, these had periods of 160 minutes. However 160 minutes is exactly $\frac{1}{9}$th of a day, which naturally made people suspicious. This problem seemed to be resolved when the Crimean data was combined with data from Stanford using a superimposed epoch technique and the period was found to be 160.01 minutes [12]. However, van der Raay [13] has presented very convincing arguments that the period *is* 160 minutes, so it is almost certainly terrestial in origin. If they were genuine, the consensus was that

they were gravity waves.

First to resolve the different modes in global 5 minute oscillations were the Birmingham Solar oscillations group using the aforementioned potassium resonance cell [14]. Studying global modes has the advantage that as only the lowest l values, (l = 0–3), can be observed, they are easily interpreted. In particular, the l = 0–2 modes are among the most interesting as they are the only ones to penetrate to the core of the Sun, (see below).

What are the 5 Minute Oscillations?[1]

An oscillating spherical body can be described by the wave numbers n, l, and m: n being the radial order, roughly equivalent to the number of zeros in a radial direction; l being the degree, the number of nodes on the surface and m is the azimuthal order, the number of nodes around the equator, and, consequently must vary between $\pm l$. The degree, l, is related to the horizontal wave number, $k_{\rm h}$, and wavelength, λ, of the mode at radius, r, by

$$k_{\rm h} = \frac{2\pi}{\lambda} = \frac{L}{r}, \tag{1.1}$$

where $L = \sqrt{l(l+1)}$. $l = 0$ corresponds to radial oscillations where the entire body moves in and out in phase.

The '5 minute' oscillations are sound waves trapped in an acoustic cavity. They can be approximated by plane waves with the dispersion relation

$$k^2 = k_{\rm r}^2 + k_{\rm h}^2 = \frac{\omega^2}{c^2}, \tag{1.2}$$

where $k_{\rm r}$ and $k_{\rm h}$ are the radial and horizontal wave numbers. $k_{\rm h}$ is given from equation 1.1. By subtracting equations 1.1 from 1.2

$$k_{\rm r}^2 = \frac{\omega^2}{c^2} - \frac{L^2}{r^2} \tag{1.3}$$

is obtained.

Close to the surface, c is small, hence $k_{\rm r}^2$ is large; so the wave propagates nearly vertically. With increasing depth, (and sound speed), a point is reached where $k_{\rm r} = 0$.

[1]Most of the next three sections have been taken from two review papers by Gough [15] and Christensen-Dalsgaard [16]. Whenever possible the notation of Christensen-Dalsgaard has been used. The most important variation to be careful of is $\Delta\nu$ in Christensen-Dalsgaard work [16], which in Gough [17] is equivalent to $\nu_0 = 2 \times \Delta\nu_{\rm Gough}$. (Though latterly Gough uses $\Delta_{n'}$ for $\Delta\nu$.) In [15] Gough seems to have become confused by this in (my) equation 1.16.

This turning point is the bottom of the acoustic cavity. For Solar type stars it is given by

$$r_t \approx 0.8\frac{(l+\frac{1}{2})R}{(n+\frac{1}{2}l+\alpha)}. \tag{1.4}$$

The top of the acoustic cavity is formed just below the top of the photosphere where the density drops off rapidly.

It can be shown [15] that for low degree modes the frequency is given by

$$\nu \approx (n+\frac{l}{2}+\alpha)\Delta\nu + \varepsilon_{n,l}, \tag{1.5}$$

where [16]

$$\Delta\nu = \left[2\int_0^R \frac{\mathrm{d}r}{c}\right]^{-1} \tag{1.6}$$

and $\varepsilon_{n,l}$ is a small correction term

$$\varepsilon_{n,l} = \mathrm{O}(\Delta\nu\, n^{-1}). \tag{1.7}$$

$1/\Delta\nu$ is the sound travel time across the diameter of the star, and α is a term that depends on conditions near the surface, and hence, as the wave is travelling vertically, is mostly a function of frequency not l. As can be seen, $\Delta\nu$ is the approximately equal interval between modes with the same degree, l, but with radial orders which differ by one. In fact, modes form pairs in which $\nu_{n,l} \approx \nu_{n-1,l+2}$, so giving the typical structure to resolved power spectra.

The separation, $\delta\nu_{n,l} = \nu_{n,l} - \nu_{n-1,l+2} \approx 4l + D_0$ is an important diagnostic tool as D_0 mostly depends on conditions near the turning points, i.e. in the core. As the waves close to the surface are almost vertical, their behaviour is nearly independent of l, and it is only near the turning point that k_h is comparable to k_r. This means that the separation between the pairs of modes is more or less unaffected by most of the Sun except the very bottom of the acoustic cavity, when for low degree modes, the wave is in the core.

The azimuthal mode, m, is only apparent if there is a preferred axis to the star. In the Sun, as probably in a lot of stars, this is provided by rotation. This gives a splitting of the frequencies,

$$\nu_{nlm} = \nu_{nl0} + m\,\Delta\nu_{nlm}, \tag{1.8}$$

where $\Delta\nu_{nlm}$ is a weighted average of the rotation frequency, $\Omega(r,\theta)/2\pi$, of the star.

1.1.2 Rapidly Oscillating Ap Stars[2]

Rapidly oscillating Ap stars (roAp) are cool magnetic Ap stars, with periods of 4–15 minutes and with light variations of $B \lesssim 0.016$ mag. The short periods imply that these are high amplitude p-mode oscillations.

Kurtz showed that the amplitude of some of them is modulated by the rotation period of the star, with the maximum amplitude corresponding to the maximum effective magnetic field. He demonstrated that this can be simply explained by the oscillations being low degree non-radial oscillations with their axis aligned with the magnetic field. This is known as the *Oblique Pulsator Model.* The major problem with this model is that there should be precession of the oscillations with respect to the magnetic axis because of advection. This has not been seen. In fact, HR 1217 had, (by 1985), remained in phase for over three years and HR 3831 for more than four. Dolez and Gough suggested that the growth time for the oscillations is short compared with the precession time. Also, only oscillations aligned with the magnetic axis are excited to an observable amplitude. Dziembowski and Goode, however, suggested that the oscillations are dominated by the magnetic field rather than by rotation and so will not drift with respect to the magnetic field.

As an alternative, Mathys has suggested the *Spotted Pulsator Model*, in which the oscillations are caused by surface inhomogeneities and "a variable ratio of surface flux to radius variation with cylindrical symmetry about the magnetic axis of the star". This avoids most of the above problems. It has, however, several "unknown and currently unmeasurable" free parameters, and hence, it is "neither applicable or testable" (Kurz).

One of the suggestions for the excitation mechanism for roAp stars is overstable magnetic convection. where the field lines are 'glued' to the plasma and supply a restoring tension against convective motion. This is most effective at the magnetic poles, hence, the oscillations are aligned with the magnetic field. In roAp stars, the time scale for magnetic instability is approximately ten minutes, so the observed periods are simply the modes closest to this. All roAp stars, however, lie within the δ Scuti instability strip, which has led to the suggestion that the κ-mechanism, (plus the magnetic field enhancing the instability of non-radial modes), is the method of excitation.

[2]Most of the following is taken from a review paper by Kurtz [18]

Observations of roAp Stars

There are about a dozen roAp stars known. Most of them have only been observed photometrically. Radial velocity measurements have been made on a few of these. As this thesis describes a radial velocity interferometer, only those for which (successful) radial velocity measurements have been made will be discussed.

HR 1217 This has been observed by at least two groups. Matthews *et al.* [19] used a coudé with a Reticon array stabilized using the mercury 4358 Å line on the 3.6 m CFHT, whilst simultaneously observing the light curve on another telescope. They observed HR 1217 for two consecutive nights, the second of which was at its maximum photometric amplitude. They treated the data by 'binning' each (previously known) cycle into ten separate bins. The first night they could only put an upper limit on the oscillations of $\approx 130\ \mathrm{m\,s^{-1}}$, whereas the second night gave a peak-to-peak amplitude of $\approx 400 \pm 50\ \mathrm{m\,s^{-1}}$.

Leeper *et al.* [20,21] used the Fabry-Perot part of the instrument, (as described in chapter 5), with a single line [22] to observe HR 1217 on the 60″ IRFC telescope. An amplitude of $258 \pm 58\ \mathrm{m\,s^{-1}}$ at a frequency of $2731.7 \pm 2\ \mu$Hz for the best four nights of data was measured.

γ Equ Libbrecht [23] observed γ Equulei using the coudé spectrograph of the 200″ Hale telescope with an iodine absorption cell to provide a stable reference spectra, (see section 2.3.1.) The resulting spectrum was recorded using a charge couple device (CCD) read out continuously. Four nights of observations led to the discovery of three oscillation modes at 1366, 1369.2 and 1427 μHz with a peak-to-peak amplitude of $42\ \mathrm{m\,s^{-1}}$ for the integration of the power from 1300–1450 μHz. He claimed a signal-to-noise ratio much higher than obtained previously (by Matthews *et al.* on HR 1217). He did not observe the previously measured photometric period of 1339 μHz [18].

α Cir Pietraszewski had obtained data on α Circini on the 1.9 m at the South African Astronomical Observatory (SAAO) using a Queensgate Instruments Fabry-Perot, (see section 2.3.3.). This was re-examined by Leeper [20], using iterative sine wave fitting, (ISWF), who confirmed a period of 2.5 ± 0.1 mHz and found an amplitude of $1015 \pm 160\ \mathrm{m\,s^{-1}}$, with a confidence level, (as from Scargle [24]), of 99%.

1.1.3 Main Sequence Stars

The search for oscillations in Solar type stars is proving to be one of the most challenging observational problems currently facing astronomers. Though a few astronomers have claimed to have detected them [25,26,27,28], after a lot of theoretical speculation [29,30,31,32], the validity, (caused by high noise levels and lack of repeatability), of their observations is questioned [33,34].

The Problem

The Sun oscillates with a velocity of 15 cm s^{-1} and a period of 5 minutes. Christensen-Dalsgaard and Frandsen [35] have modelled the oscillatory behaviour of main sequence stars with differing masses to the Sun. Their calculations were based on energy equipartition between the oscillations and convection, as this appeared to dominate the linear damping and excitation of the oscillations. Also, as the properties of the modes have very little dependence in l, the calculations were made for radial oscillations, ($l = 0$).

At the edges of the convection zone, the convective kinetic energy, E_c, is at a minimum, whilst the mean lifetime of a convective eddy, τ_c, tends to infinity. At approximately where the superadiabatic gradient is a maximum, τ_c tends towards its minimum value, $\tau_{c,min}$. Any modes with periods, Π, shorter than $\tau_{c,min}$ have at least two points, at $r = r_i$ say, where $\tau_c = \Pi$. So

$$E_{osc} = \sum_i E_c(r_i)\,. \tag{1.9}$$

This relies on the simplification that modes shorter than $\tau_{c,min}$ would not be excited.

The oscillation energy is related to the radial surface velocity, v_s, by

$$E_{osc} = \frac{1}{2} M v_s^2 \mathcal{E}_{osc}\,, \tag{1.10}$$

where

$$\mathcal{E}_{osc} = \int_V \rho |\xi|^2 dV \xi_r(r_s)^2, \tag{1.11}$$

ξ is the eigenfunction of linear oscillation, ξ_r its radial component and r_s the surface radius of the star. Hence the surface velocity is given by

$$v_s = \left[\frac{2\sum_i E_c(r_i)}{M\mathcal{E}_{osc}}\right]^{1/2}. \tag{1.12}$$

The results of the calculations are shown for zero age stars in table 1.2. As can be seen, both the velocity amplitude and period tend to a maximum for a star with about

Table 1.2: Properties of oscillations of ZAMS models: M, $T_{\rm eff}$ and L are the mass, effective temperature and luminosity respectively, of the model; $M_\odot$ and $L_\odot$ the Solar values; $v_{\rm s,max}$ and $(\delta L_{\rm s}/L_{\rm s})_{\rm max}$ are the maximum values of the surface velocity and relative luminosity perturbation; with $\Pi_{\rm max}$ being the period corresponding to, and $\Delta\nu$ the frequency difference of two adjacent modes at the maximum velocity, (from [35]).

$M/M_\odot$	$T_{\rm eff}$	$L/L_\odot$	$v_{\rm s,max}$ (cm s^{-1})	$(\delta L_{\rm s}/L_{\rm s})_{\rm max}$	$\Pi_{\rm max}$ (min)	$\Delta\nu$ (μHz)
0.8	4880	0.25	3	6.0×10^{-5}	4	204
0.9	5285	0.44	6	1.5×10^{-6}	4	184
1.0	5646	0.71	10	2.5×10^{-6}	4	165
1.1	5916	1.13	15	3.4×10^{-6}	5	142
1.2	6178	1.70	20	4.2×10^{-6}	5	124
1.3	6457	2.49	25	5.1×10^{-6}	5	110
1.4	6778	3.49	37	6.2×10^{-6}	10	96
1.5	7184	4.74	144	1.3×10^{-5}	18	89
1.6	7640	6.26	72	1.0×10^{-5}	9	94
1.7	8072	8.06	71	2.7×10^{-6}	10	93
1.8	8475	10.2	72	2.7×10^{-5}	7	90

$1.5M_\odot$ and a temperature of 7184 K. This, according to Lang [36], is equivalent to a F0 star.

Table 1.3 shows the evolutionary sequence of oscillations for a $1M_\odot$ star. With increasing age both the period and amplitude increase, whilst the spacing between adjacent modes decreases.

To understand what is happening the following equations are needed (again from

Table 1.3: Properties of oscillations of the models in a $1M_\odot$ evolutionary sequence, (again from [35]).

Age (10^9 yr)	$L/L_\odot$	$T_{\rm eff}$	$v_{\rm s,max}$ (cm s^{-1})	$(\delta L_{\rm s}/L_{\rm s})_{\rm max}$	$\Pi_{\rm max}$ (min)	$\Delta\nu$ (μHz)
0	0.71	5646	10	2.5×10^{-6}	4	165
2.65	0.85	5713	13	3.0×10^{-6}	5	150
4.75	1.00	5770	15	3.5×10^{-6}	5	137
9.68	1.68	5784	26	6.2×10^{-6}	8	96
11.71	2.35	5359	34	9.3×10^{-6}	15	59

Christensen-Dalsgaard and Frandsen [35]):

$$\mathcal{E}_{\rm osc} \approx \frac{3}{4\pi^2}\frac{\rho_{\rm s}}{\overline{\rho}}\frac{c_{\rm s}}{r_{\rm s}}\mathcal{F}(\nu/\nu_{\rm c})\int_0^{r_{\rm s}}\frac{{\rm d}r}{c}, \tag{1.13}$$

and

$$E_{\rm c} \approx \rho^{1/3}F_{\rm c}^{2/3}(T/g_{\rm s})^3, \tag{1.14}$$

where $\rho_{\rm s}$ is the photospheric, and $\overline{\rho}$ is the mean density of the model, $c_{\rm s}$ is the velocity of sound in the atmosphere, $\mathcal{F}(\nu/\nu_{\rm c})$ is the dependence of $\mathcal{E}_{\rm osc}$ on ν, where $\nu_{\rm c}$ is the Lamb cutoff frequency. In equation 1.14, $F_{\rm c}$ is the convective flux, T the temperature and $g_{\rm s}$ the surface gravity. In the zero age main sequence (ZAMS) model, with increasing mass, $T_{\rm eff}$ increases. As $\rho_{\rm s}$ is inversely proportional to temperature [35], it therefore decreases. This is the major cause of the decrease in $\mathcal{E}_{\rm osc}$, and, referring to equation 1.12, leads to an increase in $v_{\rm s}$. Also $g_{\rm s}$ decreases for increasing mass, (for $M \lesssim M_\odot$), and is roughly constant for higher masses. Along with the increase in T, this causes an increase in $E_{\rm c}$, hence, again an increase in $v_{\rm s}$. The fall in $v_{\rm s}$ for the higher mass models is due to a decrease in the efficiency of convection, which by the $1.8M_\odot$ is down to carrying 40% of the flux [35].

From equation 1.6 the decrease in mean frequency interval, $\Delta\nu$, is mainly due to the increasing radius with increasing mass. c, the sound speed in the star, is largely unaffected by the change in mass.

The change in surface velocity, $v_{\rm s}$, is largely caused by the decrease in surface gravity, $g_{\rm s}$, due to an increase in radius. Again, increasing radius is the main reason for the decrease in $\Delta\nu$.

Tables 1.2 and 1.3 demonstrate that whilst the highest velocities found on the Sun are about 15 cm s^{-1}, it is possible that other stars of higher masses or greater age can have much larger oscillations. Unfortunately, this is coupled with a small decrease in the modal spacing. This means that for the spacing to be resolved, slightly longer observing runs are necessary.

Stellar Parameters from Stellar Oscillations; the Reason Why

Even though the discovery of stellar oscillations in main sequence stars is proving to be very difficult, *when* they are found, the frequencies involved will be some of the most accurately known parameters of the star(s). The intention of the following is to show how, if the frequency interval, $\Delta\nu$, and possibly even more importantly, the separation

of the pairs of frequencies, $\delta\nu$, could be measured, this could lead to a much more accurate determination of some of the most basic stellar parameters. N.B. however, there has been no unequivocal discovery of an oscillating, 'normal', main sequence star.

From equation 1.4 for $n \gg l$, (as could be observed in stars), $r_t \ll R$; i.e. almost the entire radius of the star forms the acoustic cavity; therefore the frequency interval $\Delta\nu$, depends only weakly on r_t. The separation of pairs of modes, $\delta\nu$, is the difference, for two similar modes, of c, the velocity of sound, which is dominated by the conditions in between the two values of r_t. So, the value of $\delta\nu$ depends very strongly on conditions in the core.

The structure of a star depends on its chemical constituents, its age and its mass. Zero age main sequence stars, as a first approximation, can be considered to have $M \propto R^{3/4}$ [15]. The frequency interval between adjacent modes of equal l is (from [15]),

$$\Delta\nu \propto \left(\frac{g_s}{R}\right)^{1/2} = \left(\frac{GM}{R^3}\right)^{1/2} \tag{1.15}$$

As the star evolves and the radius increases, the above homologous series is maintained. As the frequency interval, $\Delta\nu_\odot$, is $\approx 135\ \mu$Hz; therefore,

$$\Delta\nu_* \approx 135 \left(\frac{M}{M_\odot}\right)^{1/2} \left(\frac{R}{R_\odot}\right); \tag{1.16}$$

i.e. it depends on both radius, hence age, and mass. As g_s can be estimated spectroscopically, by using $\Delta\nu$, both M and R can be determined separately.

As well as expanding, in the core, as the star evolves, hydrogen is converted to helium. This causes a rise in the mean molecular weight of the star, which causes the acoustic frequencies to be reduced [15]. As the modes which penetrate deepest into the stars are the most affected, $\delta\nu$ is reduced. So $\delta\nu$ is measuring the nonhomologous changes in the core and determines the evolutionary age $\tau = t/t_{\rm ms}$, where $t_{\rm ms}$ is twice the time necessary for the star to use up half the hydrogen in its core [15]. $t_{\rm ms} \propto M^{-4}$ [15] for Solar type stars; therefore by knowing $\delta\nu$ and $\Delta\nu$, (along with g_s to give the mass), it is possible to calculate the age of the star.

Theoretical stellar models depend on M; t; the mixing parameter, α; and the chemical composition, X, Y, and Z—the initial relative abundances by mass of, respectively hydrogen, helium and the rest, (i.e. $X + Y + Z = 1$). For a given X, Z and α, stellar evolution theory relates luminosity, L, and $T_{\rm eff}$ to M and t. Hence if L, $T_{\rm eff}$ and, say, Z/X are known, using $\Delta\nu$ and $\delta\nu$, it is possible to determine M, t, Y, and α.

Table 1.4: Formal errors in inferred age t, mass M, initial hydrogen abundance Y and a mixing-length parameter, α

	$\delta t/t_{\rm ms}$	$\delta M/M$	$\delta Y/Y$	$\delta\alpha/\alpha$
$T_{\rm eff}$ (2%)	-0.06	0.04	-0.09	0.16
L (10%)	0.03	0.05	-0.02	-0.11
Z/X (50%)	1.1	-1.9	5.6	-2.6
$\Delta\nu$ (1 μHz)	0.01	0.01	-0.02	-0.003
$\delta\nu_{l=0}$ (1 μHz)	-0.13	-0.02	0.10	-0.03

Table 1.5: Transformation of the error matrix of Table 1.4, with $g_{\rm s}$ replacing Z/X

	$\delta t/t_{\rm ms}$	$\delta Z/Z$	$\delta Y/Y$	$\delta\alpha/\alpha$
$T_{\rm eff}$ (2%)	0.04	0.07	0.12	-0.005
L (10%)	-0.03	-0.02	-0.24	-0.008
$g_{\rm s}$ (20%)	-0.17	-0.07	-0.57	0.28
$\Delta\nu$ (1 μHz)	0.01	0.01	-0.002	-0.013
$\delta\nu_{l=0}$ (1 μHz)	-1.14	-0.04	0.05	-0.003

From Gough [15], table 1.4 lists the partial derivatives of $t/t_{\rm ms}$, $\ln M$, $\ln Y$, and $\ln\alpha$ with respect to the parameters in the first column. The precision of measurement, according to Gough, is probably optimistic. The limiting factor is the model's extreme sensitivity to the precision in Z/X. However, he showed that by knowing the mass, either from a binary system or from the surface gravity, the situation is much improved. Table 1.5, again from Gough [15], shows the results. As can be seen, for example, the age of the star can be found to within 20%. Unfortunately the helium abundance is very poorly determined.

Observations

The standard method of presenting frequency spectra of solar oscillation data is as power spectra, i.e. either the velocity or intensity squared. The advantage of this method of presentation is that it enhances the results by emphasizing the peaks from the signal by effectively multiplying them by the signal-to-noise ratio with respect to the noise level.

In stellar data, (at least on main sequence stars), the signal-to-noise ratio, (due to lack of photons), is much smaller, a more complicated 'enhancement' process is necessary. Firstly, in detecting p-modes, apriori knowledge has to be used. From equa-

tion 1.5, the characteristic signature of a p-mode spectrum is a series of equi-spaced (in frequency) peaks. Consequently, either by using auto-correlation or Fourier transforms of the frequency spectrum, the frequency interval ($\Delta\nu$ and its harmonics) appears in the frequency spectrum of the frequency spectrum. Whilst the above process appears to be a legitimate method of combining the signal from maybe twenty to thirty modes, which individually have an amplitude comparable to the noise, the data is inevitably presented as the power spectrum of the power spectrum or, effectively, the signal to the fourth power! i.e. if a signal in amplitude, (as this is what is being measured), is combined to be twice the noise, the perceived 'signal', (to the fourth power), is *sixteen* times the 'noise' level. Random noise spikes, of course, are emphasized similarly.[3]

ϵ Eri As well as in sodium and potassium, in the Sun the oscillations are visible in other lines, including the calcium H and K. In chromospherically active stars the calcium H and K lines are much enhanced. Noyes suggests [26] that the chromospheric response to p-mode oscillations might be enhanced as well. Because of previously measured indications of chromospheric activity [37], the K2 dwarf ϵ Eridani was observed.

The observations were made using a H-K photometer on the 60″ telescope at Mount Wilson on four different nights. On the first and third nights there were three and six, respectively, "prominent" peaks in the power spectrum at around about ten minutes. The three peaks from the first night's data agreed with three of the six in the third night's data to within the resolution, (≈ 50 μHz). To test whether there was an equally spaced p-mode type spectrum, the auto-correlation of the individual nights power spectra was found. This gave peaks which could be identified with $\Delta\nu/2$ and $\Delta\nu$, giving $\Delta\nu \approx 170$ μHz. By doing a cross-correlation between the two power spectra, which gave a modulation of about 86 μHz, it was found that $\Delta\nu = 172$ μHz. Though the individual peaks were not statistically significant—in the third night's data the highest peak was 4.28σ, which has an 87% chance of appearing somewhere in the spectrum—with the coincidence over two nights of data, the possibility of a fluke was reduced—to less than 0.2% in the above case. To further assure themselves of the statistical validity of their technique, they scrambled the data and repeated the process. At no time did they manage to reproduce similar results.

[3]The corollary of this, is of course, that if you are doing instrumental stability tests, the most effective method of demonstrating how stable your instrument is, is to present the data as an *amplitude* spectrum. The author intends to follow the latter convention.

On the second night no oscillations were found. The chromospheric activity was exceptionally high, however, which might have decreased the amplitude in H and K or increased the background noise. Again on the fourth night they failed to find oscillations, even though chromospheric activity was down to normal levels.

According to Noyes, the radius of ϵ Eridani has been found to be $R/R_{\odot} = 0.81$ to within 10%, and, because of its Ca II emission and rotation rate, (which mean it is younger than the Sun), a value of 169 μHz $< \Delta\nu <$ 179 μHz is to be expected. This, of course, is compatible with his results. The peak power, however, is at ten minutes, which is greater than the expected value of around about four minutes. He suggests that this could be because of different excitation mechanisms being dominant in ϵ Eridani. The amplitude of the oscillation is about two orders of magnitude greater than that found in the Sun. This could be due to the velocity of the oscillations being extremely high or the response of the chromospheric emission to the oscillations being higher than in the Sun.

The above seems to be the only attempt, (in print), of measuring the p-mode spectra of ϵ Eridani. Baliunas *et al.* [37], however, had previously found "A strong, broad peak at periods of 6–8 minutes" in the Ca II H and K emission using the same instrument as Noyes.

Guenther and Demarque [29] pointed out that while the chromospheric and rotation rates were consistent with ϵ Eridani being a young star, it also had a low metallicity, which is a sign of an old star. Using the observed $M_{\rm bol}$, $T_{\rm eff}$ plus the Solar helium abundance and mixing length, α, by varying the mass and metal abundance, Z, they were able to construct a model of the star. Unfortunately, with either the observed ($Z = 0.01$), or Solar, ($Z = 0.02$), values for the metal abundance, they had to make the star ridiculously old, (> 20 Gyrs), to get the measured frequency spacing. They managed to resolve this, however, by using a mixing length of one (cf. $\alpha_{\odot} = 1.37$). A star of age 11.48 Gyrs was found to reproduce approximately the same frequency spacing, $\Delta\nu$, as measured, and led to an identification of the modes detected.

Guenther [30,31] obviously then had second thoughts about the age of the star and suggested two possible solutions to the dilemma. The first was that ϵ Eridani was a binary. This would enable the required brightness of ϵ Eridani 'A' to be lower, so bringing the position of the star in the Hertzsprung-Russell diagram nearer to that predicted by the ZAMS model. Unfortunately, ϵ Eridani has been 'speckled' and has

had its radial velocity measured. Neither of these are consistent with it being a binary. Consequently, Guenther concludes that it could be a nearly face on binary with a small separation.

Another possibility, he suggests, is that it has a much higher metal abundance, ($Z \approx 0.03$), which would put it on the required ZAMS track. Guenther says that very active stars like ε Eridani are possibly covered in bright plage regions, which would raise the flux in both the absorption lines and continuum, so leading to a reduction in the lines equivalent widths, and hence, giving an underestimation of the metallicity.

Soderblom and Däppen [32] were also very doubtful of the age attributed to ε Eridani by Guenther and Demarque. By using the observed values of $M_{\rm bol}$, $T_{\rm eff}$ and radius, (from parallax), the Solar helium abundance and fixing the age to less than 1 Gyr, (because, according to them, the chromospheric activity is proportional to t^{-2}), produced a model with the mixing length, $\alpha = 0.5$. This gave even better reproduction of the measured frequency of ε Eridani.

Däppen and Soderblom [33,34] finally arrived at what is probably the correct conclusion. Because of the "unsatisfactory theoretical explanations" and, also, the non-confirmation of the results, ε Eridani *doesn't* oscillate with a frequency separation of 172 μHz. They recalculated the model for non-controversial input parameters and came up with a frequency separation of anything between 198–244 μHz.

α Cen Grec *et al.* [28,27] have observed α Centauri with the 3.6 m ESO telescope, La Silla, Chile on two occasions: for three consecutive nights in 1983 and for one night in 1984. They used a magneto-optic filter [38] with a 0.08 Å bandwidth on the red wings of the two Na D lines, and as a reference signal, 20 Å bandwidth of the continuum centred over the same lines, (see section 2.3.2). Following the above methods of data reduction, they obtained, on the first run, oscillations with amplitudes of 1–2 $\mathrm{m\,s^{-1}}$ with periods of 3.5–8.5 minutes and a frequency interval of $\Delta\nu \approx 165.5$ μHz.

(The following is based on arguments presented by Innis and Isaak [39] for Procyon.) It is very difficult to follow how Grec *et al.* arrive at their conclusions. In most of their figures, the y axis is $\Delta I/I$ to what ever power is relevant. The first graph containing $\mathrm{m\,s^{-1}}$, (their figure 11), has a y axis of $\mathrm{m^2\,s^{-2}\,mHz^{-1}}$ smoothed to a resolution of 0.04 mHz, with a peak value of $\approx 40\ \mathrm{m^2\,s^{-2}\,mHz^{-1}}$. (It is the inverse transform of the frequencies selected from the power transform of the power transform.) This gives a power of $\approx 1.6\ \mathrm{m^2\,s^{-2}}$ *averaged* over $\Delta\nu/2 \approx 0.08$ mHz. As all the power is concentrated

in a single, narrow mode, the *peak* power is much greater. If α Centauri has modes with the same width as the Sun, i.e. 1 μHz, and all the power in the 0.04 mHz is from one mode, then they will have a power of $\approx 64\ \mathrm{m^2 s^{-2}}$. This is equivalent to a velocity of about $8\ \mathrm{m s^{-1}}$. (This is possibly an underestimate; as, even though $\Delta\nu \approx 80$ mHz, and, therefore, there is one mode per 40 mHz, the higher l modes have much smaller amplitudes than the lower l modes.)

Unfortunately, owing to bad weather, they were only able to observe for one night in 1984. Whilst there was a peak at 82.7 μHz in the power spectrum of the power spectrum, it was not the highest.

In the discussion they say that the signal-to-noise ratio of the individual modes is less than 1, (nearer 0.5). Assuming 20–25 equispaced peaks, this improves the statistics by a factor of 4 to 5. This means that they were 80% confident of the value of the frequency range, $\Delta\nu$, curvature, (in the echelle diagram), and global power.

Grec *et al.* go on to say: from measurements of temperature and distance, α Centauri has an estimated radius of $1.23 \pm 0.04 R_\odot$. As it is part of a binary, α Centauri has a very well determined mass of $1.09 M_\odot$. This gives, for a ZAMS star, $\Delta\nu \approx 142$ μHz and a radius of $1.03 R_\odot$. Homologous scaling, ($R^{3/2}\Delta\nu \approx$ const), with $\Delta\nu = 165.5$ μHz predicts $R = 0.93 R_\odot$! As stars are normally expected to expand with age it is a surprising result. Even if α Centauri is believed to be on the ZAMS, it would have to have a mass of only 1 $M_\odot$ to have the measured frequency separation. The measured frequency range is as would be expected for α Centauri. The amplitude,[4] however, is 5–10 times too great. Even though the radial velocities are calculated by simply multiplying the photometric signal by a factor, ignoring any changes in the line profile etc., a factor of 5–10 is difficult to explain.

Demarque *et al.* [40] calculated models of α Centauri for a range of input parameters, where possible, constrained by errors in the observed values. They were unable to reproduce the frequency spacing, as measured by Grec *et al.* All their (quoted) results were in the range $\Delta\nu \approx 100$–120 μHz. They concluded that Grec *et al.*'s observations are "inconsistent with p-mode spectra constructed from standard models".

α CMi Grec *et al.* have also observed Procyon and claim to have detected p-modes. They had 4 nights on the 3.6 m CFHT, and obtained 27 hours of data in total. This gave a resolution of 3.57 μHz. They claim to have found p-modes with an amplitude of about

[4]For some reason they are not quoting power.

70 $\mathrm{cm\,s^{-1}}$ and with a frequency interval, $\Delta\nu$, of 79.4 μHz, with a similar confidence level to their results on α Centauri. This result is generally accepted as being a reasonable result for Procyon. Demarque and Guenther [41], however, did a series of calculations based on several different models of Procyon, and came to the conclusion that $\Delta\nu$ should lie between 50–60 μHz.

Innis and Isaak [39] showed that taking Grec *et al.*'s figure 6, and using a mean power of 10 $\mathrm{m^2\,s^{-2}}$ with the bin size of 80 μHz, gave the power for the signal of 0.8 $\mathrm{m^2\,s^{-2}}$. If this was from a single 1 μHz width mode, it would have a power of 60 $\mathrm{m^2 s^{-2}}$, (or nearly 8 $\mathrm{m\,s^{-1}}$).

Innis and Isaak [39] also observed Procyon, for 11 nights on the 1.9 m at the SAAO, obtaining a noise level of 12 $\mathrm{m^2\,s^{-2}}$ per 0.95 μHz frequency bin. They concluded that there was "little obvious agreement" between their results and Grec *et al.*'s, even though the noise levels, (using the above arguments), were "comparable".

Libbrecht [42] also observed Procyon, using the same instrument as he was to use for γ Equulei [23]. (See also sections 1.1.2 and 2.3.1.) Although he failed to find any significant peaks, after two nights of bad seeing ($\approx$ 3 arcsecond), he obtained a photon shot noise limited velocity of $\approx$ 1 $\mathrm{m\,s^{-1}}$. This is obviously not inconsistent with Fossat's claimed results.

Chapter 2

Searching for Stellar Oscillations

2.1 Optimal Strategy

2.1.1 Length of Observing Time

To detect very small oscillations large numbers of photons have to be counted. What is the best way to do this? Either by a few *nights* on a large telescope or a few *weeks* on a small telescope.

The first thing to discuss is what is being measured. More than just proving the existence of oscillations, before any real use can be made of the data, values such as the frequency interval, $\Delta\nu$, the frequency separation, $\delta\nu$, and the width, hence lifetime, of the modes are needed. This means that the data has to be long enough to resolve these in the Fourier transform.

$\Delta\nu$ is 'fairly easy' to find. In the Sun, $\Delta\nu/2$ has a value of 68 μHz. From tables 1.2 and 1.3, in other stars we could expect a value for $\Delta\nu/2$ of down to, say, possibly 15 μHz. For this resolution, using Loumos and Deeming's criteria, $\Delta\nu/2 > 1.5/T$, for measuring the true separation of two frequencies [43], observations spread over about 28 hours, or two nights would be necessary.

In the Sun, $\delta\nu$ has a value of 9.2 μHz. To find this would require observations spread over $\approx$ 45 hours, or three nights. Of course it is probable that in other stars $\delta\nu$ could be smaller than this; but it seems reasonable to expect that the value of $\delta\nu$ can be found in the sort of allocations of time *sometimes* given on large telescopes.

The modes themselves have, in the Sun, a width of 1 μHz, i.e. they require observations stretching over 12 nights to be resolved, (or 23 nights for there to be two resolution elements over the peak).

2.1.2 Multi-Site Observations

One of the biggest problems in interpreting the data is provided by gaps caused by the alternating day-night cycle, (plus instrumental failure and, of course, bad weather). This produces spurious peaks in the data. Grec *et al.* [44] have used a sodium cell from the South Pole in the southern summer to overcome this. However, because of the short periods for which conditions at the South Pole are suitable, probably the best method for ground based observations of the Sun or stars is a global network.

By observing from more than one site around the world, so that the Sun is being observed continually, ideally, from more than one site at a time, (to reduce the effects of bad weather and instrument problems), the effects of this window function can be removed or at least reduced. The Birmingham group has had a two site network on Hawaii and Tenerife which have produced some of the best Solar oscillations spectra available [45]. They have recently expanded this with a third site at Carnarvon in Australia [46] with plans to expand it further [47]. The Nice group are also planning a *global* global oscillations network [48], whilst the Global Oscillation Network Group *GONG* is concentrating on spatially resolved measurements of the Sun [49,50,51].

2.1.3 Conclusion

With infinite resources, the largest possible telescopes, in a global network, would be used continuously for several weeks to observe the same star in the hope of detecting Solar-type oscillations. Unfortunately, obtaining more than a week on a large telescope is rare. Consequently, to obtain all the potential information available from '5-minute' oscillations, observations are most likely to be on small telescopes. This will be even more true for global networks, (although probably the first multi-site stellar seismology observations were made by Fossat on Procyon using the Russian 6 m telescope and a ≈ 4 m telescope on Hawaii[1]).

A Caveat In some of the earliest data on the Solar 5 minute oscillations [8,14,44], much higher amplitudes were being found than the 15 $\mathrm{cm\,s^{-1}}$ velocity obtained with many months of data. This is because the 15 $\mathrm{cm\,s^{-1}}$ velocity is an *average* velocity, and according to Christensen-Dalsgaard and Gough [52], there is interference between modes with similar frequencies. Claverie *et al.* [14], using 8 hours of data, with a resolution

[1] As reported to ESA–286, Seismology of the Sun and Sun-like stars, Puerto de la Cruz, Tenerife

Table 2.1: Comparison of radial velocity and photometric measurements of Solar p-modes (mostly from [53]).

	Doppler	Intensity
Degree observable	0–3	0–2
Peak signal amplitude	15 $\mathrm{cm\,s^{-1}}$	$1.5 \times 10^{-6}\ \delta I/I$
Background noise (disc centre)	$\approx 330\ \mathrm{m\,s^{-1}}$	$\approx 0.14\ \delta I/I$
Signal-to-noise	4.5×10^{-4}	1.1×10^{-5}
$(\mathrm{S/N})_\mathrm{D} \div (\mathrm{S/N})_\mathrm{I}$	≈ 40	

of 34.7 μHz, obtained a power of 1.2 $\mathrm{m^2\,s^{-2}\,mHz^{-1}}$, leading to power per resolution element, (and hence per mode), of 0.042 $\mathrm{m^2\,s^{-2}}$. This is equivalent to an amplitude of 1.2 $\mathrm{m\,s^{-1}}$ for a 1 μHz mode. Grec *et al.* [44] for 141 hrs of data from the South Pole, with a resolution of 1.97 μHz, found a power of 15 $\mathrm{m^2\,s^{-2}\,mHz^{-1}}$, equivalent to 0.03 $\mathrm{m^2\,s^{-2}}$ per mode, or a maximum amplitude of 24 $\mathrm{cm\,s^{-1}}$. Christensen-Dalsgaard and Gough, (their figure 3), in simulating a single days observations, chose their velocities randomly, using the distribution

$$p(V) = \frac{2V}{\mathcal{V}^2} \exp\left(-\frac{V^2}{\mathcal{V}^2}\right), \tag{2.1}$$

but with no frequency dependence and took $\mathcal{V} = 15\ \mathrm{cm\,s^{-1}}$. They obtained maximum power densities of $\approx 2\ \mathrm{m^2\,s^{-2}\,mHz^{-1}}$, ($\simeq 1.5\ \mathrm{m\,s^{-1}}$ for a mode of 1 μHz width), and found that

"In each case about two-thirds of the peaks dominate the spectrum."

This implies that it might be possible to search for suitable candidate stars for a more detailed study, by observing for only a short time and finding modes oscillating at near their maximum amplitudes.

2.2 Photometry versus Radial Velocity Measurements

There are two main methods of detecting, (and measuring), stellar oscillations: measurement of brightness changes and measurement of radial velocity changes in the star. Both of these have advantages and disadvantages.

2.2.1 Photometry

The Active Cavity Radiometer Irradiance Monitor (*ACRIM*) experiment on the Solar Maximum Mission spacecraft (*SMM*) produced 10 months of useable data before the fine pointing failed. Woodward and Hudson [54] used this to find the low degree p-modes on the Sun. The amplitude of the modes agreed with that predicted from radial velocity measurements. However, even though the data had been taken above the atmosphere, the signal-to-noise ratio was about *40* times worse than that seen in the results from radial velocity measurements (see table 2.1.)

Unfortunately, with an atmosphere in the way, things look even bleaker for photometric measurements. Stars twinkle [55]. More importantly, for the non-naked eye observer,[2] they are also subject to scintillation and transparency variations.

Scintillation is caused by temperature fluctuations at a height of $\approx$ 10 km which can be as small as 0.01 K. Millisecond exposure photographs, by freezing the illumination of a telescope mirror, show that the dominant path size is around $\approx$ 10 cm [56, page 4]. So long as $D_{\text{telescope}} \gg 10$ cm, the effects of these are averaged out, leaving just the contribution from the intensity fluctuations $\gtrsim D$. This leads to a cut-off frequency,

$$\nu_0 = \frac{v_{\text{w}}}{D_{\text{telescope}}} \text{ [56, page 5]}, \tag{2.2}$$

where v_{w} is the wind velocity, (usually $\approx 100\ \text{km}\,\text{h}^{-1}$ at a height of 10 km) [56, page 4].

Below ν_0 the power spectrum of the scintillation is almost constant and is proportional to $D^{-4/3}$. Unfortunately the frequencies we are interested in lie well below the cut-off frequency, ν_0.

Fossat [57,58] has compared low frequency scintillation in Mauna Kea, la Silla, the Canaries, Sutherland and Granada and found the results to be very similar for nights of good seeing at all sites.

Scintillation dominate for periods of less than a few minutes. Above this period, there are low amplitude variations in atmospheric transparency. These are caused by variations in pressure, humidity and aerosol content of the atmosphere. Their power spectrum has a ν^{-2} dependence. Again, Fossat investigated transparency variations and obtained very similar results for all sites. Figure 2.1 illustrates his findings [58].

In the Sun the maximum amplitude of the signal is about 1.5×10^{-6} mag for an approximately 1 μHz wide mode [53]. From figure 2.1 the noise for a 1 μHz bandwidth

[2]Twinkling is dominated by small turbulent elements in near-surface turbulent winds which are averaged out by the much larger telescope aperture [56, page 9].

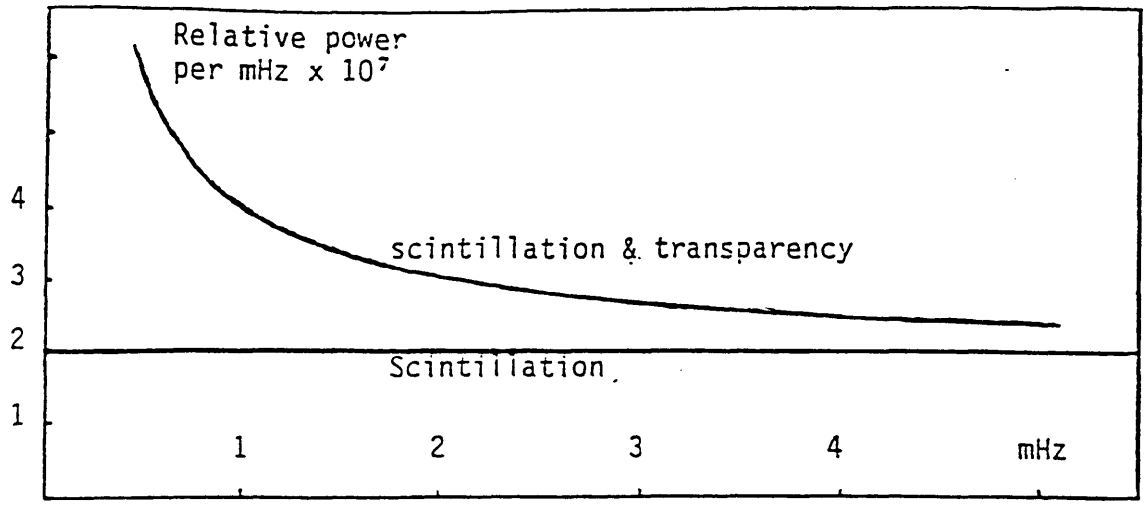


Figure 2.1: Typical power spectrum for all good photometric sites for 0.5–1 m telescopes [58]. Scintillation dominates for frequencies > 3 mHz, whilst for lower frequencies transparency fluctuations become more important.

at 33 mHz is $\approx 1.7 \times 10^{-5}$ mag, or about ten times the signal. This is about equal to the amplitude expected for higher mass stars, (see table 1.2), however their periods are predicted to be longer.

Reducing Photometric Noise

Telescope Diameter As has been previously stated, the power of the scintillation noise is proportional to $D^{-4/3}$, i.e. the scintillation's amplitude is approximately inversely proportional to the telescope diameter. Kurtz [59] has observed the star HD 101065 for two nights with both the 0.5 m (16.3 hr.) and the 1.5 m (15.4 hr.) at the SAAO. He found that the noise for frequencies above 3 mHz was reduced.

Unfortunately transparency fluctuations do not depend on telescope diameter. From the above observing runs, Kurtz found that the noise at 3 mHz was only marginally improved by the bigger telescope, and for lower frequencies, the noise was independent of telescope diameter.

Use of a Reference Star There is no gain in using a reference star to remove scintillation because of the small size of the temperature fluctuations causing the noise. To be effective the reference star would have to be within *1.7 arcseconds* of the target star [56, page 8].

Transparency fluctuations are correlated over tens of minutes of arc. Theoretically, there is an over 95% correlation between two stars separated by half a degree [56, page

18]. Unfortunately, there has not been any observational studies on the effectiveness of the removal of transparency fluctuations by two channel photometers [56, pages 27–28], but they have had a large amount of success being used to observe through clouds [56, page 27].

One situation where the use of a second channel would give false results is if the Moon was out. As the reference and target star are likely to be of differing magnitudes, the variations in sky brightness[3] affect them differently. This can be cured by using a third channel to monitor the sky brightness.

"Clever" Methods The best method of searching for Solar-type stellar oscillations using photometry would be to go into space. This would remove all the atmospheric noise, just leaving the inherent stellar noise. There have been several proposals along these lines.

It is possible that the star itself could be used as its own reference. If there are two 'wavelengths' for which the atmospheric noise is very highly correlated, but the intensity fluctuations have a lower correlation, then the oscillations could be subtracted out. These can be either, two distinct bands, or, for example the line cores, (where the intensity oscillations are supposed to be stronger), and the continuum. Frandsen used this method to observe β Hyi [60]. He used the ESO 3.6 m plus a fibre fed coudé spectrometer with a Reticon array. His spectral range was from 5160 Å to 5200 Å of which 335 pixels were counted as 'core', 1262 pixels continuum and the remaining 1870 were discarded. He obtained a power of about 2×10^{-5}. This was mainly due to poor seeing, (or too small a fibre), the read out noise of the Reticon, (which was comparable to the signal), and problems with the bias zero level, which stopped the scintillation noise being properly compensated for, (cf. the problems of sky brightness). Noyes used a similar method in his observations of ε-Eridani [26]. He used the emission cores of the H and K calcium lines, with two 20 Å wide strips of the continuum, (to the red and blue), as a reference.

2.2.2 Doppler Methods

The big advantage of measuring the radial velocity is that it enables the problems with atmospheric noise to be eliminated. In effect, it is like using the star as its own reference.

[3]Because of thin clouds, (if present), and a possible analogue to a 1% variation in sky brightness during the day [59]

Either one side of the line(s) are compared to the continuum or one side of the line(s) are compared to the other. By, preferably, observing both continually or, alternatively, chopping between the two positions faster than the cut-off frequency, ν_0, the effects of scintillation, sky transparency fluctuations and even thin clouds can be eliminated.

The big disadvantages are twofold: the spectrometer has to be incredibly stable and, as it is only using a small spectral range compared to a 'conventional' photometer, it either needs a large telescope or a very long time. Measuring radial velocities is also restricted by the number and type of lines that are available in certain, (usually hot), stars; narrow lines are generally better and either the radial velocity spectrometer could use a lot of lines or it needs very specific lines which are not necessarily present.

2.2.3 Summary

Table 2.2: Comparison of Radial Velocity and Luminosity Measurements for Detecting Solar-Type Oscillations.

Radial Velocity	
Advantages	Disadvantages
Negligible atmospheric noise.	Difficult instrumentation.
Can see the $l = 3$ mode.	Restricted range of stars.
Very low noise from the star.	Inefficient use of the available light.
Can tolerate quite bad seeing conditions.	

Luminosity	
Advantages	Disadvantages
Can be used for any stellar type.	Very restricted by atmospheric noise.
Simple instrumentation.	Only $l = 0$–2 modes visible.
Can use large amounts of the spectrum.	Needs 'photometric' seeing conditions.
	High stellar atmosphere noise.
	For maximum sensitivity need very large diameter telescopes (to reduce the scintillation noise).

On ground based photometry; *if* the calculations by Christensen-Dalsgaard and Frandsen [35], (and table 1.2), are correct, *if* the mode lifetimes are the same or longer than the Sun's, *if* enough observing time to resolve the modes could be had, (preferably on a large enough telescope to reduce the scintillation, combined with a reference star to reduce the sky transparency fluctuations), it might be just possible to observe Solar-type oscillations in some spectral types of star.

On radial velocity measurements; there are no intrinsic reasons why this should be impossible. It is a case of 'just' building a stable enough spectrometer and integrating for long enough. The problems are in the 'just'.

In conclusion, if the instrumental problems can be overcome, the most feasible way to do ground based asteroseismology is by measuring radial velocities. If they can't, astronomy will have to wait until there is a dedicated satellite, (for space borne photometry).

2.3 Methods of Measuring Radial Velocities

As this thesis is about building a stellar oscillation spectrometer a description of some other spectrometers that have been specially built, (or modified), to measure radial velocities follows.

2.3.1 Grating Methods

According to Griffin [61], the first measurements of stars' radial velocities were made by William Huggins in 1868 by visually comparing the displacement of Balmer lines with the spectrum from a hydrogen emission tube. Vogel, in 1892, measured radial velocities by superimposing the Hα line from a hydrogen discharge lamp onto the same photograph as the star's spectrum. By aligning the star's spectrum with a similarly treated spectrum from the Sun it was possible to find the star's radial velocity by measuring the relative displacement of the two Hα lines. Later developments with grating spectrographs led to an precision of about 1 km s^{-1} on reasonably bright stars.

The Griffin Radial Velocity Spectrometer

By recording the entire spectrum, the photographic method of measuring radial velocities spreads the information bearing light over many thousands of separate 'detectors', and, with the very low quantum efficiency of photographic emulsions, needs very long

exposures for all but the brightest stars. Griffin [61] developed a method for measuring radial velocities by making a 'diaphragm' from the spectrum of a star, (Arcturus), consisting of a series of apertures corresponding in position and width to the absorption lines. To measure the radial velocity of another star, the diaphragm was placed in the spectrometer and a lens was used to collect all the light passing through the apertures onto a photomultiplier. The diaphragm was then scanned across the stellar spectrum. When all the apertures were aligned with their corresponding absorption lines, the signal was at a minimum. By measuring the offset of the minimum it was possible to find the radial velocity of the star with respect to Arcturus. In just a six minute observation, on the 36″ Cambridge coudé reflector, it was possible to find the radial velocity of a star of down to 9th magnitude with an accuracy of up to 1 $\mathrm{km\,s^{-1}}$, which was equivalent to the best measurements then available.

A more modern instrument using the same technique is Coravel [62]. This uses an echelle in the Litrow mounting and is fixed at the Cassegrain focus. Again, Arcturus was used to make the diaphragm. However, so that an iron hollow cathode lamp can be used as the reference, the apertures corresponding to the iron absorption lines were narrowed to match the instrumental profile. On a 1 m telescope, Coravel is capable of giving better than 0.5 $\mathrm{km\,s^{-1}}$ for 13th magnitude stars in less than five minutes.

Problems in measuring velocities occur because of the mismatch between the stellar spectrum and the diaphragm. This occurs because the reciprocal of the dispersion is non-linear. According to Griffin [61] this does not give too great a problem for stars of the same spectral type as the star for which the diaphragm was made. However, stars with differing brightness distributions across their spectrum to Arcturus give greater emphasis to the spectral lines at one end of the spectrum or the other, so shifting the effective wavelength of the spectrum by about 300 $\mathrm{m\,s^{-1}}$, for a shift of 100 $\mathrm{km\,s^{-1}}$, in the most extreme spectral type of stars observed. In Coravel this problem is reduced because, as a cross-dispersed echelle is used, each order only stretches across a small percentage of the wavelength range, and the spectrum is shifted by moving the input slit rather than the diaphragm which causes a smaller error.

Improved Reference

Possibly one of the largest sources of error in finding accurate radial velocities is caused by the differences in illumination of the collimator by the star and the reference spec-

trum; for example: no secondary mirror hole in the reference beam, misalignment and non-uniformity both in the telescope and the reference optics and variations due to seeing and temperature gradients in the telescope. R. and R. Griffin [63] suggested that the telluric lines in the stellar spectrum could be used as standards: because they follow the same path as the stellar lines; are there all the time; are actually part of the spectrum, thereby eliminating the need to compare spectra; and are also absorption lines. Working from plates that had already been taken, without many of the precautions that they considered necessary and using water lines, errors of around 50 $\mathrm{m\,s^{-1}}$ were found on Arcturus and Procyon.

M. Smith [64] has obtained a precision of 6–11 $\mathrm{m\,s^{-1}}$ using a Reticon with a coudé spectrograph on a 107″ telescope on both Arcturus and Aldebaran. He used molecular oxygen lines around 6300 Å, believing that, as oxygen lines were formed over a greater path length than water lines they were less likely to suffer from wind speed and other atmospheric effects.

A modification of this technique by Campbell and Walker [65] achieved an accuracy of around 12 $\mathrm{m\,s^{-1}}$ on several stars by using a hydrogen fluoride absorption cell. The advantages of this method were that it removes problems with wind velocities and pressure changes in the atmosphere, strong reference lines can be produced by using a long cell, (for a 1 m long cell the hydrogen fluoride lines were 80% deep), and, by careful choice of gas, it was possible to have some choice in the position of reference lines. (This was one of the reasons why the very noxious hydrogen fluoride was chosen.) At one atmosphere pressure, hydrogen fluoride has a line width of 0.6 Å, which was easily resolvable with the spectrograph, so a lower pressure had to be used. A pressure of half an atmosphere was found suitable, which was achieved by connecting the cell to a vial of liquid hydrogen fluoride in iced water and relying on the vapour pressure at 0°C to keep the pressure stable to the 5 Torr necessary for 10 $\mathrm{m\,s^{-1}}$.

Libbrecht [23,42] had used the coudé spectrograph of the 200″ Hale telescope with an iodine absorption cell. Using the 72″ camera mirror and a Texas Instruments 800 × 800 CCD for a $\approx$ 55 Å range centred near 5350 Å he obtained a dispersion of 0.07 Å per pixel. A duty cycle of unity was obtained by reading out the CCD, "slowly and continuously".

On Procyon a one minute integration gave an error of 15 $\mathrm{m\,s^{-1}}$. After subtracting the Earth's spin etc., slow drifts of < 100 $\mathrm{m\,s^{-1}}$ were found. These correlated with

fluctuations of the iodine density, and hence with iodine temperature, as the cell was not temperature controlled. All the remaining errors were consistent with photon shot noise. Unfortunately, this was 'helped' by the low efficiency of the system; out of every 800 photons striking the primary, only *one* was detected. This was because of low spectrograph efficiency (2%), a loss of a factor of ten from bad seeing, (3 arcsecond cf. the 0.25 arcsecond slit width), and absorption in the iodine cell. Though improving the spectrograph and using an image slicer could improve the count rate by, maybe, up to six times, Libbrecht went on to say that the best way of improving the count rate would be to extend the wavelength range to several thousand Ångstroms, so giving an additional improvement in signal-to-noise of 5–10×'s. This would give problems as

> "the duty cycle on a bright star is quite low with current machines (say, 5 seconds to expose, followed by 45 seconds to read out)"

so fast read out CCD's would be necessary.

The problems common to all these methods are the need to find regions with both stellar and telluric (or gas) lines intermixed with only a few blends. This restricts the number of suitable lines, hence useable signal, and possibly puts them where the detector has a low quantum efficiency, necessitating long exposures. Long exposure times, of course, are more of a problem for photography. Photographic plates also give problems with long exposure times because of changes in the stars velocity caused by the rotation and orbit of the Earth.

2.3.2 Resonance Line Methods

Resonant Scattering Cells

The alkali metal vapour resonant scattering cell has been one of the most successful methods of observing the 'Sun as a star' i.e. looking for the global modes. Its use was first proposed by Isaak [66], who has been one of the most successful users of the technique [9,10,14,46,47], using a potassium cell. Fossat's Nice group have used a sodium based cell [8,44,67]. The major advantage of the resonant scattering method is that it provides a direct comparison of an absorption line with a laboratory wavelength without any intervening spectrometers, interferometers, etc.

Figure 2.2 shows the arrangement of the Birmingham spectrometer. The Sunlight from the Coelostat is first filtered to isolate a 15 Å bandwidth around 7698.9 Å. It is then

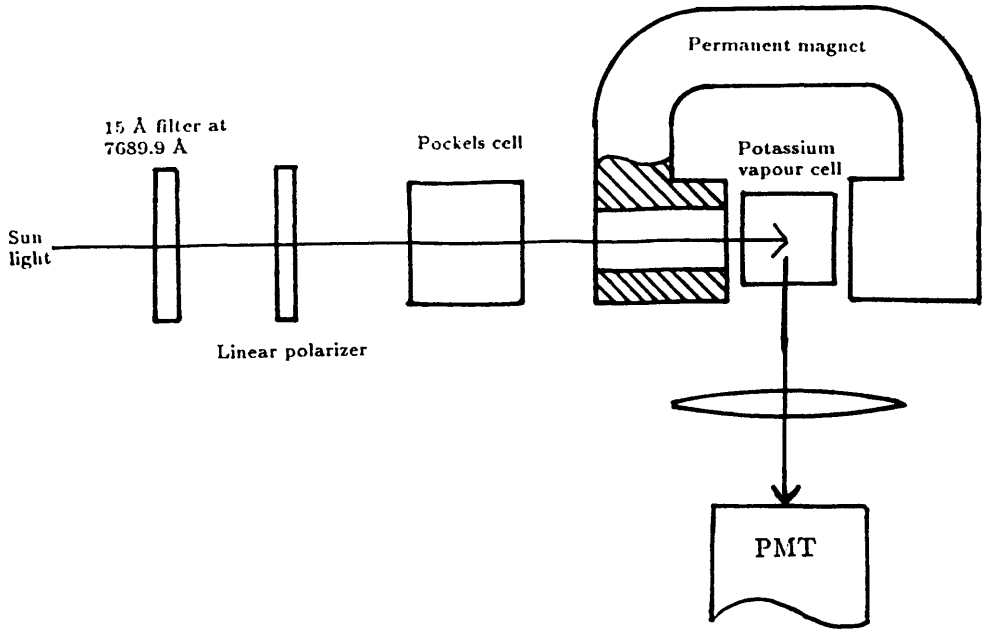


Figure 2.2: The Birmingham resonant scattering spectrometer

linearly polarized. After the polarizer, it passes through a Pockels cell. This converts the linearly polarized Sunlight to circular polarization. The Sunlight then passes into the potassium vapour cell. This sits in between the poles of a permanent magnet with the field lines lying parallel to the Sunlight. A photomultiplier sits perpendicular to the direction of the Sunlight and measure the amount of light being scattered from the potassium vapour. Because of the Zeeman effect, the resonant scattering cross-section is split symmetrically about the null position, with each component affecting one sense of circular polarization only. As the same potassium line is present in the Sun with a more or less negligible Doppler shift, each component samples one side of the line. So by chopping the Pockels cell, so that the sense of the circular polarization is reversed, first the signal from one side of the line, and then from the other, can be measured. Then from

$$V \propto \frac{N_{\mathrm{lcp}} - N_{\mathrm{rcp}}}{N_{\mathrm{lcp}} + N_{\mathrm{rcp}}}, \tag{2.3}$$

the radial velocity of the Sun can be found.

Magneto-Optic Filters—*MOF*

The big problem with the resonant scattering cell is its lack of 'transmission'. Even using the fastest lenses available, only a few per cent of the scattered light can be collected. Whilst this is not a problem for the Sun, for other stars, owing to the lack of photons, this is important. Fortunately this problem can be overcome by using a magneto-optic

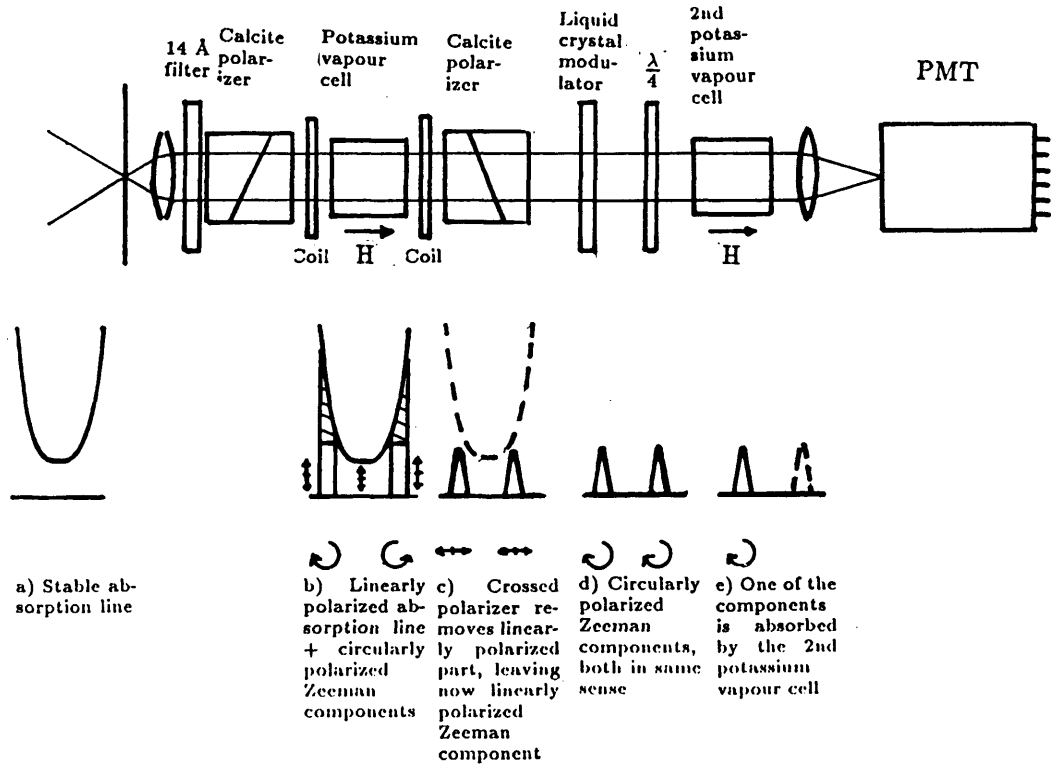


Figure 2.3: The magneto-optic filter

filter, *MOF*.

This was initially developed for measuring spatially resolved velocity and magnetic fields on the Sun [68]. This discussion is based on a type using two absorption cells containing potassium developed by the Birmingham group for stellar seismology (figure 2.3) which has been used to observe Procyon and Arcturus [39,69,70].

(The letters refer to figure 2.3) First of all the star light (a) passes through a 14 Å filter to isolate the potassium line, followed by a calcite polarizer to linearly polarize it. Next is the first potassium vapour cell. This is in a longitudinal field of 0.16 T provided by a permanent magnet. To provide calibration, the magnetic field is square wave modulated by ±3.44 T every 8 s by reversing a d.c. current through a pair of coils [71]. Any linearly polarized light can be considered to consist of two in phase, circularly polarized components, of equal intensity, but of opposite sense. Due to the Zeeman effect, the potassium line's absorption cross-section is split symmetrically about the middle of the potassium line, (cf. the resonant scattering cell), and absorbs the opposite sense of circular polarization at the two Zeeman wavelengths. Consequently, out of the potassium absorption cell comes the linearly polarized 'continuum', plus the two oppositely polarized lines at the Zeeman wavelengths (b). A second calcite polarizer,

crossed with the first, removes the continuum and linearly polarizes the two Zeeman components (c).

The two now linearly polarized lines are converted to circular polarization using a liquid crystal modulator and a quarter-wave plate. The beam now consists of two circularly polarized (in the same sense) lines at the Zeeman wavelengths (d). They then go through a second potassium cell, in which one of the components is absorbed and the other transmitted (e). By switching the direction of linear polarization out of the liquid crystal, it is possible to swop the sense of the circular polarization. This means that the other Zeeman component is transmitted, which gives two signals on either side of the stellar absorption line, similar to equation 2.3, so enabling the radial velocity to be measured.

There are other possible arrangements that have been used for MOF's, by for example Schmider *et al.* [38], who use a single sodium cell, and Cacciani [72], who uses a single sodium cell, but double passes it, using a mirror.

The main problem with all the methods that rely on resonance with a laboratory line is that they are only useful on a restricted number of stars. This is because the particular line must be present in the star and the laboratory wavelength must overlap with the Doppler shifted wavelength of the star, The latter constraint can be partially overcome for stars near the ecliptic with radial velocities of $\lesssim 20\ \mathrm{km\,s^{-1}}$ by using the Earth's orbital velocity to bring the stellar line within the passband of the 'filter'. This means that the star can only be observed for a few weeks (≈ 2–3) every year.

2.3.3 Interferometric Methods

PEPSIOS

Traub *et al.* [73] made one of the first attempts to search Solar-type oscillations in other stars. They used their PEPSIOS spectrometer on the Smithsonian 1.5 m telescope in June and December of 1976. PEPSIOS [74] is a three etalon Fabry-Perot spectrometer. It was pressure scanned using nitrogen gas. Each etalon was in a sealed container connected to the previous one by differential pressure controllers. For scanning, a fixed-path Michelson interferometer was used to monitor the pressure changes by counting mercury fringes. After an interference filter, used to isolate the absorption line, but before the etalon, a sheet of plane glass was used to monitor the 'continuum' to provide a reference to enable scintillation etc. to be removed.

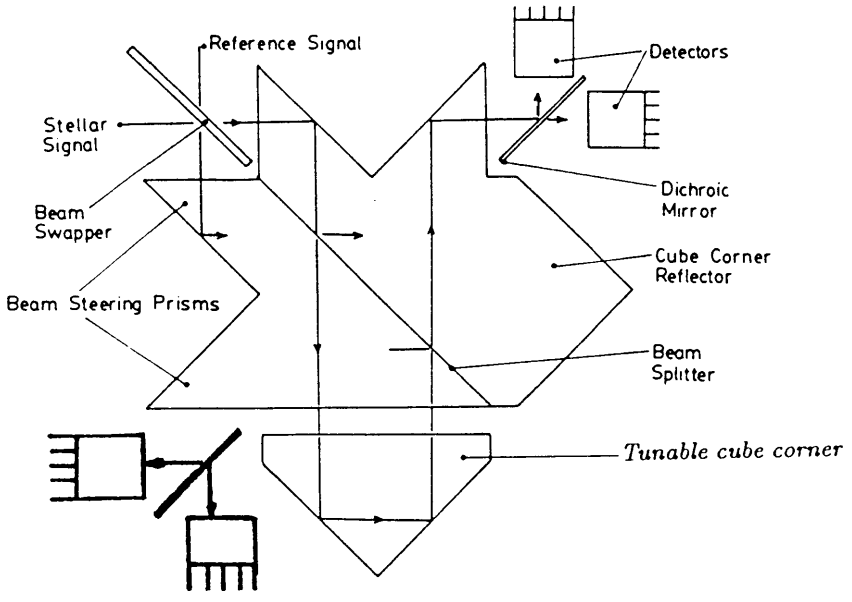


Figure 2.4: The Imperial College Michelson *ISOS*

For searching for Solar type oscillations, the PEPSIOS passband was set at the half-intensity point of the Fe I line. The instrumental passband had a full width at half-maximum (FWHM) of about 0.067 Å. For most of the stars it gave a 25% deep line profile of FWHM 0.027 Å.

Several of the brighter stars visible from the northern hemisphere were observed, usually for quite short periods, (of typically 45 to 90 minutes), giving noise levels of about 10 $\mathrm{m\,s^{-1}}$. Arcturus and ϵ Cygni were observed for longer, ($\approx$ 12 and $\approx$ 7 hours respectively), with a better photomultiplier, to give noise levels of 1 and 3 $\mathrm{m\,s^{-1}}$ respectively. All of their Fourier transforms had been smoothed with a running average of 1 mHz. No stellar oscillations were found, but noise from the telescope drive appeared in a number of the observing runs.

The Sun was also observed by using a white-painted flat surface at 45° to the telescope axis in front of the secondary and pointing the telescope 90° from the Sun, so giving integrated sunlight. In a 85 minute run they found a peak at 3.32 mHz with an amplitude of 1.6 ± 0.5 $\mathrm{m\,s^{-1}}$.

The Michelson *ISOS*—Interferometric Oscillation Stellar Spectrometer

The Michelson *ISOS* was developed at Imperial College by Forrest [75,76]. It is field-widened, has two input and output ports, and is optically stabilized. It was made out of solid glass components for reasons of robustness and stability. The main body of the

interferometer consisted of two 45° prisms, cemented hypotenuse to hypotenuse. One of the two hypotenuses was coated with a semi-reflecting layer of silver. Silver was used, even though it has higher absorption than aluminium, as it was possible to have a coating in between two layers of glass, which could reflect and transmit both polarizations of light very nearly equally. (As opposite polarizations cannot interfere, the beam-splitter has to have 50:50 transmission and reflection in each polarization, rather than 90:10 in perpendicular and visa-versa in parallel polarized light.) Rather than scanning the line, it searched for changes in radial velocity by observing the phase of the $\cos^2$ fringes at a fixed path length. As the wavelength changed, the output intensity varied.

Using a longer path length would have made the variations more rapid. Unfortunately, because of the finite width of the absorption line, it would also have reduced the amplitude of the fringes. The optimum path length was found to be 5.5 mm, giving a resolution of 0.1 Å. To isolate the absorption line, a 1.5 Å pre-filter was used. The fringes from the pre-filter have a large amplitude only near zero path difference, hence the instrument is relatively insensitive to pre-filter drift.

All Michelson Interferometers have two output (and input) ports. In a 'normal' Michelson, half the light is reflected back along the input beam. In the Michelson *ISOS* two cube corners were used instead of plane mirrors. As well as reflecting the beams, they displace them, so making both output beams accessible. The two beams were the complements of each other, hence, the radial velocity could be found by measuring the ratio $(C - D)/(C + D)$, where C and D were the counts from the star in the two output ports. This not only reduced the photon shot noise, it also reduced the noise from scintillation, transparency variations and even thin cloud.

To stabilize the Michelson, an optical reference, using the cadmium red line, was necessary. One of the cube corners was mounted on piezo-electric stacks. By measuring the ratio, $(A - B)/(A + B)$, of the two cadmium red output beams, the position of the cube corner could be altered to keep the path difference constant. The reference line was isolated from the stellar line using dichroic beam-splitters The movable cube corner also allowed the Michelson to be scanned for a few fringes, so enabling the path difference at which the null-point of the reference signal coincided most closely with the maximum slope of the stellar signal to be used.

The value of the air-gap produced by mounting one of the cube corners on piezo-electric stacks was selected to provide field-widening (see Appendix A). This had the

advantage that it reduced sensitivity to the input beam position. To reduce it still further, and to allow the Michelson to be used off the telescope, an optical fibre was used.

As well as two output apertures, the Michelson *ISOS* had two input apertures. By swopping the input beam between the two input apertures, the two output beams were also swopped between the two output apertures, (and hence the two photon counting channels). This reduced errors caused by drifts in the photomultipliers and/or electronics. The beams were swopped using a rapidly rotating disc, one half of which was silvered.

The Michelson *ISOS* was controlled using a Rockwell AIM 65 microcomputer, (latterly a single board computer based system, plus BBC microcomputer). The microcomputers were able to do a Fourier transform of the last 256 points taken as a quick-look facility. The data was stored on digital cassette using either a Cristie CS5 or 6. From figures given in [77] it has obtained noise levels of about 4 $\mathrm{m\,s^{-1}}$ on a number of stars.

Fabry-Perot *ISOS*

This was developed at Imperial College by Pietraszewski [78]. It consisted of a Queensgate Instrument CS100 capacitance servo system driving an ET28 etalon mounted in a temperature controlled pressure pot. By putting it in a pressure pot the sensitivity of the etalon to temperature was reduced to 75 $\mathrm{m\,s^{-1}\,^{\circ}C^{-1}}$. However it was controlled to 0.01°C to remove drifts in the filter and from temperature gradients causing distortion in the etalon plates. The line was isolated by a 10 Å filter which could be tilt-tuned in wavelength. Again the instrument was fibre fed for similar reasons to the Michelson. The etalon was controlled from an AIM 65 microcomputer and was chopped on the points of inflection of the absorption line at a rate of 4 or 5 Hz to reduce changes in the signal brightness due to guiding, seeing, clouds etc. and the counts from several chops on each point summed. Again, to give the radial velocity signal, $(C - D)/(C + D)$ was worked out, where C and D are the counts from the two points of inflection. A noise of 30 $\mathrm{m\,s^{-1}}$ was obtained on α Car [79].

Chapter 3

Defining the Instrument

The first part of this chapter shows why many spectral lines are needed to obtain sub-metre per second radial velocity measurements, even on the brightest stars. This is followed by a discussion on how this can be achieved whilst still maintaining the necessary degree of stability in a radial velocity spectrometer. Having concluded that this can best be done using a multiple-line interferometer, the final section investigates some of the problems involved in this.

3.1 The Need for Multi-lining

Consider a triangular shaped absorption line of full width half maximum d, of fractional depth D, of wavelength λ_0 (figure 3.1). The signal from an interferometer with rectangular pass band of width d, centred at λ_1 or λ_2 is equal to

$$A \text{ or } B = \left[1 - \frac{D}{2}\right] Id, \tag{3.1}$$

where

$$I = \frac{n}{(2-D)d} \tag{3.2}$$

and

$$A = B = \frac{n}{2}. \tag{3.3}$$

Let there be a change in velocity of δv, giving a Doppler shift of $\delta\lambda$, (figure 3.1). The new values for A and B are

$$A' = A - (1-D)I\,\delta\lambda - \frac{DI}{2d}(\delta\lambda)^2 + I\,\delta\lambda \tag{3.4}$$

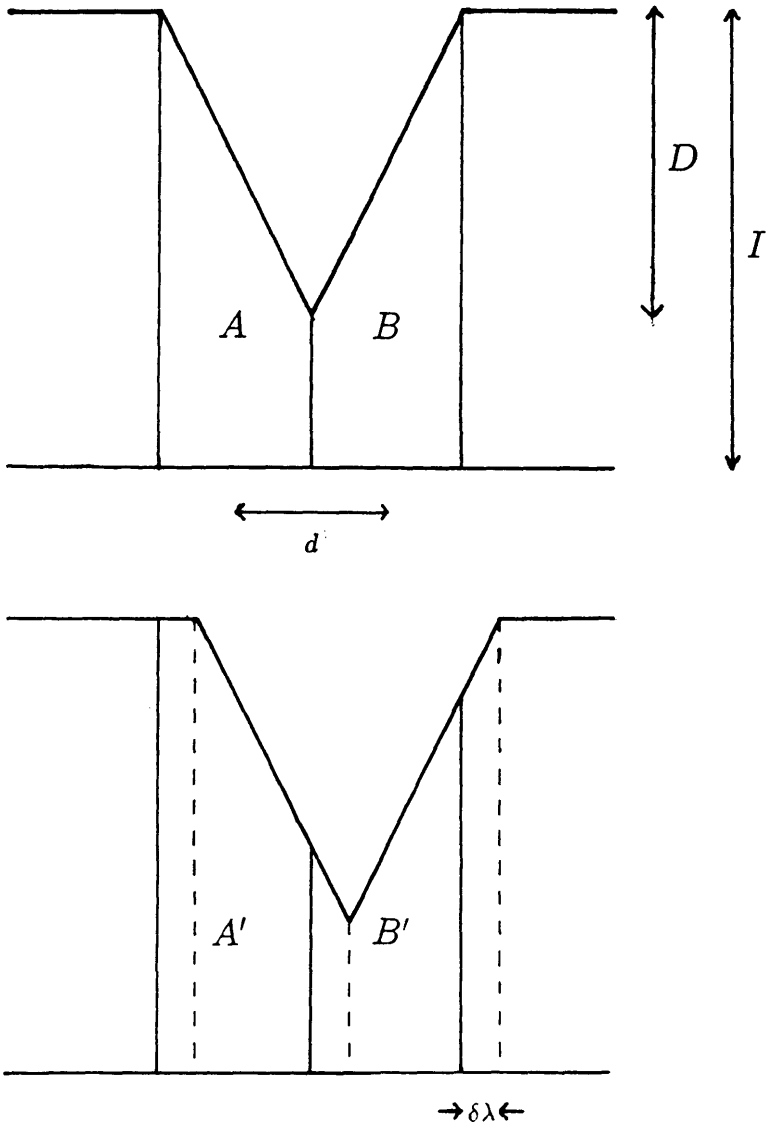


Figure 3.1: Triangular absorption line.

and

$$B' = B + (1 - D)I\,\delta\lambda + \frac{DI}{d}(\delta\lambda)^2 - I\,\delta\lambda. \tag{3.5}$$

What is required is

$$r = \frac{A' - B'}{A' + B'}. \tag{3.6}$$

$$A' - B' = 2DI\,\delta\lambda - \frac{3DI}{2d}(\delta\lambda)^2 \tag{3.7}$$

and

$$A' + B' = A + B + \frac{DI}{2d}(\delta\lambda)^2. \tag{3.8}$$

As $\delta\lambda$ is very small, terms in $(\delta\lambda)^2$ can be ignored, hence

$$\frac{A' - B'}{A' + B'} = \frac{2DI\,\delta\lambda}{A + B}. \tag{3.9}$$

By Poisson statistics the error in A or B is the square root of the number of counts, i.e.

$$\sigma_A = \sqrt{A}, \tag{3.10}$$

$$\sigma_B = \sqrt{B}. \tag{3.11}$$

Hence, (see Bevington [80]),

$$\sigma_r^2 = \sigma_A^2 \left[\frac{\partial r}{\partial A}\right]^2 + \sigma_B^2 \left[\frac{\partial r}{\partial B}\right]^2, \tag{3.12}$$

$$\sigma_r^2 = \sigma_A^2 \left[\frac{2B}{(A+B)^2}\right]^2 + \sigma_B^2 \left[\frac{-2A}{(A+B)^2}\right]^2. \tag{3.13}$$

Substituting for σ_A and σ_B from equations 3.10 and 3.11,

$$\sigma_r^2 = \frac{4AB^2 + 4BA^2}{[(A+B)^2]^2}. \tag{3.14}$$

However $A \approx B \approx n/2$, where n is the total number of counts for the two chop positions, therefore,

$$\sigma_r^2 = \frac{\frac{1}{2}n^3 + \frac{1}{2}n^3}{n^4}, \tag{3.15}$$

$$\sigma_r = \frac{1}{\sqrt{n}}. \tag{3.16}$$

Hence, to find the signal equivalent to the noise, the change in ratio is equated to the error i.e.

$$\frac{1}{\sqrt{n}} = \frac{2DI\,\delta\lambda}{n}, \tag{3.17}$$

substituting for I gives

$$\frac{1}{\sqrt{n}} = \frac{2D\,\delta\lambda}{(2 - D)d} \tag{3.18}$$

or

$$n = \left[\frac{(2-D)d}{2D\,\delta\lambda}\right]^2. \tag{3.19}$$

In a typical case of a 0.3 Å wide, 50% deep line, to obtain a noise equivalent to under 10 cm s^{-1}, requires almost 10^{11} counts. For a 4 m telescope, using the standard formula of

> a thousand counts per second per square centimetre per ångstrom from a 0 magnitude star[1].

and an instrumental efficiency of 1%, it requires over nine nights of observations on a 0 magnitude star to obtain this! Obviously this is extremely expensive in telescope time. By using, however, just nine lines, (with the same instrumental efficiency, of course), a noise level which would need at least nine clear nights on one of the largest telescopes available, can just about be obtained in one nights observations.

3.2 The Radial Velocity Spectrometer

3.2.1 Preamble

From section 2.3 the different types of radial velocity spectrometers can basically be divided into two types:

1. Those that use large parts of the spectrum to give accuracies of 10–100's of metres per second in a few minutes.
2. Those which use one (or two) lines, to give a potential precision of under a metre per second, but need integrations of several nights.

The aim of the project was to develop an instrument which, whilst using many lines, would be as stable as the single line instruments.

Though work is being done on using more than one element in *MOF* type instruments, this will be limited by the need to find elements which can form a vapour under similar conditions. At the moment attempts are being made to use sodium and potassium together [72]. As it is unlikely that many more than these two elements will be able to be used together,[2] for the stable part of the instrument an interferometer is the most practicable option.

[1] Actually from a F0 star at 5000 Å either 1014 [81] or 1074 [82, page 207].

[2] Although it should be possible to pre-disperse the spectrum and use multiple absorption cells.

3.2.2 Some Methods for Multi-lining a Radial Velocity Interferometer

Most methods that have been used or are under development rely on post-dispersion; that is taking the output from the interferometer, and dispersing it onto a multi-element detector like a CCD. One method, which is being developed by Butcher and Hicks [83], is to use a very stable Fabry-Perot to act as a reference for an echelle plus CCD detector. Instead of using the Fabry-Perot in transmission, they intend to reflect the star light off the interferometer before feeding it into an echelle spectrometer. As the reflected spectrum from a Fabry-Perot is the complement of that transmitted, the stellar spectrum will have superimposed on it a series of reflection minima from the Fabry-Perot. This method is analogous to the grating plus telluric or HF absorption line methods, with the reflection minima acting as pseudo-absorption lines. It has the advantage that by correct choice of the Fabry-Perot coatings and gap, the pseudo-absorption lines can be placed anywhere in the stellar spectrum, at (almost) any desired frequency, and can extend for at least 1000 Å. It is obviously limited by the stability of the Fabry-Perot and the CCD detector, with the latter, (according to Butcher and Hicks), being the limiting factor, leading to a velocity resolution of a few metres per second.

It would obviously be possible to do something similar with the Imperial College Michelson *ISOS*, either using a multi-element detector or some kind of mask, to isolate regions where absorption lines coincide with the correct part of the Michelson fringes. However as the Michelson *ISOS* is a twin-beam instrument it would mean that two spectrometer/detector systems would be needed so adding to the complication and cost.

Generally for post-dispersion, some form of multi-element detector has to be used. These are expensive, have problems with dimensional stability and varying sensitivity of the pixels and, if a large number of lines are to be used, hence a large number of elements, require powerful computing facilities. Consequently it was decided to investigate pre-dispersion or dispersing the light before it is fed into the interferometer.

Using Pre-dispersion with a Radial Velocity Interferometer

In a typical interferometer the wavelength transmitted usually depends on gap and angle. For a constant gap it is possible to transmit any wavelength by varying the angle

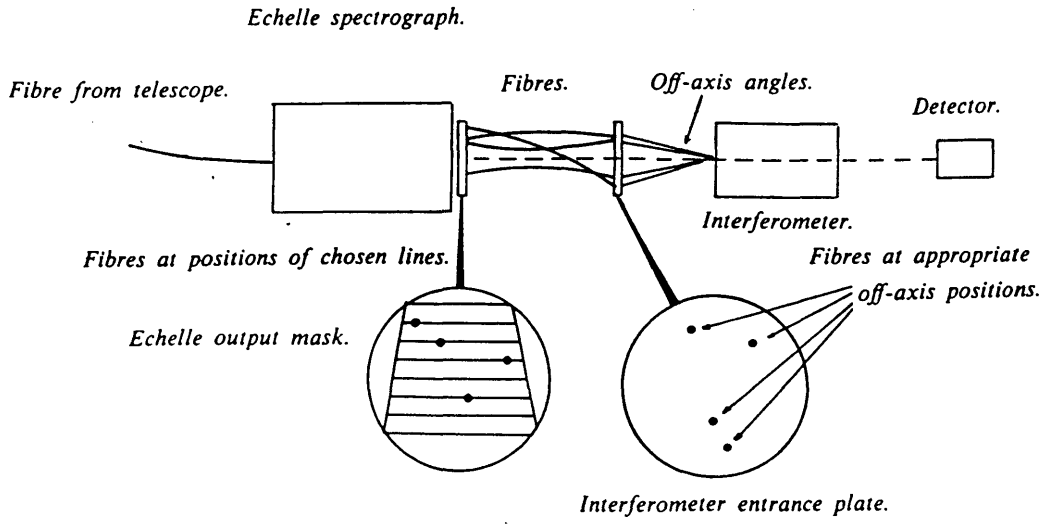


Figure 3.2: Keeping the phase constant for different wavelengths by introducing them at differing angles.

the light is fed in at; for example, in a Fabry-Perot interferometer

$$m\lambda = 2d\cos\theta \tag{3.20}$$

where λ is the wavelength, m the order, d the gap and θ the angle.

Normally the interferometer is used on-axis with a single input aperture. However if the stellar light could be pre-dispersed, and each stellar line introduced at its correct input angle, all the lines could be transmitted simultaneously. This can be done by taking a spectrometer and putting an optical fibre at the position of each selected absorption line. Then, whilst keeping the interferometer at constant gap, positioning each optical fibre at the correct angle for its particular wavelength (figure 3.2). Thus, the interferometer acts as a sort of diaphragm, as in the Griffin type radial velocity spectrometers, so enabling a single detector to be used.

3.3 Design Considerations

As has been stated before, Imperial College has been involved with both Fabry-Perot and Michelson radial velocity interferometers. It is proposed to discuss both their requirements for the following:

- Is the phase maintained with differing intrinsic stellar radial velocities?

- What is the largest size of fibre that can be used for an interferometer with a given resolution-luminosity product?
- The positional tolerances of the optical fibres.

A qualitative discussion on the pre-disperser then follows. As this project is concentrating on the Fabry-Perot there is then a more detailed discussion on the optimum resolution and pre-disperser sizes for different stellar line widths for use with the Fabry-Perot.

3.3.1 Maintenance of Phase with Radial Velocity Change

The Griffin-type radial velocity spectrometer only maintains alignment between the stellar absorption lines and the slits in the diaphragm for stars of the same radial velocity. Even with a precision of a few hundred metres per second, this leads to errors for extreme stellar types. For sub-metre per second measurements this would be unacceptable. Therefore, so that the same arrangement of fibres can be used for many different stars, it is important that the Doppler shift of all the absorption lines from the fibres can be corrected for by the *same* change in gap in the Fabry-Perot or path difference in the Michelson.

Fabry-Perot

For an on-axis ray in the Fabry-Perot

$$m\lambda_0 = 2d \tag{3.21}$$

and for an off-axis ray,

$$m\lambda_1 = 2d\cos\theta. \tag{3.22}$$

A change in the velocity of the star of v, changes the wavelength to

$$\lambda_0' = \lambda_0\left[1+\frac{v}{c}\right] \tag{3.23}$$

and

$$\lambda_1' = \lambda_1\left[1+\frac{v}{c}\right], \tag{3.24}$$

becoming

$$m_0\lambda_0' = 2d' \tag{3.25}$$

and

$$m_1\lambda_1' = 2d''\cos\theta, \tag{3.26}$$

for constant θ. For the phase to be maintained d' must equal d''. Substituting for equation 3.21 in equation 3.22,

$$m_1\lambda_1 = m_0\lambda_0\cos\theta \tag{3.27}$$

and multiplying both sides by $(1 + v/c)$ gives

$$m_1\lambda_1' = m_0\lambda_0'\cos\theta. \tag{3.28}$$

Therefore by substituting 3.25 in 3.28,

$$m_1\lambda_1' = 2d'\cos\theta, \tag{3.29}$$

i.e. $d' = d''$ and the phase is maintained for changing radial velocity.

The Michelson

In the Michelson in air,

$$\lambda_0 = \frac{2\pi\Delta}{\psi}, \tag{3.30}$$

$$\lambda_1 = \frac{2\pi\Delta}{\psi}\cos\theta, \tag{3.31}$$

where ψ and Δ are the phase and path differences respectively. For the same change in velocity, v, equations 3.30 and 3.31 become, (for constant ψ);

$$\lambda_0' = \frac{2\pi\Delta'}{\psi}, \tag{3.32}$$

$$\lambda_1' = \frac{2\pi\Delta''}{\psi}\cos\theta. \tag{3.33}$$

Substituting λ_0 in equation 3.31 gives

$$\lambda_1 = \lambda_0\cos\theta. \tag{3.34}$$

Hence, by multiplying both sides by $(1 + v/c)$

$$\lambda_1' = \lambda_0'\cos\theta \tag{3.35}$$

and substituting for λ_0'

$$\lambda_1' = \frac{2\pi\Delta'}{\psi}\cos\theta, \tag{3.36}$$

i.e.

$$\Delta'' = \Delta' = \Delta(1 + v/c). \tag{3.37}$$

The above arguments demonstrate that both instruments are suitable for observing stars with differing Doppler shifts.

3.3.2 Resolution-Luminosity Product—the Maximum Useable Input Aperture

One of the major advantages of interferometers over grating spectrometers is that for the same resolution, in the same size instrument a larger input aperture can be used [84]. However, this is only true for the on-axis case, for off-axis angles the size of the useable input aperture normally falls off rapidly with increasing angle.

The Fabry-Perot

The finesse of an etalon is dependant on several factors, e.g.

$$N^2 = N_r^2 + N_d^2 + N_a^2, \tag{3.38}$$

where N_r, N_d, and N_a are the finesses due to the reflectivity, defects and input aperture respectively [85]. The usual criterion for optimum loss of finesse caused by any one factor is for it to approximately match that caused by any other factor; i.e.,

$$N_r \approx N_d \approx N_a; \tag{3.39}$$

there is no point in using extremely flat (and expensive) plates, (i.e. high defect finesse), with coatings that have low reflectivity, (i.e. low reflectivity finesse). In fact, having too high a finesse because of the reflectivity can cause a loss in transmission. However it is not unusual to use a smaller than maximum aperture to give some leeway in construction, stability etc. Similarly, the loss of finesse from using off-axis fibres is only tolerable if it is equal to or (preferably) less than that of the etalon, which should be equal to (or slightly better than) the required finesse.

As the transmission maxima of the Fabry-Perot repeat, it is only necessary to be able to move the fibres off-axis enough to cover the wavelengths in between any one on-axis transmission maximum and the next.

From $m\lambda = 2d\cos\theta$, by differentiation,

$$\frac{d\lambda}{d\theta} = -\frac{2d\sin\theta}{m} \tag{3.40}$$

or

$$\sin\theta = -\frac{m}{2d}\frac{d\lambda}{d\theta}, \tag{3.41}$$

($d\lambda$ being equivalent to the resolution of the etalon and $d\theta$ the angular width of the fibre). However for the on-axis wavelength λ_0,

$$\lambda_0 = \frac{2d}{m}, \tag{3.42}$$

therefore

$$\theta \approx \frac{1}{\lambda}\frac{\mathrm{d}\lambda}{\mathrm{d}\theta} \tag{3.43}$$

i.e. the maximum useable off-axis *angle* depends only on the required resolution and the angular size of the input aperture, and is independent of gap.

The inter-order distance needed is dependent on the maximum width of the filter profile. Obviously to stop overlapping orders the inter-order distance must be greater in width than the filter profile.

By taking

$$m\lambda = 2d, \tag{3.44}$$

and

$$(m+1)\lambda' = 2d, \tag{3.45}$$

and then subtracting gives

$$m(\lambda' - \lambda) - \lambda' = 0 \tag{3.46}$$

or

$$m = \frac{\lambda'}{\lambda' - \lambda} = \frac{\lambda'}{\Delta\lambda}, \tag{3.47}$$

(where $\Delta\lambda$ is the inter-order distance). Hence, the order, m, is found, which allows the gap to be calculated;

$$d = \frac{m\lambda}{2}. \tag{3.48}$$

From the inter-order distance and the desired resolution, the required finesse can be found,

$$N = \frac{\Delta\lambda}{\delta\lambda}. \tag{3.49}$$

The maximum necessary off-axis angle is found from

$$m\lambda_0 = 2d, \tag{3.50}$$

$$(m-1)\lambda_0 = 2d\cos\theta_{\max}. \tag{3.51}$$

Subtracting gives

$$\lambda_0 = 2d(1 - \cos\theta_{\max}) \approx \theta_{\max}^2 d \tag{3.52}$$

or

$$\theta_{\max} \approx \sqrt{\frac{\lambda_0}{d}}. \tag{3.53}$$

The maximum angular diameter of the fibre is given by rearranging equation 3.43,

$$\mathrm{d}\theta = \frac{1}{\theta_{\max}}\frac{\mathrm{d}\lambda}{\lambda_0} \tag{3.54}$$

and substituting for $\theta_{\max}$,

$$\mathrm{d}\theta = \frac{\mathrm{d}\lambda}{\lambda_0}\sqrt{\frac{d}{\lambda_0}}. \tag{3.55}$$

Therefore, if the fibre diameter is fixed, then the required focal length of the collimator can be found from

$$F_{\text{collimator}} = \frac{\phi_{\text{fibre}}}{\mathrm{d}\theta}, \tag{3.56}$$

which gives the diameter of etalon needed,

$$\phi_{\text{etalon}} = \frac{F_{\text{collimator}}}{\text{fno}_{\text{fibre}}}. \tag{3.57}$$

The Michelson

One of the major advantages that the Michelson interferometer, (e.g. the Imperial College Michelson *ISOS*), can have is that it can be field-widened, i.e. it would have a much larger input aperture than a 'classical' interferometer of the same size. Field widening, of course, means that there is only a minute change in wavelength with angle over the input aperture. For a solid Michelson with an air gap of e in one of the beams, (see Appendix A), this is given by

$$\Delta_i = 2[e(n\cos i - \cos r) + nd\cos i] \tag{3.58}$$

where d is the physical difference in the position of the two mirrors, which, if

$$e = \frac{d}{n-1} \tag{3.59}$$

$$\Delta_i \approx \Delta_{i=0^\circ} \tag{3.60}$$

i.e. the condition for field-widening. This allows the field widened Michelson to be used with almost any diameter fibres. The corollary, of course, is that it then becomes unsuitable for an instrument that relies on a variation of wavelength with input angle! By displacing one of the cube corners, however, it is possible to introduce a path difference with angle, (in one direction), which is proportional to the product of the sine of the off-axis angle (i_x) times the distance the cube corner has been displaced (x) [75], i.e.

$$\begin{aligned} \Delta_i = \; & 2[e(n\cos i - \cos r) + nd\cos i] && (\equiv \Delta_{i=0^\circ}) \\ & + x\sin i_x && (\equiv \Delta_{i_x}) \end{aligned} \tag{3.61}$$

or

$$\delta\Delta_i \approx \Delta_{i_x} = x\sin i_x, \tag{3.62}$$

where x is the cube corner's displacement and i_x is the angle of incidence in the direction of displacement. To enable the Michelson to transmit any wavelength, it is necessary to displace the cube corner enough to give a 360° phase change across the input aperture; i.e. the phase change across the input aperture is given by

$$\frac{2\pi x \sin \pm i_{\max}}{\lambda} = \pm\pi \tag{3.63}$$

or

$$\Delta_{i_{\max}} = x \sin \pm i_{\max} = \pm\frac{\lambda}{2}. \tag{3.64}$$

This produces a linear phase shift, which means that there is a constant $\mathrm{d}\lambda/\mathrm{d}i$ across the aperture. Hence, to a first approximation, there is no reduction in resolution, (for constant aperture size), with position. Combined with the large apertures produced by field-widening, this allows any reasonable sized fibre to be used across a large enough aperture to fit many of them. (In fact the major limitation on input size is vignetting inside the interferometer.) This is the big advantage of the Michelson.

3.3.3 Fibre Positioning Accuracy

It is important to know the effects of misalignment in the position of the optical fibres in the two interferometers, so that some idea of the positioning tolerances and sensitivity to drifts can be found. For both the Fabry-Perot and Michelson interferometers, the misalignment for which the addition of a second line causes a loss of signal, (compared with the single line case), is found.

The Fabry-Perot

Consider figures 3.3a, b, and c. Figures 3.3a and b are a very simplified representation of Fabry-Perot passbands convolved with absorption lines. Figure 3.3c represents the sum of the two with them misaligned by an error, e. The passbands a_1, a_2, b_1 and b_2 are given by, (using the previous notation),

$$a_1 = b_2 = Id - \frac{IDd}{2} \tag{3.65}$$

and

$$b_1 = a_2 = Id - \frac{ID}{2d}[d^2 + 2ed - e^2]. \tag{3.66}$$

The passbands A and B are just given by $a_1 + a_2$ and $b_1 + b_2$ respectively. Again consider a small change in wavelength $\delta\lambda$. This gives

$$a_1' = a_1 + ID\,\delta\lambda - \frac{ID}{2d}(\delta\lambda)^2, \tag{3.67}$$

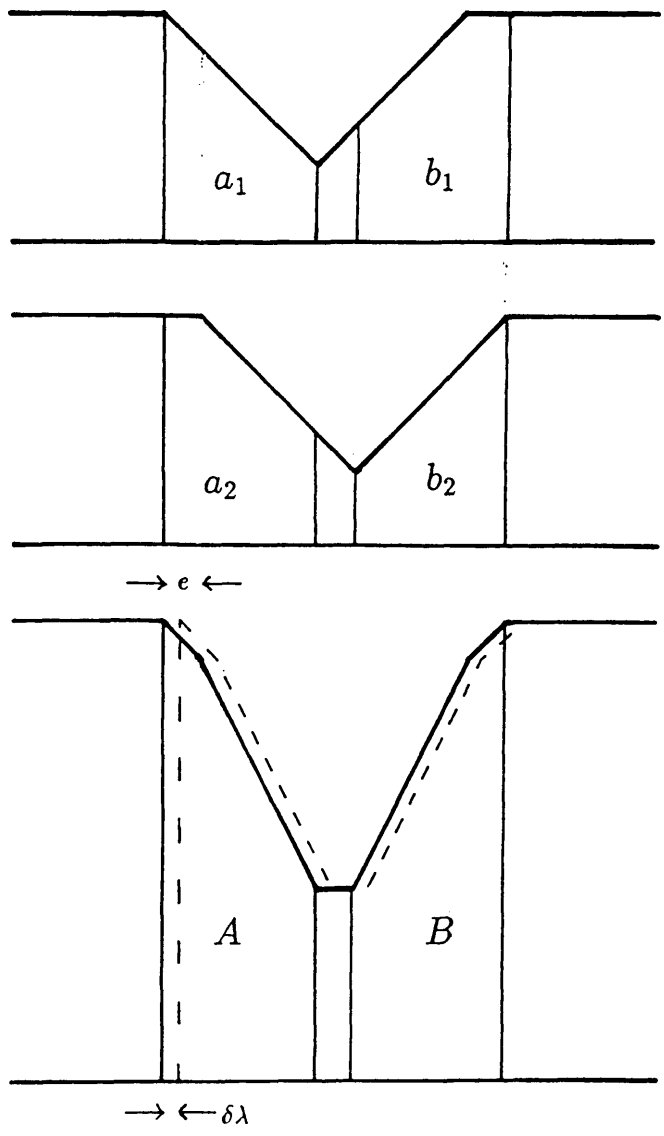


Figure 3.3: Errors in alignment of the fibres in the Fabry-Perot.

$$b_1' = b_1 - \left[1 - \frac{e}{d}\right] ID\,\delta\lambda - \frac{ID}{2d}(\delta\lambda)^2, \tag{3.68}$$

$$a_2' = a_2 + \left[1 - \frac{e}{d}\right] ID\,\delta\lambda - \frac{ID}{2d}(\delta\lambda)^2, \tag{3.69}$$

$$b_2' = b_2 - ID\,\delta\lambda + \frac{ID}{d}(\delta\lambda)^2, \tag{3.70}$$

with the pass bands A and B being given by

$$A' = a_1 + a_2 + \left[2 - \frac{e}{d}\right] ID\,\delta\lambda - \frac{ID}{d}(\delta\lambda)^2, \tag{3.71}$$

$$B' = b_1 + b_2 - \left[2 - \frac{e}{d}\right] ID\,\delta\lambda + \frac{ID}{2d}(\delta\lambda)^2. \tag{3.72}$$

Ignoring terms in $(\delta\lambda)^2$,

$$A' - B' = 2\left[2 - \frac{e}{d}\right] ID\,\delta\lambda \tag{3.73}$$

and

$$A' + B' = a_1 + a_2 + b_1 + b_2 \approx 2n. \tag{3.74}$$

Therefore,

$$\frac{A' - B'}{A' + B'} = \left[2 - \frac{e}{d}\right] \frac{ID}{n}\,\delta\lambda. \tag{3.75}$$

Similarly to equation 3.17, equating the ratio to the error caused by photon statistics,

$$\left[2 - \frac{e}{d}\right] \frac{ID}{n}\,\delta\lambda = \frac{1}{\sqrt{2n}}. \tag{3.76}$$

Therefore the noise equivalent wavelength is given by

$$\delta\lambda_{2\text{ lines}} = \frac{\sqrt{n}}{[2 - e/d]ID\sqrt{2}}. \tag{3.77}$$

Equating this to the similar quantity for one line from equation 3.17 gives

$$\frac{\sqrt{n}}{[2 - e/d]ID\sqrt{2}} = \frac{\sqrt{n}}{2ID} \tag{3.78}$$

or

$$e = d(2 - \sqrt{2}) \approx 0.59d. \tag{3.79}$$

i.e. the fibre must be positioned to better than approximately half of the line width. A not too surprising result. The fractional improvement is given by

$$\frac{2 - \sqrt{2} - e/d}{2 - \sqrt{2}}. \tag{3.80}$$

Hence , $\approx$ 90% of the maximum improvement can be had if the lines are aligned to within a $\frac{1}{20}$ of the line width.

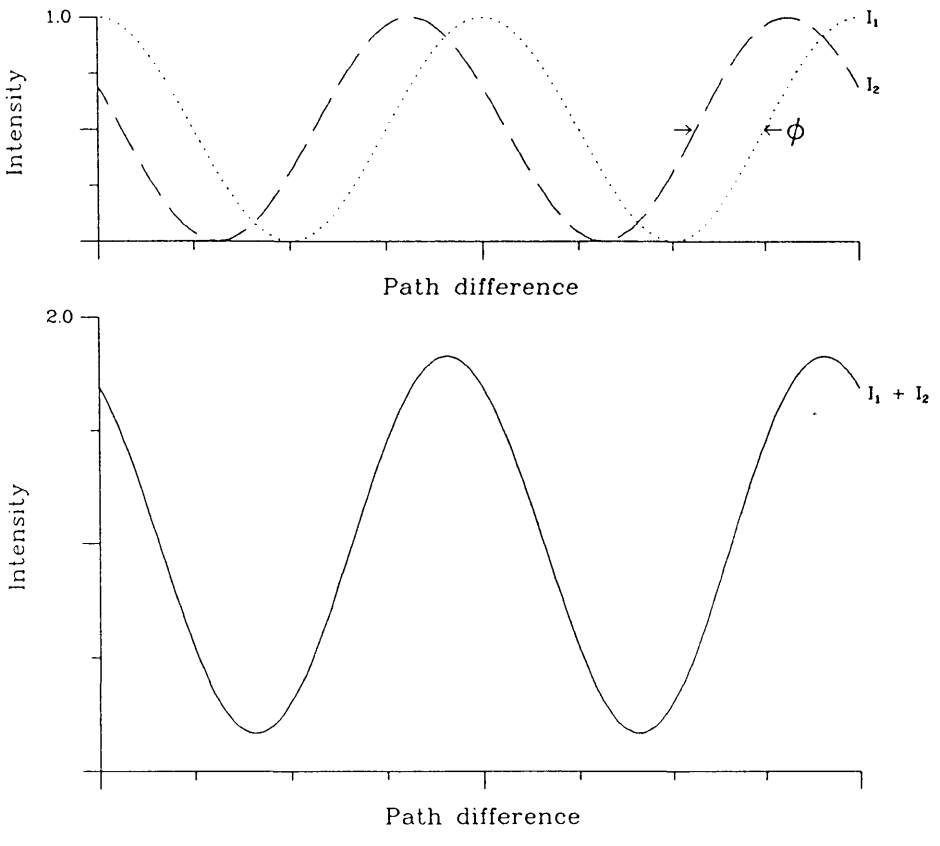


Figure 3.4: Effect of errors in the phase of the Michelson's $\cos^2$ fringes.

The Michelson

Scanning the Michelson gives $\cos^2$ fringes, (figures 3.4a and b). The sum of the squares of two cosines is

$$\cos^2 A + \cos^2 B = 1 + \cos(A+B)\cos(A-B). \tag{3.81}$$

As a simplification, consider two lines, $\lambda_1 \approx \lambda_2$, of equal intensity, n counts per second, which, at a certain path length have fringes at nearly the same frequency, (λ_1's phase been given by $\psi = 2\pi\Delta/\lambda_1$), (figure 3.4c), separated by phase, ϕ,

$$n[\cos^2\psi + \cos^2(\psi+\phi)] = n[1 + \cos(2\psi+\phi)\cos\phi]. \tag{3.82}$$

$\cos\phi$ is a 'constant' that varies from 1 for when the fringes are in phase to -1 when they are 180° out of phase.

The two output beams from the Michelson, C and D, are the complements of each other. At the cross-over points, $C = D = n/2$, and for 100% deep $\cos^2$ fringes, the slopes are $\mp n$. i.e.

$$\frac{\mathrm{d}I}{\mathrm{d}\psi} = \mp n. \tag{3.83}$$

For very small changes in wavelength, $\mathrm{d}I/\mathrm{d}\psi$ is approximately constant, i.e.

$$C' = C + n\,\delta\psi \quad ; \quad D' = D - n\,\delta\psi. \tag{3.84}$$

At the cross-over point $C \approx D \approx n/2$,

$$r = \frac{C'-D'}{C+D} = \frac{2n\,\delta\psi}{n} = 2\,\delta\psi. \tag{3.85}$$

If a second line is added, the slope is changed to, (by differentiating equation 3.82),

$$\frac{\mathrm{d}I}{\mathrm{d}\psi} = -n\sin(2\lambda+\phi)\cos\phi. \tag{3.86}$$

For the cross-over points, $C'/n = D'/n = 1/2$, or $\cos(2\psi+\phi) = 0$; i.e.

$$\frac{\mathrm{d}I}{\mathrm{d}\psi} = -n\cos\phi. \tag{3.87}$$

Similarly to equations 3.84 and 3.85 this gives

$$r_{(2\text{ lines})} = 2\cos\phi\,\delta\psi. \tag{3.88}$$

As in equation 3.15, the noise is given by

$$\sigma_r^2 = \frac{\frac{1}{2}n^3 + \frac{1}{2}n^3}{n^4} \tag{3.89}$$

or

$$\sigma_r = \frac{1}{\sqrt{n}} \quad \text{or} \quad \sigma_{r_{(2\ \text{lines})}} = \frac{1}{\sqrt{2n}}. \tag{3.90}$$

(3.91)

Therefore equating the change in the ratio with the noise, (in the ratio), gives

$$2\,\delta\psi = \frac{1}{\sqrt{n}} \quad ; \quad 2\cos\phi\,\delta\psi_{(2\ \text{lines})} = \frac{1}{\sqrt{2n}} \tag{3.92}$$

or

$$\delta\psi = \frac{1}{2\sqrt{n}} \quad ; \quad \delta\psi_{(2\ \text{lines})} = \frac{1}{2\cos\phi\sqrt{2n}}. \tag{3.93}$$

i.e., for there to be an improvement in signal from adding two lines,

$$\delta\psi_{(2\ \text{lines})} < \delta\psi, \tag{3.94}$$

$$\frac{1}{2\cos\phi\sqrt{2n}} < \frac{1}{2\sqrt{n}}, \tag{3.95}$$

$$\cos\phi > \frac{1}{\sqrt{2}} \tag{3.96}$$

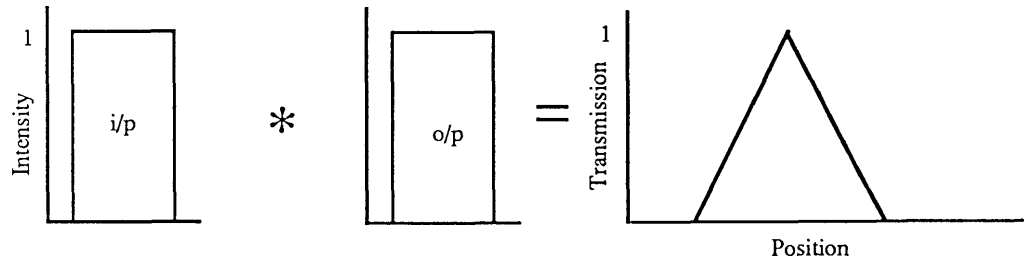
i.e., the maximum phase error before there is any degradation in signal is 45°. Obviously for a worthwhile improvement in signal the phases need to be more accurate than above.

$$\text{Fractional Improvement Achieved} = \frac{\cos\phi - 1/\sqrt{2}}{1 - 1/\sqrt{2}}. \tag{3.97}$$

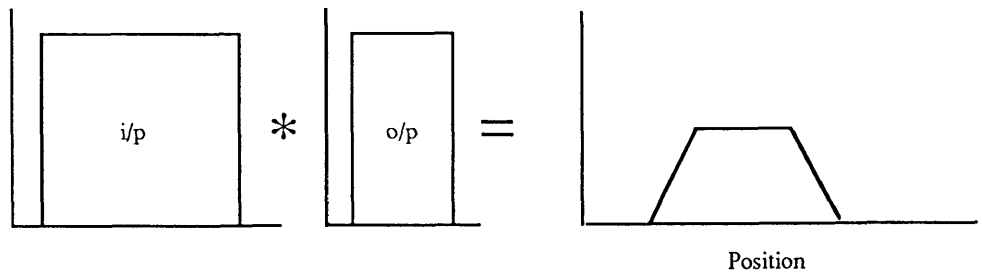
However, fortunately, from equation 3.97, an error of $\approx 4.4°$ gives nearly 99% of the maximum gain.

3.3.4 Pre-disperser

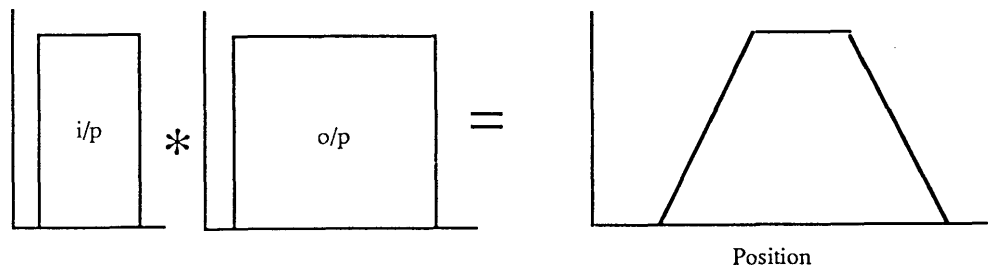
Normally for maximum resolution combined with efficient use of the light, the exit and the image of the entrance slits of a spectrometer are of equal size, so giving the filter profile as in figure 3.5a. For the present problem, the spectrometer can be considered to be acting as a pre-filter and its resolution is less important. However, to reduce sensitivity to spectrometer (filter) drift it is necessary to have a broader flat topped filter profile. Widening the input aperture achieves this, but leads to loss of light (figure 3.5b). However, increasing the size of the output slit/fibre gives the required result (figure 3.5c). To make efficient use of the optical fibres without using individual subsidiary optics for each output fibre, at least the output optics, (from the spectrometer, i.e. the *input* optics to the output fibres), need to be around f3. Of course the spectrum will have to be of a suitable physical size to allow for the positioning of the fibres.



a) Equi-sized input and outputs



b) Input slit twice the width of the output slit.



c) Output slit twice the width of the input slit.

Figure 3.5: Convolution of input aperture with output aperture for differing size slits. (Even though the intention is to use fibres this is drawn for straight slits.).

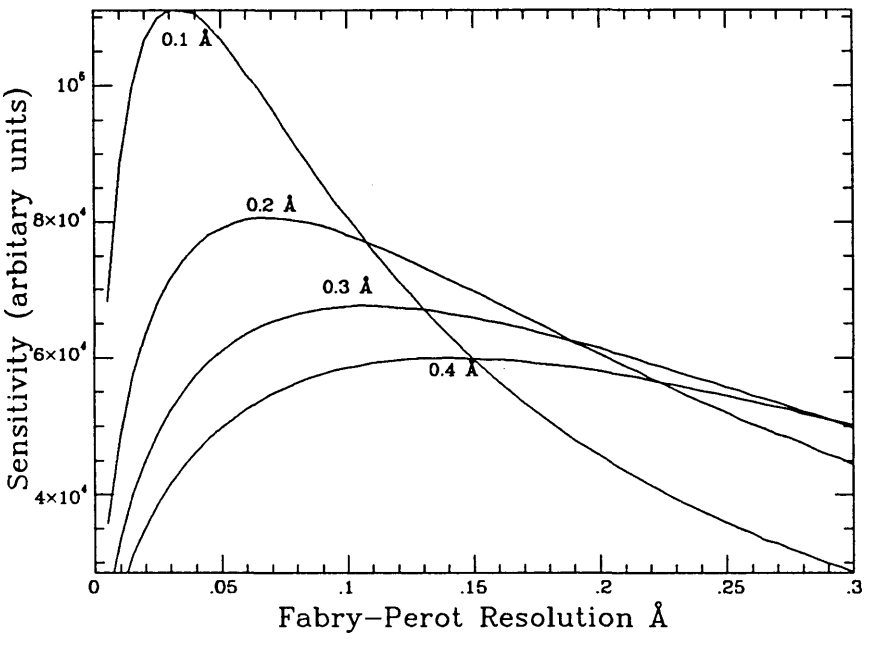


Figure 3.6: Sensitivity v. resolution for differing line profiles.

3.4 Detailed Fabry-Perot Design Study

As can be seen from above the Fabry-Perot is very strongly affected by the lowering of the resolution for off-axis angles. As shown by equation 3.43, for a given wavelength and input aperture, the maximum *useable* off-axis angle depends on the resolution of the etalon, but is independent of the gap. For the Fabry-Perot to be suitable for all wavelengths, the maximum useable angle must be greater than the distance to the first off-axis order. This can be achieved by adjusting the inter-order distance. However, this then restricts the size of the filter profile useable, which can introduce sensitivity to drifts. What are the optimum resolutions, and, hence, the optimum filter profiles for differing stellar lines?

3.4.1 Optimum Fabry-Perot Resolution

Different types of stars have different line widths. These range from less than 0.1 Å for the cooler stars to greater than 1 Å for the hottest. Figure 3.6 is a plot of the sensitivity versus the Fabry-Perot resolution for a number of different linewidths. A Gaussian profile was used for the stellar absorption lines, and for the filter profile, the 'ideal' produced by the echelle, as discussed in chapter 4, was used. Other runs

had demonstrated that there were variations in optimum resolution for differing filter profiles, but that this was small. The change in resolution of the Fabry-Perot was produced by varying the finesse. The first thing to be noticed is the resolution of the etalons needed, approximately 40% of the width of the (Gaussian) line profile. This suggests that for maximum sensitivity, extremely high finesses are needed for line widths similar to those in the Sun. Another thing of note is the increase in sensitivity with the narrower lines.

3.4.2 Filter Width

According to Griffin and Griffin [63] accuracies of less than 1 $\mathrm{km\,s^{-1}}$ have been obtained photographically, i.e. using long exposures. (Presumably without using telluric lines which they, (Griffin and Griffin), suggested can be used for obtaining accuracies of 10 $\mathrm{m\,s^{-1}}$.) For 5000 Å this is equivalent to an accuracy of $\approx$ 0.02 Å. From the above, it can be expected that a properly designed spectrometer can be made stable, (or at least servo-controlled), to better than 0.02 Å. As a more conservative estimate, drifts of around 0.1 Å might be expected.[3]

Figure 3.7 shows the change in radial velocity versus filter drift for a fixed filter profile with different combinations of lines and etalon gaps. The Fabry-Perot instrumental profiles used are the optimum for the line width, (found using the same program as was used for generating figure 3.6). The filter profile used is that theoretically produced by the echelle pre-disperser described in chapter 4. Not unexpectedly, the errors decrease with decreasing line, (and Fabry-Perot instrumental), width. With the smallest line width shown, 0.1 Å there is an error of less than 5 $\mathrm{m\,s^{-1}}$ for the 0.1 Å expected drifts. Unfortunately, the largest line width investigated has produced an error of about 270 $\mathrm{m\,s^{-1}}$, which is comparable to the 'error' produced by the Earths heliocentric velocity ($\approx \pm 290$ $\mathrm{m\,s^{-1}}$ for London). As both of these are expected to be of a much greater period than any '5-minute' type oscillations, hopefully they should not affect the data too much.

Figure 3.8 illustrates the importance of very good images from the echelle and uniform transmission across the fibre ends. The filter profile has now been replaced by a Gaussian filter profile of the same full width half maximum (FWHM). As can be seen, there has been a large increase in sensitivity to drifts, with the 0.4 Å line more than

[3]For the present spectrometer, 0.1 Å $\approx$ 1.5 thou.

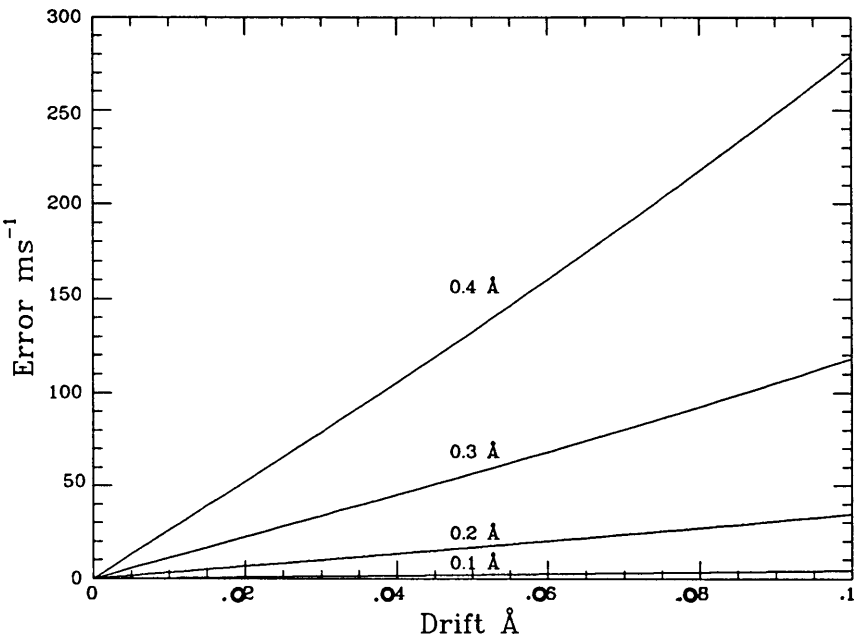


Figure 3.7: Error in radial velocity v. filter drift for a fixed filter profile. All the lines are 70% deep and have a Gaussian line profile. The filter was produced by convolving a 600 μm circle with a 260 x 370 μm ellipse with a dispersion of 2.8 mm/Å to represent the output fibre and the image of the input aperture from the echelle discussed in chapter 4.

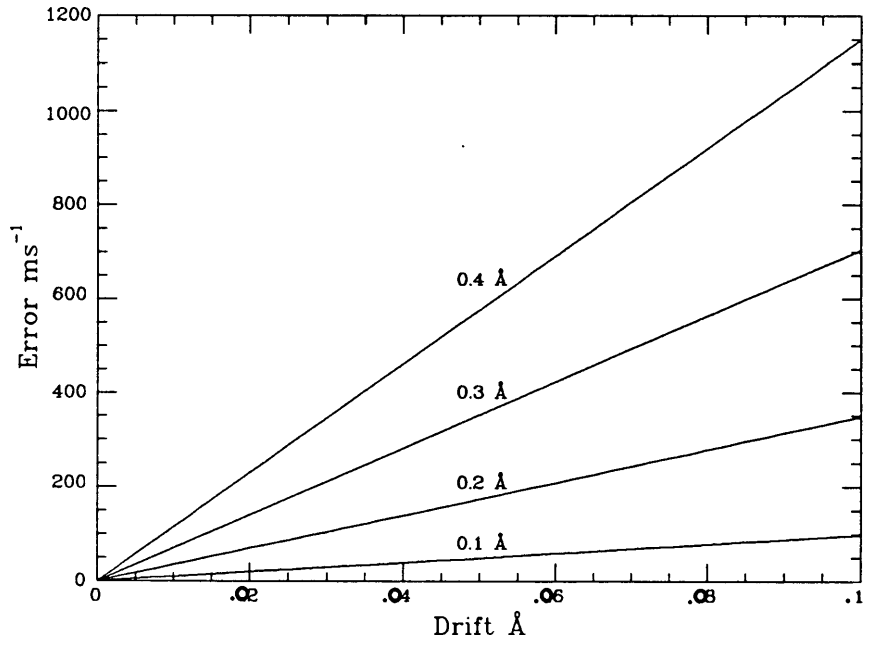


Figure 3.8: Error in radial velocity v. filter drift for a Gaussian filter profile with the same full width half maximum as the 'ideal' filter profile from the echelle.

quadrupling in sensitivity and the narrower lines seeing even larger relative increases.

From the above, it appears that the pre-disperser, for a Fabry-Perot, needs to have a FWHM of about 8 times the stellar line width, for poor image quality, or for very good image quality, a 'flat top' of about 2.5 times the line width.

Chapter 4

The Pre-Disperser

The instrument consists of two main parts, the pre-disperser and the interferometer, (plus of course a telescope). However as the instrument is connected to the telescope, and the interferometer is fed from the pre-disperser, via optical fibres it is proposed to first discuss the properties of these, along with some of their uses.

4.1 Optical Fibres

Step index fibres have proved to be the most useful optical fibres in astronomy. They consist of a high refractive index core, plus a lower refractive index cladding, all surrounded by some kind of protective sheath. They rely on total internal reflection at the core/cladding interface. There are two main types: all silica, (A.S.), which have a core and cladding made of differently doped fused silica to give differing refractive indices; and plastic coated silica, (P.C.S.), which have a silica core and a cladding made out of plastic. Whilst the P.C.S. fibres have a large numerical aperture, 0.4 (f1.2), compared to 0.2, (f2.5), for A.S., the A.S. fibres seem to last better and show less focal ratio degradation, (spreading of the beam caused by scattering inside the fibres). Normally they are designed for transmission in the red. However, it is possible to obtain fibres with a core having a higher water molecule content, (hence known as wet), which show an improved blue transmission. P.C.S. fibres are available in sizes from 50 μm to 1500 μm core diameter, with A.S. fibres being readily available up to 200 μm, but 400 μm core diameter A.S. fibres have been produced [88,87].

The two major, (often simultaneous), uses of optical fibres in astronomy are as image scramblers and light guides. As image scramblers optical fibres have unique properties.

Unlike most optical systems where the output ray can be predicted from the input ray, with optical fibres, the position and azimuthal angle with respect to the exit face of the emergent ray are arbitrary, only the input angle to the fibre axis, θ_i, being approximately conserved. This means that for high accuracy spectroscopy, for example radial velocity measurements, errors due to the stellar image moving over the input slit, because either of seeing or inaccurate guiding, are much reduced [89].

The simplest use of optical fibres as light pipes is for them to act as a coudé focus replacement. This allows all the advantages of working with off-telescope instrumentation, (ease of temperature control, simplicity of installation, reduced requirements for mechanical strength etc.), to be had very simply and cheaply. It has the added advantage that it is possible to change between two instruments in a matter of minutes, if the observing programme or weather requires it.

As well as feeding a spectrometer with a single fibre, multiple object spectrometers have been built. In these multiple fibres are used, each fixed in the image-plane of the telescope at the position of an object, (usually a galaxy), for which a spectrum is required. Obviously if, (say), twenty objects are viewed simultaneously, ignoring possible extra losses in the system, the telescope is being used twenty times more efficiently [90,91].

Another use for fibres as light pipes is to make image slicers out of bundles of optical fibres, where the bundle of fibres turns a two dimensional image into a one dimensional line suitable for feeding into a spectrometer's input slit. Both the above techniques have been tried out on the Anglo-Australian telescope [90,93].

One of the major problems found when working with optical fibres is focal ratio degradation. This is far worse for low numerical aperture beams, than for beams with numerical apertures near the fibre's maximum, (see figure 4.1). Hence, optical fibres are usually used at or near their maximum numerical aperture. Also, as well as spreading outwards, the beam can spread inwards, so filling any 'shadow' caused by the telescope's secondary, which, if as in a lot of spectrometers, the instrument uses optics which have central obstructions, leads to light loss.

4.2 Interfacing the Telescope to the Input Optical Fibre

The largest telescope that the instrument might possibly be used with is the 4.2m William Herschel. From the previous discussion it is better to feed the fibre close to

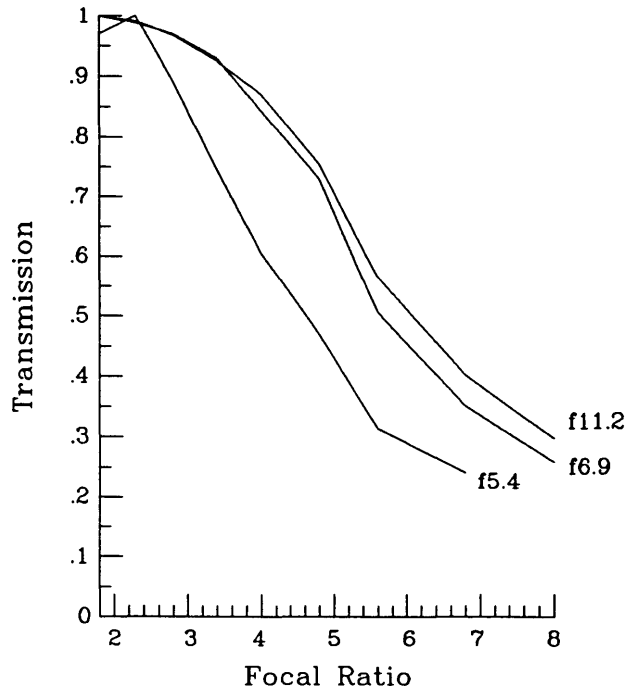


Figure 4.1: Focal ratio degradation in a 200 μm A.S. fibre.

the fibre's maximum numerical aperture. For all silica fibres, f3 is probably a good compromise, which for 3″ seeing, (a bad night), would give a seeing disc of about 180 μm, hence a 200 μm fibre could be used. As most telescopes are usually used at high focal ratio focuses like the Cassegrain, it is necessary to convert from, for example, f11 at the Napier focus of the William Herschel or f15 at the Cassegrain focus of the Isaac Newton to f3 for the fibre.

The simplest way of doing this is shown in figure 4.2a, where a lens is placed after the focus of the telescope. The disadvantage of this method for accurate radial velocity measurements is that if there are any changes in the image size or position from the telescope, caused by alterations in seeing, guiding etc., this affects the input fno. to the optical fibre. A better way, but needing two lenses, is shown in figure 4.2b, where the converging lens is placed before the focus of the telescope. The diverging lens acts as a field lens to "throw the pupil to infinity", that is to straighten the chief rays. With this system, alterations in the seeing affect the image size on the fibre (which is relatively unimportant), not the fno., (which could alter the output from the fibre).

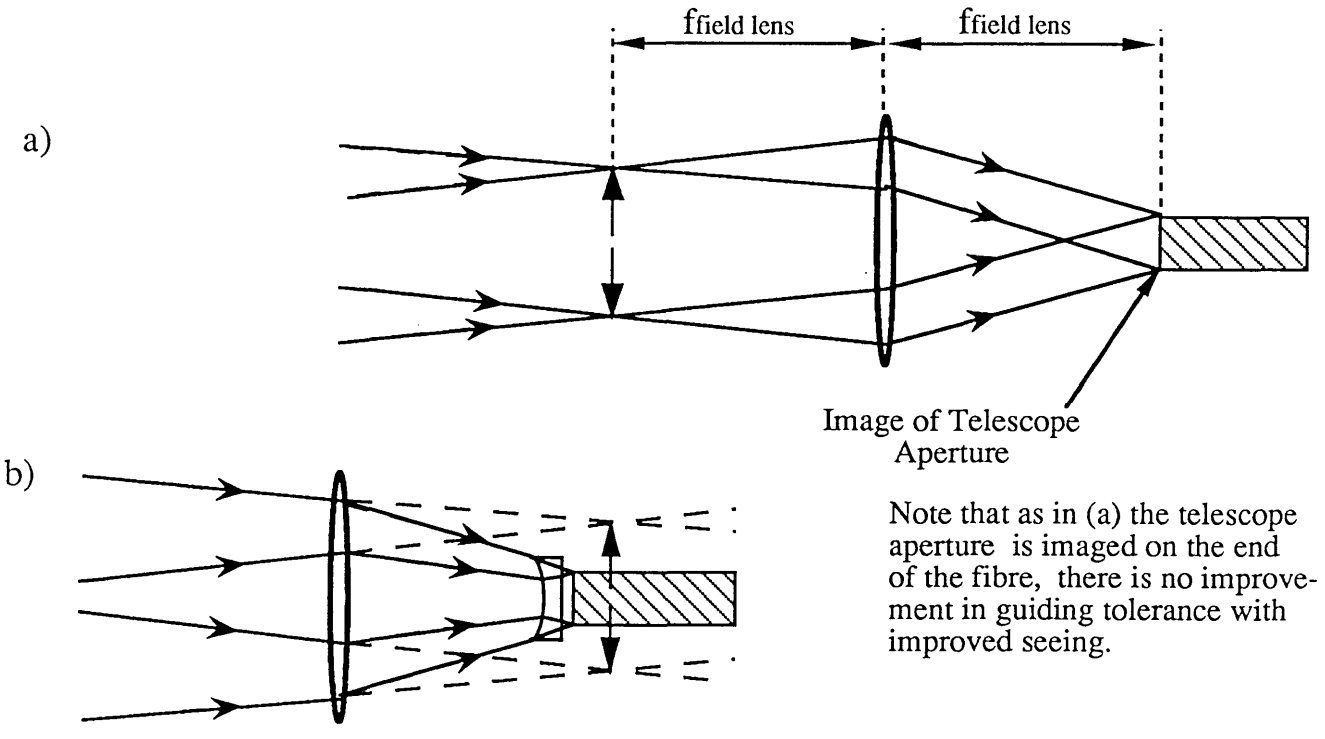


Figure 4.2: Interfacing the telescope to the optical fibre.

4.3 The Echelle

Choice of Dispersion

The expected typical full width half maximum for absorption lines in the stars of interest ranged from about 0.1 Å to 0.3 Å. So for a reasonable filter profile, a 'flat top' of around about .75 Å was required. The input beam into the pre-disperser was close to the maximum numerical aperture possible for use in fibres; so, a faster beam could not be used. Therefore, to produce a 'flat top', larger output fibres were necessary. The sizes which were available had core diameters of 400 μm and 600 μm, which would need a dispersion of 3.75 Å mm^{-1} and 1.9 Å mm^{-1} respectively, to give a flat top of 1 Å to the filter profile, if the output fno. was the same as the input fno, i.e. a 200 μm image size. Whilst high resolution was not necessary, high luminosity and high angular dispersion with a fast output beam was. Also, it would be useful if the grating could be blazed, so that more than one fibre per line would not be necessary, as most of the light from one wavelength would be in one order. For these reasons an echelle grating was the best choice.

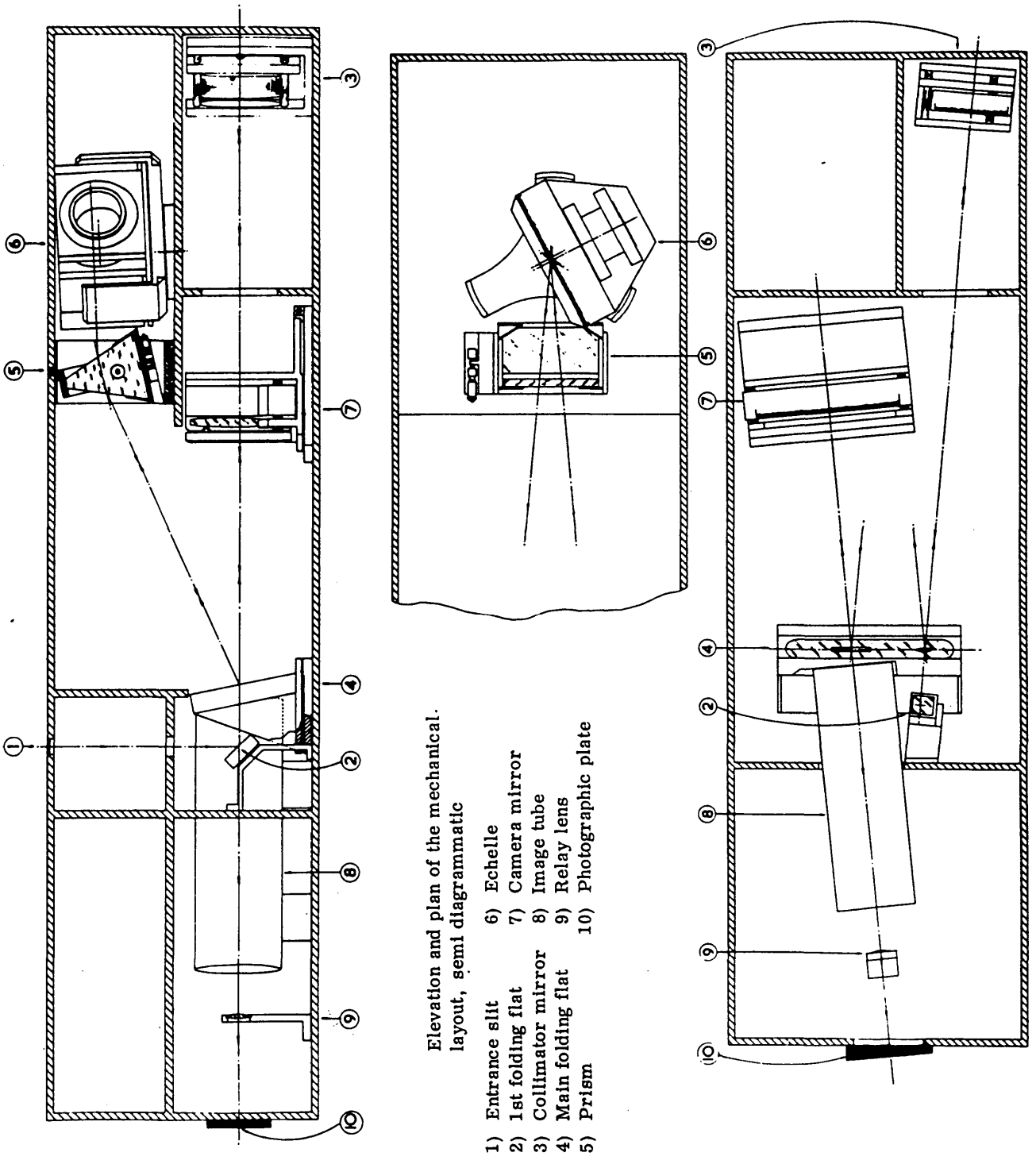


Figure 4.3: The Learner echelle in its original condition (from [92]). As used, the image tube was replaced by the output fibre holder and the "1st folding flat" was removed, so allowing the light straight through from the input fibre.

Fortunately there was an echelle spectrometer available from R.G.O., figure 4.3. This had originally been designed at Imperial College by Learner [92] as a prototype for an instrument to be used at the Anglo-Australian Telescope. The grating had a blaze angle of 63°26′ with 79 lines/mm. The collimator was f15 and the camera mirror f3.5 by f5. The average dispersion was 2.8 Å mm^{-1}, which gave a flat top of 0.95 Å using a 1.11 mm input aperture, (the equivalent to a 200 μm fibre converted from f2.7 to f15), with 600 μm output fibres, which was about what was necessary. Hence it was decided to take advantage of this.

4.3.1 Interfacing the Input Optical Fibre to the Echelle

Input Optics

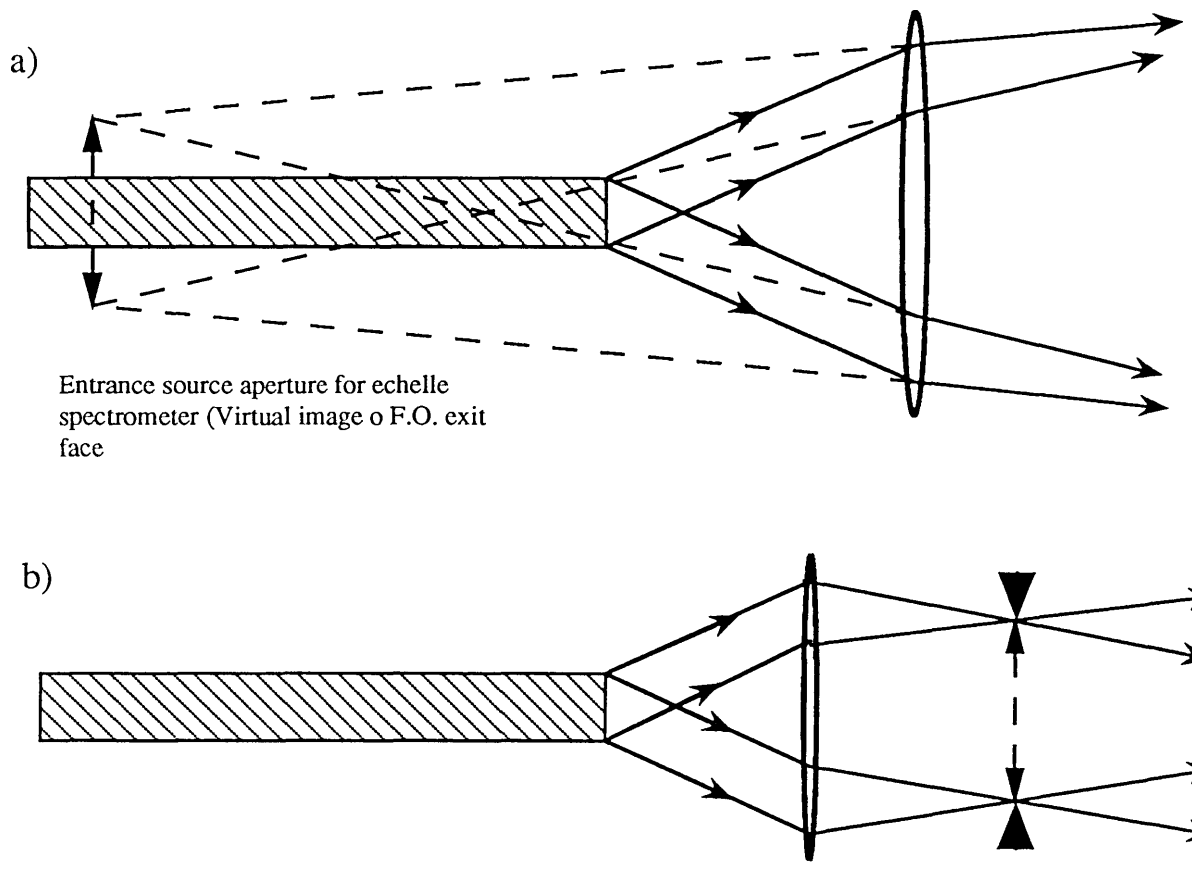


Figure 4.4: Altering the output focal ratio from the fibre.

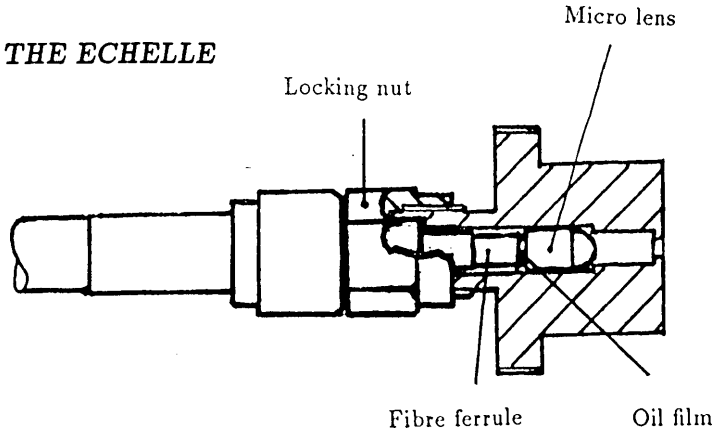


Figure 4.5: Input optics to the echelle spectrometer.

The collimator was a f15 mirror, so it was necessary to convert the $\approx$ f2.7 beam out of the fibre into a f15 beam. Two possible ways of doing this are shown in figures 4.4a and 4.4b. The first method is to use a lens as a magnifying glass, (figure 4.4a), the second is to put the fibre at the focus of a short focal length lens. The second method converts the fno. out of the fibre into the diameter of the input aperture, (figure 4.4b). This has the advantage that it ensures the collimator is always filled, as the beam produced is always at the correct fno., whatever the beam from the fibre does, (changes in the fno. out of the fibre affect the input aperture size), where as the first method always keeps the same size input aperture, but allows the fno. to vary. The first method also has the advantage that if the spectrometer design relies on there being a central 'hole' in the beam, it maintains any of the shadow of the secondary remaining after passing through the input optical fibre. It was believed at the time that even illumination of the collimator was the most important property required, and consequently, the second method was used, (figure 4.5). Now however, the problems of variation in the filter profile caused by changes in the diameter of the input aperture are considered to be more important. (Though these problems should be small if the fibre was fed correctly at a constant fno.)

Correcting for Inherent Stellar Radial Velocity

The majority of stars have an inherent radial velocity caused by their Heliocentric radial velocity and the motion of the Earth. For minimum sensitivity to 'filter' drifts, it is necessary to have the absorption line centralized in the 'filter'; therefore, the filter profile must be able to be moved to correct for Doppler shifts. For a single wavelength this can be done in several ways: by moving the input aperture, by moving the output aperture or by tilting the grating. With multiple wavelengths, however, there are problems with

changes in dispersion across the spectrum. Walraven [93] demonstrated that this can be overcome in a Litrow mounting by shifting both the input and output apertures in opposite directions.

From

$$m\lambda = d(\sin i + \sin r) \tag{4.1}$$

$$\frac{\mathrm{d}\lambda}{\lambda} = \frac{\cos i.\mathrm{d}i + \cos r.\mathrm{d}r}{\sin i + \sin r} \tag{4.2}$$

For a proportional shift in the entrance and output apertures, i.e.

$$\mathrm{d}r = \alpha\,\mathrm{d}i \tag{4.3}$$

equation 4.2 becomes,

$$\frac{\mathrm{d}\lambda}{\lambda} = A\,\mathrm{d}i \tag{4.4}$$

where

$$A = \frac{\cos i + \alpha \cos r}{\sin i + \sin r} \tag{4.5}$$

Therefore, as $\delta\lambda/\lambda$ is a constant, (for a given δv), across the entire spectrum, A must be independent, to first order, of r. i.e.

$$\frac{\mathrm{d}A}{\mathrm{d}r} = 0 \tag{4.6}$$

Pure autocollimation in the blaze angle, β, i.e. $i = r = \beta$, gives

$$\alpha = -[1 + 2\tan^2\beta]^{-1} \tag{4.7}$$

This means that for a $63\frac{1}{2}^\circ$ grating, the input aperture has to be moved nine times as far as the output aperture. There are still second order terms, but for smallish angles (≈ 0.1 radians) these are negligible.

However to implement this is difficult. It was decided, for simplicity, to only move the input aperture. The largest changes in radial velocity needed are about ± 50 km s^{-1} [82, pages 235–241]. With the grating being a cross dispersed echelle each order is quite short, being only about 140 Å long. For the 45th order, the central wavelength theoretically is 5016 Å and a change in velocity of 50 km s^{-1} produces a doppler shift of 0.836 Å. From equation 4.1,

$$\sin i = \frac{m\lambda}{d} - \sin r \tag{4.8}$$

giving a change in incident angle, δi, of 0.067°. The wavelength at one end of the output field in the 45th order is about 5086 Å, for which $r = 61.36^\circ$, which undergoes a doppler

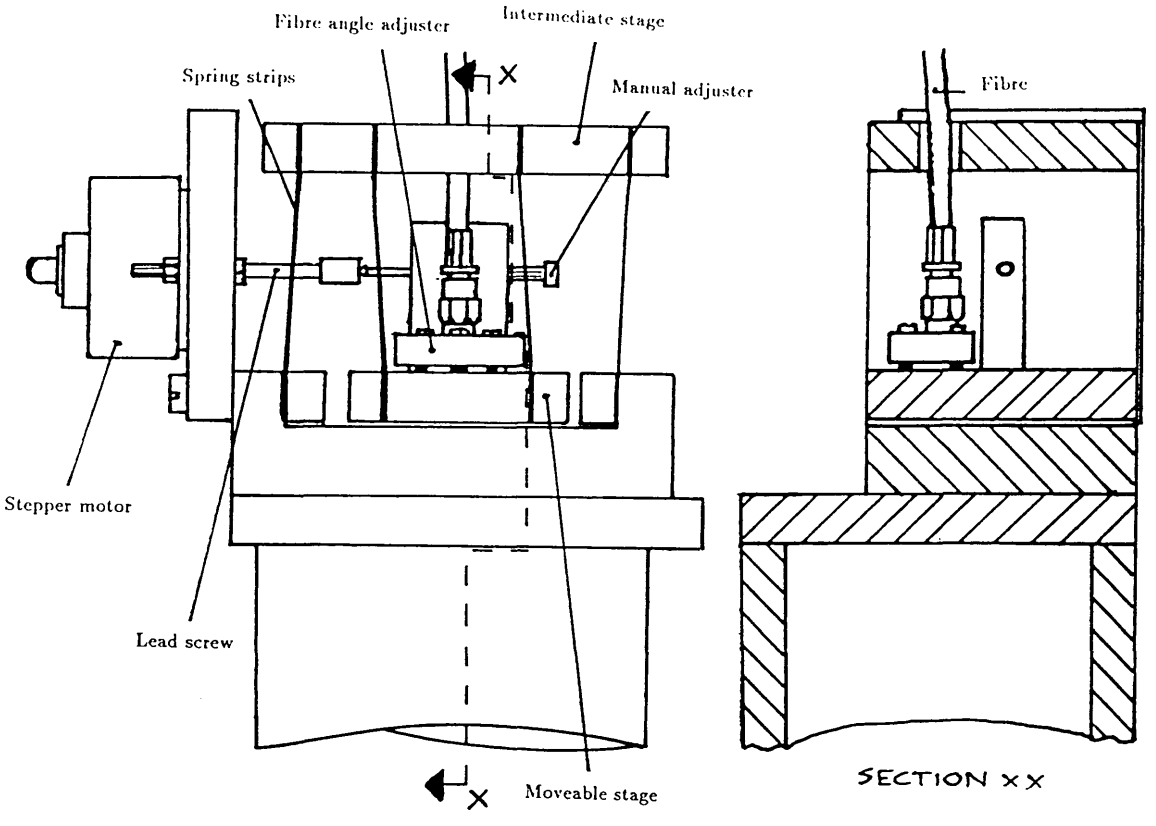


Figure 4.6: Spring strips design for compensating for changes in radial velocity.

shift of 0.848 Å for a 50 km s^{-1} change in velocity. However for $r = 61.36°$, moving the input aperture 0.067° means that the centre of the fibre is equivalent to $\lambda = 5087.2$ Å, a difference of 0.36 Å. This means that the line is 127 μm off the centre of the fibre, or slightly under a quarter of the width of the fibre; therefore, the majority of the line should probably still be within the 1 Å flat top of the filter profile. Although this is possibly excessive, it is for the extreme case; that is, a line on the edge of the output field and for a star with the maximum doppler shift. For the vast majority of stars and/or lines the discrepancy will be much less than this. Hence moving only the input aperture is probably satisfactory.

For a 1.5 m collimator, a 0.067° movement in the input aperture is equivalent to 1.75 mm. $\pm$50 km s^{-1} is about 4 mm of movement. One way of producing this is to use spring strips [94,95]. For short distances these can give a very accurate linear movement. The design which was used is shown in figure 4.6. The position was controlled by a linear actuator, (a commercially produced combination of a stepper motor plus screw thread).

As there was no need for the spectrometer to sit up against the bottom of the mirror

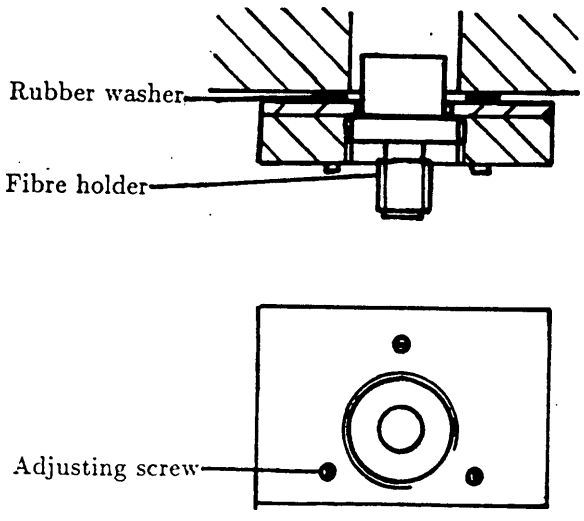


Figure 4.7: Input fibre angle adjuster.

cell, the first folding flat, (in the original design), could be dispensed with. An extra tube, however, was required to mount the input aperture in the correct position.

Problems were found with the alignment of the fibre to the collimator mirror, so the fibre was mounted using an adjustable mounting consisting of three 'rubber springs', rubber washers compressed by a brass plate and adjusted by tightening or loosening three screws, (figure 4.7).

4.3.2 The Output Mask from the Echelle

It was decided to use the plate holder which came with the spectrometer. To enable the mounting plate for the fibres to be reproducibly positioned, kinematic mounting was used. There were already three balls to keep the photographic plates in the correct plane of focus for the spectrometer. Three more balls, plus opposing springs, were added to keep the plate in the correct vertical and horizontal, (at right angles to the optic axis), positions and at the correct angle (figure 4.8). A new back was made. It had a large aperture, to allow the fibres to pass through. Also, it was fitted with three locking screws, (over the three balls), which were used to hold the plate in position.

Selecting the Stellar Lines

The positions of the spectral lines were found by taking a photograph of the solar spectrum on a photographic plate made by Ilford, (with similar properties to FP 4 35 mm film). Immediately after the solar spectrum had been photographed, a photograph was taken of a mercury and a neon discharge lamp spectrum on another plate, to provide a

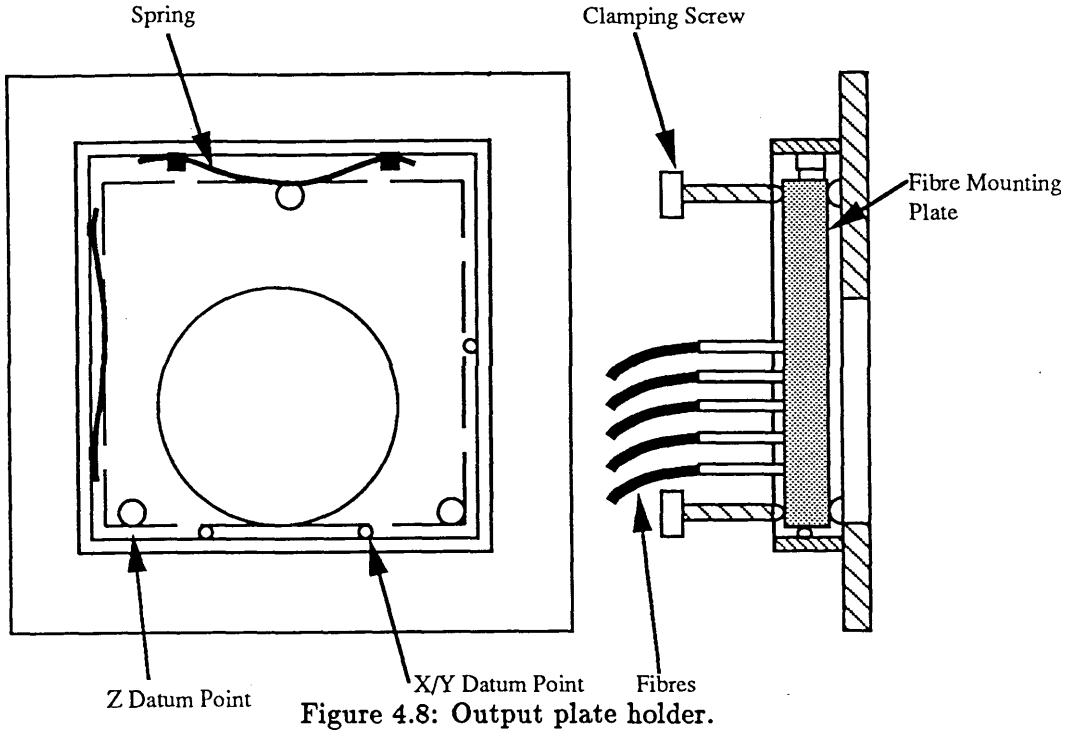


Figure 4.8: Output plate holder.

reference for realignment. On the solar spectrum, the positions of the X and Y kinematic mounting points were marked to act as datum points.

By working through a solar atlas [96] and catalogue [97], suitable absorption lines were chosen and marked on an enlargement of the spectrum. As the height in the sun at which different species are formed varies, to remove any problems of differing radial velocities with height, lines from the same species were used. Because of the number of lines available, it was decided to use all iron I lines. They had to be from $\approx$ 4500 Å to 5500 Å to match the available Fabry-Perot's coatings; far enough away from each other to allow the fibres to be positioned, (in two dimensions, as the orders were close together); no large close by lines in the spectrum, which might affect their line profiles; and they had to be as wide as possible, so that they would match the resolution of the Fabry-Perot, which was about 0.37 Å. (Because of the sun's low rotation rate most solar lines have a width of around 0.1 Å as opposed to 0.2 to 0.3 Å in some of the stars we were interested in.) An attempt was made to choose lines which would be suitable for the restricted range of the available Fabry-Perot, (see chapter 5), by the use of a computer program which chose the gap for which the most lines could be used. The position of the lines were measured by using a microscope which was fitted to a numerically controlled jig-borer. The photographic plate was attached to the jig-borer with double sided Sellotape, the positions of three datum points, (based on the positions of the three new kinematic mounting points), recorded, and by finding large features in the spectrum

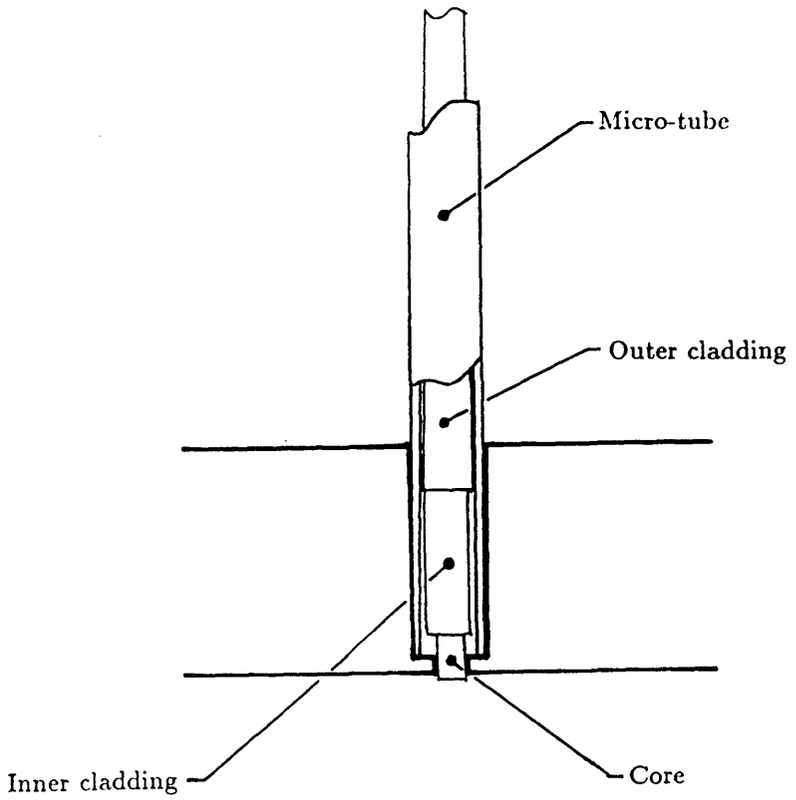


Figure 4.9: Output fibre mounting technique.

on both the plate and enlargement, the lines identified and their positions measured. It was then a case of doing a simple co-ordinate transform to find the positions of the lines with respect to the datum points. The fibre holes were then drilled on the same jig-borer as had been used to measure their positions.

Initially an 800 μm hole was drilled and counter bored to 1.65 mm. The fibres were held by using lengths of stainless steel tubing glued into the counter-bored holes. The fibres were attached to this using lengths of heat shrink. This was done so that the fibres could be easily dismantled without damaging them. Originally it was intended to locate the fibres in a 800 μm hole using the optical cladding of the fibres. However, the optical cladding is very soft and easily damaged, so a new plate was made with holes drilled to locate the 600 μm core, (figure 4.9). Initially nine fibres were used.

Chapter 5

The Interferometer

There have been two types of interferometer which have been developed at Imperial College for measuring the radial velocity of stars, based around Michelson [75,77] and Fabry-Perot [78,79] interferometers. (See also section 2.3.3.) Both of these have been tested with the pre-disperser. The Michelson was at a higher level of development than the Fabry-Perot, and using it with the pre-disperser needed very little work. However, the Fabry-Perot had only been used to measure large radial velocities, ($km\,s^{-1}$) [78], and before it could be used on the Sun or Solar type stars it needed a lot of development work.

5.1 The Michelson Interferometer

As the Michelson was field-widened, there should have been only a very small change in phase across the input aperture. So that the input wavelength could be changed by altering the input angle, the intention was to adjust the position of one of the cube corners on the Michelson to give a greater than 360° phase change across the entrance aperture, (in one direction), and then cement it in place, using UV setting cement. On inspection, however, it was found that there was already more than 360° phase change due to misalignment or, possibly, optical defects.

The total path length in the interferometer was equivalent to 5.5 mm of air. As can be seen from figure 5.1a, simply putting a fibre off-axis leads to vignetting. By putting a negative lens just in front of the fibres as in figure 5.1b, the beams from the off-axis fibres can be made to cross in the middle of the interferometer. This also has the advantage that as the beam splitter is nearly at the middle of the interferometer,

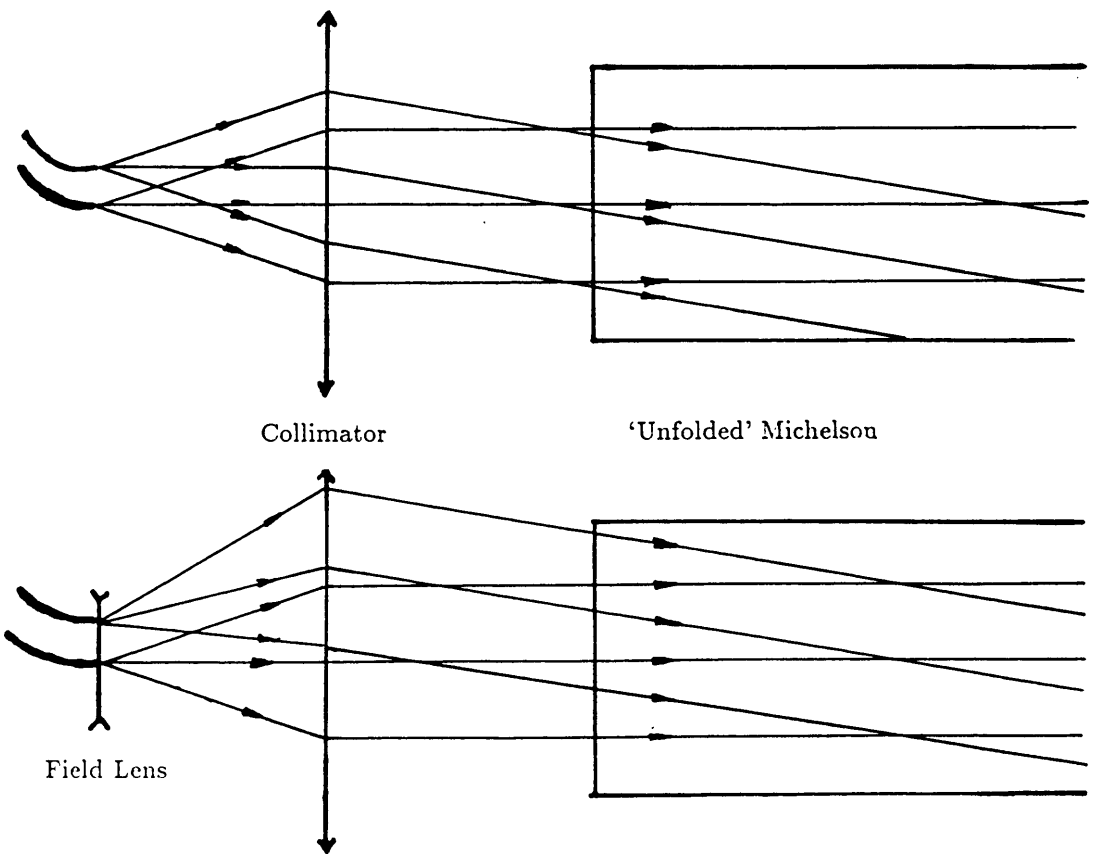


Figure 5.1: Use of a field lens in the Michelson interferometer to stop vignetting. For simplicity the Michelson has been drawn 'unfolded.'

all the beams use more or less the same part of the beam splitter.

The size of field produced by moving the cube corner was 20 mm. As can be seen from equation 3.97, for 99% of the maximum possible improvement, an error of about a $\frac{1}{40}$ of a fringe is tolerable. For this, possibly over-rigorous criterion, the positioning tolerance is $\lesssim \pm 0.5$ mm. If a little bit more leeway were to be allowed, the fibres needed positioning only approximately. This was done by drilling an array of holes in a plate, which was then placed at the input aperture of the Michelson. It was decided to test the principle with nine fibres. The fibres from the pre-disperser were individually scanned to find the one that gave the best fringes, (a combination of depth and brightness). This was placed in the central hole. The Michelson was scanned, and the best cross-over point, (the position where the phase in the signal and reference fringes most nearly go through zero simultaneously), noted. The fibre was then removed, another fibre placed in the central position, and again scanned. By comparing the fringes from this fibre, at the cross-over position of the reference fringes, with that of the first fibre, it was possible to calculate where in the field it should go. The fibre being tested was then removed from the centre, and inserted in the indicated hole, and the 'master' fibre replaced in the central hole. The Michelson was again scanned, and the depth of the fringes compared with those from the test fibre. If the results were not satisfactory, the test fibre was repositioned in adjacent holes until the fringe depths were comparable to those originally obtained from the test fibre. The process was then repeated for the remaining seven fibres.

5.2 The Fabry-Perot

For the Fabry-Perot, apart from the etalon and the CS100 control system, virtually an entirely new instrument had to be designed, including a new mounting, software and a lot of the electronics. First of all an ideal etalon for the present pre-disperser will be defined and then a description given of how the etalon that was available was used.

5.2.1 The Ideal Etalon for the Current Pre-Disperser

The maximum width of the filter profile from the pre-disperser, hence the minimum inter-order distance, is about 2.5 Å. To allow for some margin of error it would probably be better to have an inter-order distance of twice this, i.e. 5 Å. Equation 3.47 then gives an order of 1000 with a wavelength of 5000 Å on axis, leading to a gap of 250 μm, (from

Table 5.1: Specifications of an 'ideal' and the available etalons (at 5000 Å).

	Ideal	Available
Diameter	≈300 mm	85 mm[a]
Gap	250 μm	92 μm
Finesse	47	33[b]
Inter-order distance	5 Å	13.6 Å
Resolution	0.15 Å	0.37 Å

[a]70mm useable diameter
[b]Over 70 mm

equation 3.48). Hotter stars of interest have line widths of about a 0.25 to 0.4 Å, so a suitable resolution would be about 0.15 Å. This means that the etalon would need a finesse of about 33. For a gap of 250 μm, the first off-axis angle at which 5000 Å reappears is 2.56°, (from equation 3.53). The maximum angular size of fibre which can be used is, (from equation 3.54), 0.038° , which, using 600 μm fibres, is equivalent to a collimator of 893 mm. This gives the minimum size of etalon required, (equation 3.57), using an output beam of f3, to be 297 mm. The above etalon would have a resolution of 0.15 Å in the centre, becoming 0.21 Å at the edge.

If one were produced to this specification it would be extremely expensive. There are several options for making the etalon of more manageable dimensions, for example:

- Halving the inter-order distance would produce a $\sqrt{2}$ improvement.
- The etalon diameter necessary is directly proportional to the fibre size.
- Only using the Fabry-Perot to observe the hottest stars, and hence be able to use a lower resolution etalon.

However, the major problem with the current set up is the need to use the pre-disperser which was designed for use with the Michelson interferometer.

5.2.2 The Available Etalon

Of the etalons available the most suitable was a Queensgate Instruments' 85 mm diameter etalon which had been used for measurements of radial velocities of the Zodiacal light [98]. Its specifications are as given in table 5.1.

The restriction on useable diameter was necessary as the most suitable collimator available was a f2.9, 8″ focal length aerial photography lens, plus there was known to be a reduction in finesse at large apertures.

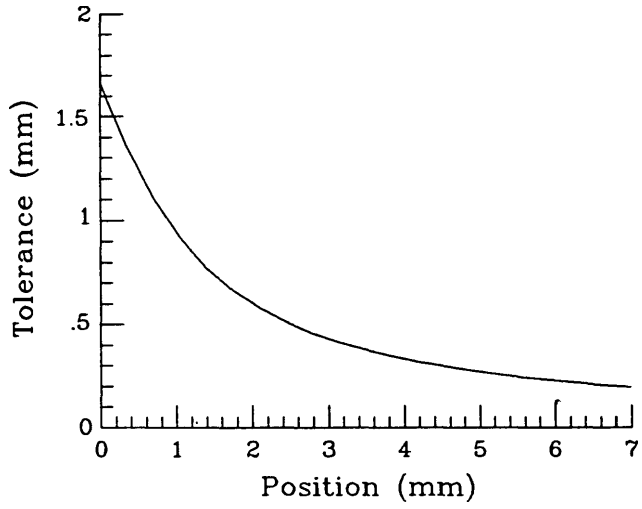


Figure 5.2: Positional tolerance for the available Fabry-Perot. This is based on a 0.3 Å width line, (as measured by the Fabry-perot). N.B. this represents the maximum error before the next fibre has a negative effect.

With this combination, for an on-axis wavelength of 5000 Å the order would be the 368th, which, (by rearranging equation 3.47), would give an inter-order distance of 13.6 Å. This, with a finesse of 30, gives a resolution of 0.37 Å (on axis). Therefore, the 600 μm fibres, combined with an 8″ focal length collimator, have an angular diameter of 0.17°, which, from equation 3.53, means that the angle, at which the loss of resolution for off-axis fibres equals the resolution of the etalon, is 1.45°. In the 368th order this is equivalent to 4998.4 Å, or a change in wavelength of 1.6 Å. However, an entire order is 13.6 Å, so this etalon can only cover about 12% of an order. Although this would be unsatisfactory for an instrument being used for astronomical observations, it was hoped that there were enough lines available to demonstrate the principle of multi-lining with the Fabry-Perot.

Figure 5.2 shows the maximum misalignment in the Fabry-Perot using a 0.3 Å line. (This was typical for the lines that were used with the Fabry-Perot.) For the maximum off-axis angle it is intended to use, an accuracy of better than 0.2 mm is required.

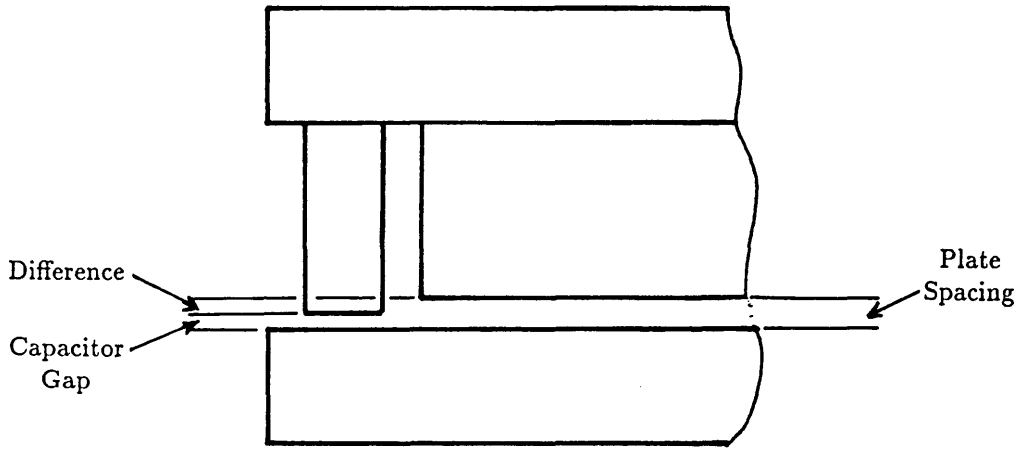


Figure 5.3: Difference in optical and capacitor gaps.

5.2.3 Building the Interferometer

Housing

Even using capacitance micrometry, the etalon is still affected by temperature, pressure and humidity changes. These can affect both the capacitance signal, (though this effect is reduced by using an air-spaced reference capacitor), and the optical gap of the etalon. The optical gap of the etalon is affected in two ways. Firstly, changes in temperature etc. affects the refractive index of the air in the gap. Ignoring affects on the capacitance micrometry, this is equivalent to 330 $\mathrm{m\,s^{-1}}$ for a change in temperature of 1°C and 90 $\mathrm{m\,s^{-1}}$ for a millibar change in pressure [78]. Secondly, although the capacitor pads are mounted on fused silica pillars and the etalon plates are made of fused silica, these are of slightly different thicknesses (figure 5.3). This means that the capacitance micrometry is unable to compensate for the expansion of this extra thickness with temperature. The difference in thickness is 42 μm, and as the thermal expansion coefficient of fused quartz is $5.5 \times 10^{-7}\,^{\circ}\mathrm{C}^{-1}$, this is equivalent to 75 $\mathrm{m\,s^{-1}\,^{\circ}C}$. Also, the plates can bow, so causing a change in the gap, because of temperature gradients in between the inner and outer sides of the plates. These effects can be reduced by putting the etalon in a temperature controlled pressure pot. This is doubly advantageous because of

$$\frac{n-1}{\rho} = \text{constant} \tag{5.1}$$

where ρ is the density [86, page 500].

As the pressure pot is sealed, it must maintain a constant density inside independent of temperature, (ignoring the effects of temperature and pressure on the dimensions of the pressure pot), which reduces the need for temperature control. There is, obviously,

still some need for temperature control to reduce the effects of the difference in thickness of the fused silica and to prevent distortions of the plates. However, instead of millikelvin being necessary, a one hundredth of a degree should be sufficient.

The Collimator and Camera Lenses

As mentioned above, an f2.9, 8″ focal length, ex-aerial photography lens was used as a collimator. Similarly to the Michelson, there were problems with vignetting. Consequently a field lens had to be used. As the limiting aperture was the collimator, the etalon being of larger diameter, an 8″ positive focal length lens was placed immediately in front of the fibres. A f3, 8″ focal length lens was used as the camera lens.

Stabilization

Previous tests on a CS100 control system, plus an etalon sealed in a temperature controlled pressure pot, have given a stability of, at best, 30 $m\,s^{-1}$ [79]. As it is hoped to be able to detect oscillations of less than a metre per second, obviously, this is unsatisfactory.

The majority of this noise is believed to be caused by temperature instabilities of the control electronics, giving an error of 326 $m\,s^{-1}\,°C^{-1}$ [99]. There are two possible ways of solving this, both of which could be used together. Either by very careful choice of, and temperature stabilization of all critical components, (which should be able to give a stability of 0.3 $m\,s^{-1}$, as developed by Butcher and Hicks [83]), or, alternatively, referring the etalon to a stable wavelength, either from a stabilized laser, spectral lamp or a very stable Fabry-Perot. It was decided to use an optical reference to stabilize the etalon.

The best reference source that was available, (at Imperial College), was the cadmium lamp. This has been in the past used as a standard wavelength and, without spending up to £25,000[1] on a stabilized laser, is probably the best choice. There are four main lines in the cadmium spectrum, a red, a green, a blue/green and a blue line. Because of the need to be able to separate the reference light from the signal, the green and

[1]The cost of a portable iodine stabilized laser [100] in 1985 from

Frazier Precision Instrument Co., Inc.,
210 Oakmont Avenue,
Gaithersburg, MD20877, USA

blue/green lines could not be used, and because the etalon coatings were unsuitable for the red line, the blue line was chosen. Two photomultipliers were used, one for the signal and one for the reference. The reference line was separated out using a blue/green dichroic and a cadmium blue filter. So that there would be no reference light getting into the signal channel, an electronically controlled shutter was used. See figure 5.4 for a schematic of the pressure pot, etalon, lenses, filters etc.

Photon Counting

Two photomultipliers were needed. For the reference channel an E.M.I. side window photomultiplier was used. This was suitable as high count rates were expected and the signal from this was to be nulled, (see later), so the problem of a relatively high dark count is reduced. For the signal channel, it was originally planned to use a cooled R.C.A. 31403A/02 photomultiplier, which would be suitable for the comparatively low count rates from stars. For observing the Sun, however, another E.M.I. side window tube was used as it had a higher count rate and did not need cooling, so could be left running.

Twin MLV100TB circuits from Lecroy were used as discriminators. The pulses out of the circuits were converted into TTL pulses and recorded on twin scalers.

Increased Resolution in the Capacitance Micrometry

The CS100 is able to be controlled digitally, i.e. by feeding the CS100 with a twelve bit number, an offset is produced in the position of the plates. In the standard CS100, with a 92 μm gap etalon, and for a wavelength of 5000 Å, the minimum offset (1 bit) is equivalent to about 1300 $\mathrm{m\,s^{-1}}$. Hence the etalon could drift by up to ± 650 $\mathrm{m\,s^{-1}}$ before any correction would be made. Obviously as oscillations of less than a metre per second are being searched for this is unsatisfactory.

The CS100 has three sets of digital inputs for controlling the etalon: the X and Y channels, which control parallelism, and the Z channel which controls the gap. An extra Z channel was added to the CS100, (referred to as the fine-Z), in which one step equals about one two thousandth of the step of the standard or coarse-Z channel. This means that one fine-Z step is equivalent to about 0.6 $\mathrm{m\,s^{-1}}$ using the current etalon.

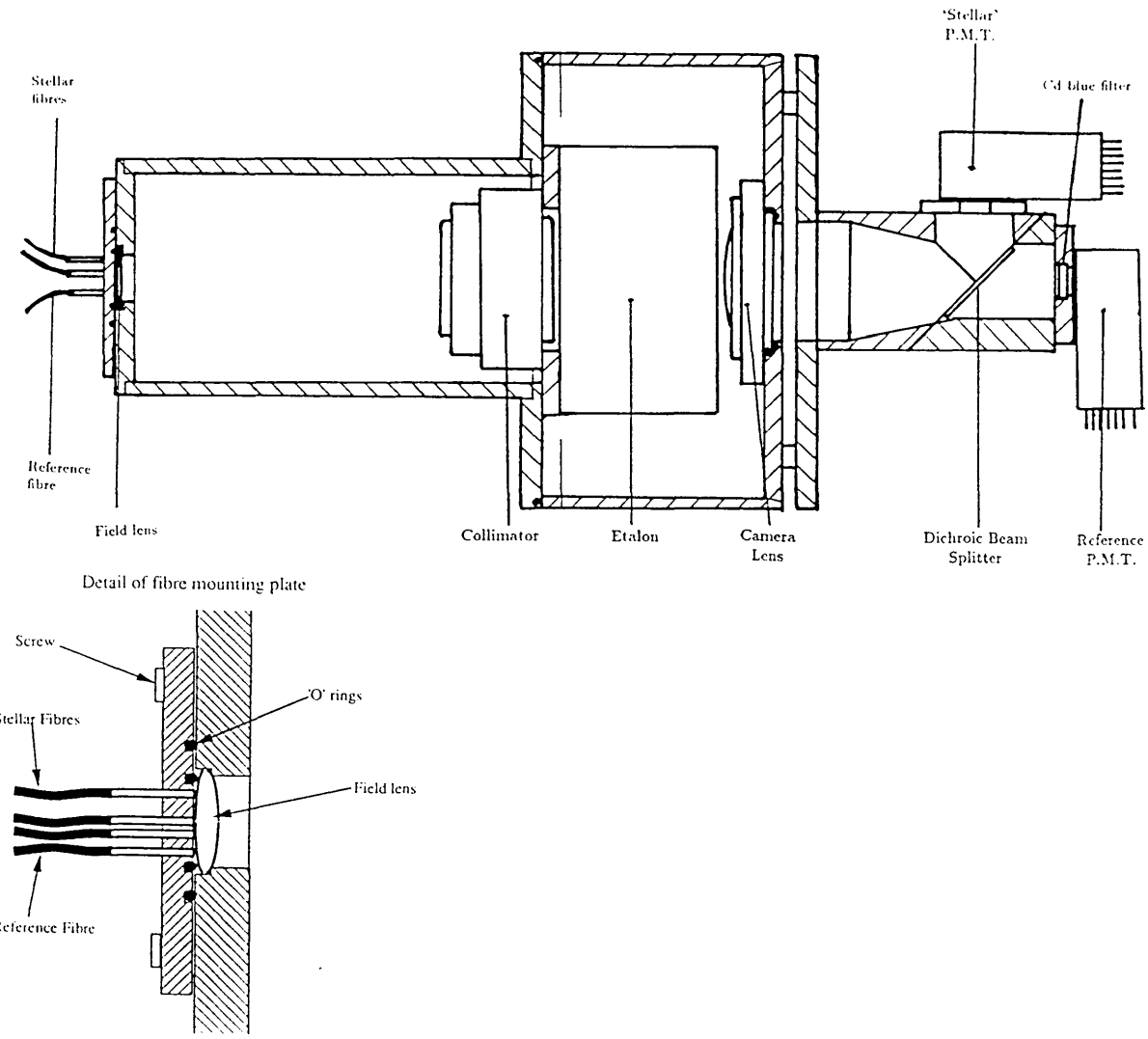


Figure 5.4: The Fabry-Perot radial velocity interferometer.

The Digital Control System

All the digital control electronics were in a double rack. The system was based around the Rockwell 6502 family of chips. The actual processor was on a SBC (single board computer) module. The program was stored in two 8K eprom emulators, which are RAM with a battery back up. Four VIA's, (6522 versatile interface adaptors), were used for controlling the CS100, one each for the X, Y, Z and fine-Z channels. The counts were recorded on two scalers, each based around two 74LS393 counters, controlled by VIA's. The data is outputted and the instrument controlled by two RS232's, (6551 serial interfaces). One outputs data to, and receives commands from, a Lear-Siegler dumb terminal, and the other outputs data to a Cristie digital tape recorder, (either CS5 or CS6).

5.2.4 Controlling the Instrument

The Fabry-Perot was controlled using a program written in 6502 assembler on a Rockwell Aim-65 and run on a single board computer (SBC). The program was stored on two 4K eprom emulators. Whilst a few routines were copied from books (e.g. Leventhal [101]), though often with modifications, the vast majority had to be specially written. No claim is made for any rigorous technique in writing code, though extensive use was, (naturally), made of subroutines, (and the odd `JMP`, equivalent to the much derided `GO TO`), even so, it was able to be swiftly redesigned, (sometimes several times), under operational conditions, i.e. whilst observing. Although the software was never used with the multi-line system on stars, it has been used twice in Tenerife, on the 60″ IRFC, with a single line, for observing Ap stars [20,22,21].

All the programs are able to be called from a menu which is put up as soon as the digital rack is turned on.

Almost any nights observing can be divided into four phases: setting up the instrument, finding the star, preparing to observe and taking the data. To understand the techniques used it is probably best to tackle these in reverse order.

Chopping

The most efficient way of using the instrument to detect changes in the position of the line is by chopping the instrumental passband from one side of the line to the other, and taking the ratio $(A-B)/(A+B)$. This is true because the chop points chosen are

naturally the two points which give the largest change in $(A - B)/(A + B)$ and hence are most sensitive to radial velocity changes. If scanning was used, and the position of the line found by doing a 'best fit' for example, a lot of the time would have to be spent counting on points that were less sensitive to changes in radial velocity.

The integration time required is governed by the minimum period it is expected to find. For any given frequency of sampling, the highest frequency that can be found is half the sampling frequency. This is called the Nyquist frequency. Obviously it does no harm to be sampling faster than that necessary to detect the highest frequency expected to be present, (so long as the amount of data being produced does not exceed the ability to deal with it). In fact it can be an advantage, in that glitches 'damage' a far smaller portion of the data, less reliance is placed on the stability of the etalon in between consulting the reference source, and fewer bytes are needed to deal with the data, as fewer counts per point are obtained.

To reduce noise from changes in sky transparency, (due to clouds etc.), the Fabry-Perot is chopped at a frequency of 10 Hz,[2] so that it spends only 50 ms on each side of the line, with the counts being summed over the required integration time, (in the correct channel of course). This is slightly less efficient as far as counting goes, as there has to be a 1 ms dead time for each chop to allow the etalon to settle down. However, ignoring other sources of noise, for a linear, (with time), change in sky transparency the improvement in accuracy compared with sitting on one side of the line for half the time, and then moving to the other half, is the ratio of the total time per point divided by .1 of a second. This gives, for a typical integration time per point of (say) ten seconds, a hundredfold increase in accuracy.

The Reference Signal Similarly to finding the radial velocity, the best way to find the error in the etalon's gap is by chopping the etalon's passband on the two sides of the reference line. Ideally, the reference line should continuously monitor both the stellar and reference signals. This, unfortunately, with the present instrument has many problems:

- Because of the restricted range in useable off-axis angles, even if the reference line was used off-axis, it would not necessarily appear at the same phase as the stellar line.

[2]Having read Warner [56] and from equation 2.2, this appears to be not fast enough to deal with scintillation on the 60″ IRFC. A chopping frequency of at least 20 Hz should have been used.

- Because of the proper motion of the stars, (and the Heliocentric velocity of the Earth), the position of any reference line would have to be made adjustable.

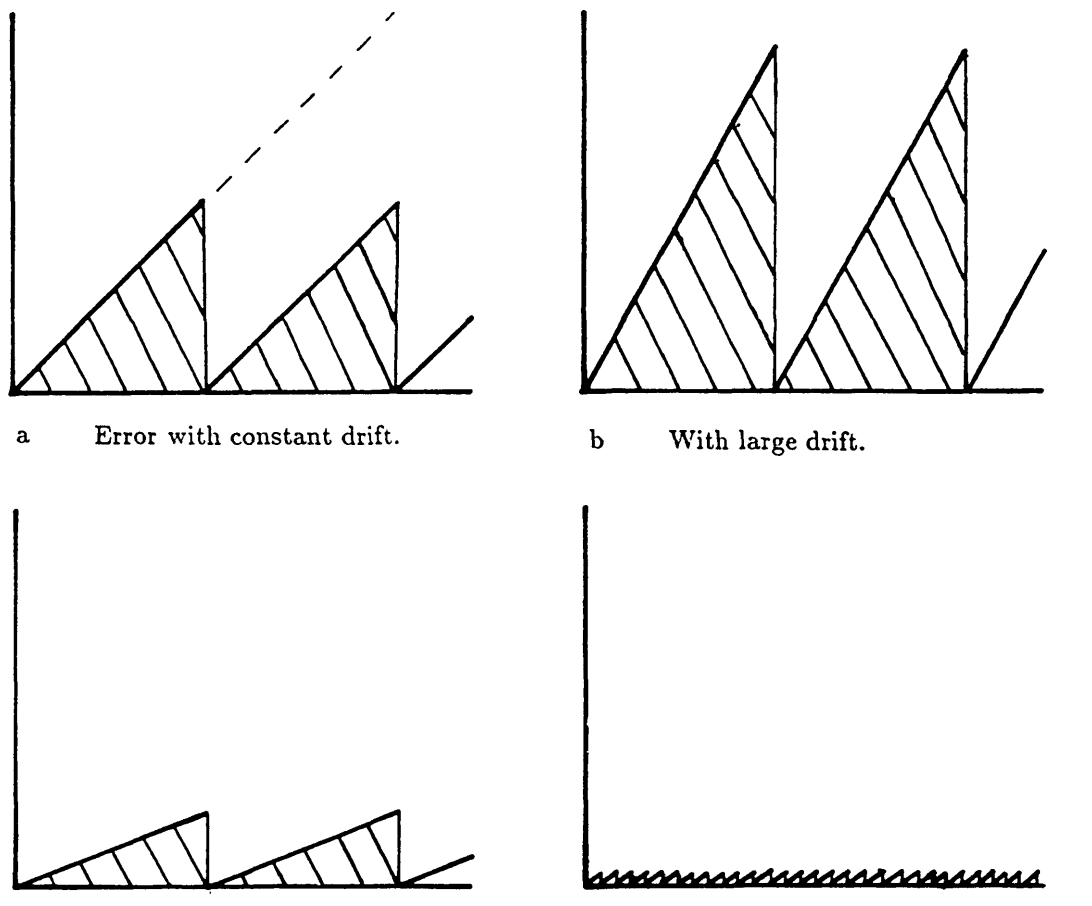
- Because of the large wavelength range being used, along with the restricted wavelength range of the etalons coatings, it would be difficult to separate (by using filters) the reference and stellar lines. This would also lead to extra light loss. Even using stops in front of the photomultipliers might give problems with 'spillage' from the very bright reference source into the signal channel because of scattered light, multiple reflections etc.

Hence, it was necessary to offset from the reference line to the stellar line. Obviously with the CS100 this could be done very easily. Also, fortunately, with the CS100 the error in offsetting was much smaller than the absolute error. For a change in gap of 6328 Å, the error was less than 0.5 Å [99]. For a 92 μm gap etalon this was equivalent to an error of 163 $\mathrm{m\,s^{-1}}$ over an offset of two and a half orders. For smaller offsets, the error was expected to be proportionately smaller, the maximum size offset that was necessary being half an order. This is, of course, the error per point; the error falls as the square root of the number of times the etalon is offset.

By offsetting to the reference line and measuring the ratio $(C - D)/(C + D)$, the error in the gap can be found. The amount the etalon gap has to be corrected is given by:

$$\text{Correction} = \frac{C - D}{C + D} \times k_1 \tag{5.2}$$

However, in the case of a drift in the gap, this method is too simple and leads to errors. In figure 5.5a, the dotted line represents the behaviour of the etalon if there was no correction applied. The shaded triangles represent the behaviour of the etalon with the above correction applied, (ignoring photon statistics). The areas under the triangles represents the error in average position of the gap. For a steady drift this error would just act as a constant offset. However, if the drift changes the error can increase or decrease depending on the direction of change, (see figures 5.5b and c). This can be removed by continually correcting the gap at a rate proportional to the slope. As the minimum correction possible is one step this means that there is still some error, but this is much reduced, (figure 5.5d).



a Error with constant drift.

b With large drift.

c With small drift

d After applying continuous correction.

Figure 5.5: Errors caused by a constant drift.

The size of this correction, called the drift term, is worked out by adding a number proportional to the presents point's error to the previous point's drift term, i.e.

$$D_i = D_{i-1} + \frac{C-D}{C+D} \div k_2 \tag{5.3}$$

There is also a correction that could have been applied which depends on the difference between the errors for the present and previous points i.e.

$$T = k_3 \times \left[\frac{C_i - D_i}{C_i + D_i} - \frac{C_{i-1} - D_{i-1}}{C_{i-1} + D_{i-1}}\right] \tag{5.4}$$

It was decided not to use this term as it would make only a negligible correction.

Minimizing the Error in the ratio $(A-B)/(A+B)$.[3] As the count rates, gradients etc. of the reference and stellar lines are different, it was necessary to work out the ratio of time spent on the reference line to time spent on the stellar line for minimum error.

As well as the error produced by photon shot noise in the stellar signal, there is an error caused by the etalon being at the wrong gap due, in part, to the photon shot noise in the reference line. Consider the case of an etalon at the 'correct' gap. Because of the photon shot noise in the reference source, the ratio has a non-zero value of

$$R_r = \frac{C-D}{C+D} \tag{5.5}$$

This causes the 'correct' values of A and B, (for a linear slope), to change to

$$A' = A + \frac{R_r}{2}\frac{S_*}{S_r}(A+B) : B' = B - \frac{R_r}{2}\frac{S_*}{S_r}(A+B) \tag{5.6}$$

where S_* and S_r are the slopes of $(A-B)/(A+B)$ and $(C-D)/(C+D)$ respectively. Therefore

$$\delta\lambda = \frac{1}{S_*}\left[\frac{A'-B'}{A'+B'}\right] \tag{5.7}$$

$$= \frac{1}{S_*}\left[\frac{A(1+R_rS_*/S_r) - B(1-R_rS_*/S_r)}{A+B}\right] \tag{5.8}$$

From equation 3.12 and remembering that the error in $(C-D)/(C+D)$ is $1/n_r$, (see equation 3.16).

$$\sigma_\lambda^2 \approx \frac{1}{S_*^2}\left\{A\left[\frac{2B}{(A+B)^2}\left(1+R_r\frac{S_*}{S_r}\right)\right]^2 + B\left[\frac{2A}{(A+B)^2}\left(1-R_r\frac{S_*}{S_r}\right)\right]^2\right.$$

[2]These calculations were done, unfortunately, after most of the data had been taken.

$$+\frac{1}{n_r}\left(\frac{S_*}{S_r}\right)^2\Bigg\} \tag{5.9}$$

$$\approx \frac{1}{S^2}\Bigg\{\frac{4AB^2}{(A+B)^4}\left(1+R_r\frac{S_*}{S_r}\right)^2+\frac{4A^2B}{(A+B)^4}\left(1-R_r\frac{S_*}{S_r}\right)^2 \tag{5.10}$$

$$+\frac{1}{n_r}\left(\frac{S_*}{S_r}\right)^2\Bigg\} \tag{5.11}$$

Using $A \approx B \approx n/2$,and $R_r \equiv 1/\sqrt{n_r}$ gives

$$\sigma_\lambda^2 \approx \frac{1}{S_*^2}\left\{\frac{1}{n_*}\left[1+\left(\frac{1}{\sqrt{n_r}}\frac{S_*}{S_r}\right)^2\right]+\frac{1}{n_r}\left(\frac{S_*}{S_r}\right)^2\right\} \tag{5.12}$$

$$\approx \left\{\frac{1}{S_*^2 n_*}+\frac{1}{S_r^2 n_r n_*}+\frac{1}{S_r^2 n_r}\right\} \tag{5.13}$$

Let the integration time be T and the stellar and reference count rates be N_* and N_r respectively. If the integration time for a stellar point is t, then

$$\sigma_\lambda^2 \approx \left\{\frac{1}{S_*^2 N_* t}+\frac{1}{S_r^2 N_* N_r (T-t)t}+\frac{1}{S_r^2 N_r (T-t)}\right\}. \tag{5.14}$$

Differentiating σ_λ with respect to t

$$\frac{\mathrm{d}\sigma_\lambda}{\mathrm{d}t} \approx -\left\{\frac{1}{S_*^2 N_* t^2}+\frac{T-2t}{S_r^2 N_* N_r\left[(T-t)t\right]^2}-\frac{1}{S_r^2 N_r (T-t)^2}\right\}\sigma^{-1/2} \tag{5.15}$$

For a minimum $\mathrm{d}\sigma_\lambda/\mathrm{d}t = 0$, and ignoring the middle term as it is effectively the reciprocal of the square of the number of counts,

$$\frac{1}{S^2 N_r (T-t)^2} = \frac{1}{S_*^2 N_* t^2}. \tag{5.16}$$

Replacing $T - t$ with t_r leaves

$$\frac{t_*}{t_r} = \frac{S_r}{S_*}\sqrt{\frac{N_*}{N_r}}. \tag{5.17}$$

Even more importantly than the ratio of the counts, the amount of time to be spent on the stellar to the reference line depends on the ratio of their slopes.

Isolating the Stellar and Reference Light To stop the stellar light affecting the reference signal, a narrow band cadmium blue filter was used in front of the reference line's photomultiplier, and to stop the reference light affecting the stellar channel, an electronic shutter had to be used. This was operated by the control program.

The Chopping Software Having selected the chopping program, the required positions, (in CS100 steps), and the times for the stellar and reference lines are inputted. The correction constant, k_1, is also entered. Putting this to zero effectively turns off the

reference system. After confirming that the input data is correct, the program starts counting on the reference line. Just before starting to count on the stellar line for the first time, the time is outputted, (if the real time clock module is in place).

The parts of the program that move the etalon, start and stop the counters, deal with the counts, work out the required corrections and the next chop position, are part of various interrupt service routines, (ISR). Interrupts literally interrupt the processor, (if they have been enabled), and cause it to go to a different program, called the interrupt service routine, controlled by interrupt vectors, (which contain the location of the ISR). The chopping routine relies on timers located on VIA's to cause the necessary interrupts. The 6522 VIA has two types of timer, T1 and T2. T2 is the simplest and is just used to time for a single set period. T1 can also do this. As well, it can also produce an interrupt every so many milliseconds without having to be reset. A T1 timer acts as the main source of interrupts, producing an interrupt every 50 ms. After saving registers etc., the first thing the ISR does is to start a T2 timer timing for $\approx$ 1 ms. Then it stops the scalers photon counting and latches the displays. It then has to decide whether the next chop is to be on the star or reference line. If it is a 'normal' point it chops the CS100, records the counts from the scaler, adds them to the correct data store (which are three bytes long), works out the next position for the etalon, sets up the next set of interrupt vectors, (for the T2 timer), and decrements the loop counter. If it is the last reference point it will set the loop counter equal to the number of star chops. The flow chart for a reference point is shown in figure 5.6. Control then returns to the main program after making any adjustments for the drift, and restoring registers etc. Meanwhile the T2 timer is counting down for 1 ms. This is to give the etalon time to settle down after having been chopped. When the T2 timer finishes counting, it causes an interrupt. This calls one of two secondary ISR's, either for a stellar chop or for a reference chop. These start counting on their respective scalers and reset the interrupt vectors for the main ISR. Figure 5.7 explains the timing of the interrupts.

Whilst the method for the majority of the chops on the stellar line is very similar to that for the chops on the reference line, the first two chops on the stellar line per point have to be very different. This is because they involve working out the correction and the new drift term from the last reference point. The correction is worked out in a slightly convoluted manner. First of all $(C + D)/(C - D)$ is worked out and then this result is divided into the correction term. It is done this way rather than the obvious

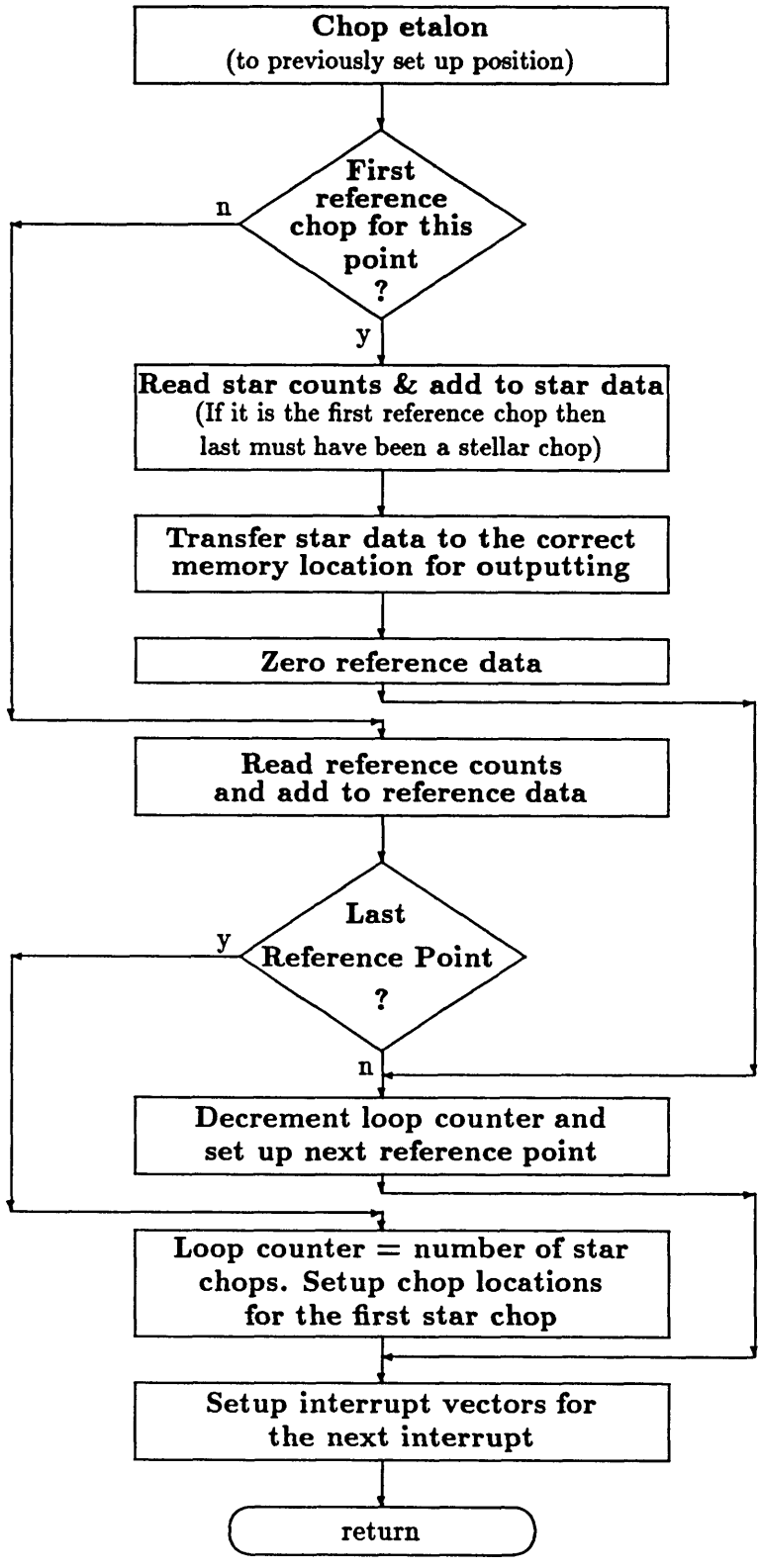


Figure 5.6: Flow chart for a 'normal' reference point. The flow chart for a 'normal' star point is very similar.

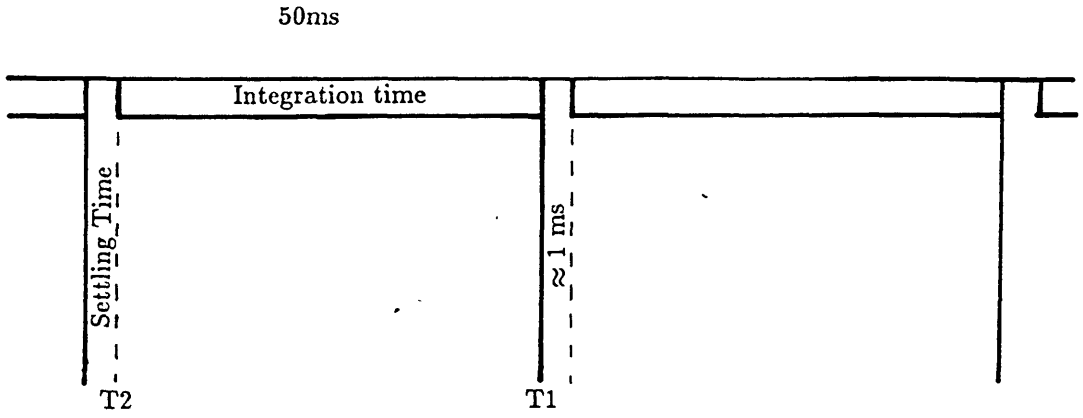


Figure 5.7: Timing of the interrupts for a 'normal' chop.

way as per equation 5.2 so that there would be no multiplication, so removing the danger of overflows causing errors.

As the correction for the drift term is applied only once per chop (in the main ISR), it is necessary to work out how many chops come in between each drift correction. This is done by dividing the total number of chops by the drift term. For simplicity, it was decided to apply the drift steps at the maximum rate of one step per chop. Obviously the maximum drift rate is governed by the number of chops; for a 20 second integration period, the maximum drift rate would be 400 steps per point. Of course this leads to errors for drift rates higher than the number of chops per point. Also, large drift rates, which are an appreciable fraction of the number of chops, produce errors from rounding fractions down. However, drifts this high were not expected. The new drift term is obtained by dividing the correction by a constant and adding it to the old drift term. Division is used to reduce the size of the change in the drift rate so averaging out noise. For simplicity, the division is done by shifting, hence can only be by factors of two, four, eight etc. When the fine-Z is altered, be it by the correction term or the drift term, if the fine-Z goes outside the range +2047 to -2048, it is zeroed and the coarse-Z position altered. Also, a warning flag is produced.

Working out the correction etc. from the previous reference point takes time. Also, it was felt more satisfactory to make the durations of counting on each side of the chop position equal, rather than giving one side a few ($\approx$ 15 ms) seconds longer, even though this would only appear as a small offset. Instead of running the standard interrupt sequence and shortening both of the first two star chops by an amount equal to the maximum possible time it takes to do the calculations, it was decided to distribute half

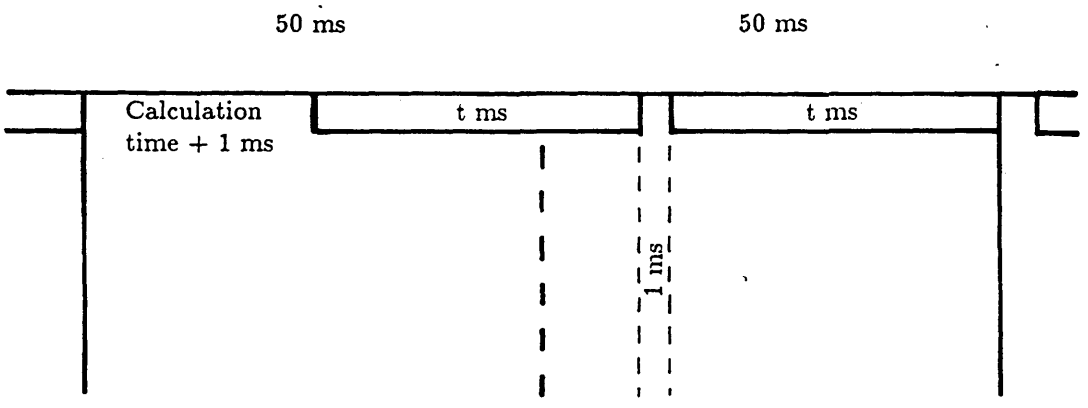


Figure 5.8: Timing of interrupts for the first two chops of each point. $t = (100 - \text{calculation time} - 2)/2$ ms

the calculation time over each chop. However, the calculation time differs from point to point, depending on the difference in counts, the number of counts, the correction constant k_1 etc., so to make a more 'interesting' program, (on the excuse that every millisecond *counts*), the time it takes to do the calculations is timed using a T2 timer. All interrupts are turned off. The time from the T2 timer is used to find the time remaining from the first two chops. Counting is started and a T2 timer set running for half the above time with its interrupt enabled, (turned on). When the main T1 timer finishes, its flag is cleared, (i.e. preventing it immediately interrupting when it is re-enabled), and all interrupts re-enabled. As everything has been done in the main ISR that is normally done in the secondary stellar ISR, there is no need for it to be called, so when the above T2 causes an interrupt, it calls the main ISR, so starting on the second stellar chop for that point. This runs as for a normal chop point, (except for its starting position, timewise), and sets up the interrupt vectors for the secondary stellar ISR. The third stellar chop is called using the normal T1 interrupt. Hopefully figure 5.8 helps to clarify this.

The shutter is opened, using a handshake line from a VIA, by a separate interrupt service routine which is called by a T2 interrupt 'arranged' in the last call to the stellar secondary ISR before the first reference chop. It is closed by the first stellar chop.

The main program outputs the data every three points. As well as the counts on the stellar line, it outputs the counts on the reference line, the ratio $(A - B)/(A + B)$, the fine-Z position, the correction term and the drift term. Also, it outputs whether there has been a fine-Z overflow in the last three points. All of these are outputted to

both the terminal and the CS5 or 6 tape recorder. As well as this, the total counts from every thirty two star chops, (i.e. every 1.6 seconds), are outputted to the terminal as an aid to guiding.

To finish 'F' has to be pressed which, after the current three points have been finished, leads to the time being outputted and a request for confirmation. If this is given the various chop positions etc. are outputted, and if not, the program continues running.

As each point is $\approx$ 50 ms long and the size of the scalers is two bytes, the maximum count rate in either the stellar or reference channels is over a million counts per second, which is faster than the photomultipliers/discriminators can handle. The stores for the counts in the program are three bytes long, so the program is able to deal with over sixteen million counts per point.

Scanning

The reference line has to be scanned to find the best points to chop on, and the corresponding best value for k_1. As well as finding the best chop points, scanning the stellar line gives the change in ratio per Å, (hence $\mathrm{m\,s^{-1}}$), and allows the stellar line to be centred in the filter profile.

Similarly to when chopping, to reduce the effect of changes in sky transparency the etalon needs to be scanned very rapidly, repeating as necessary to give the required integration time. The scan routines that were written scan over twenty points, spending 50 ms on each point, hence one second per scan. Except for an increased integration time, using the rapid scanning routine enables good line profiles to be obtained, even whilst observing through thin cloud.

The Scanning Software The first scanning routine that was produced needs to be told whether it is a stellar or reference line scan, the starting position, the number of CS100 steps in between each point and the number of scans required. It then gives the option of saving the scan on tape. Having confirmed the above information, it then starts scanning. When the program has finished scanning, the data is outputted both as a string of numbers and as a histogram of asterisks. The graph is plotted having subtracted the minimum count rate to give maximum clarity with shallow lines. The maximum count rate, (minus the minimum), is divided by 64, (by shifting), to give the scale. As the software can not handle fractions, this means that the peak of the graph can be represented by between 33 and 65 asterisks. If the difference between

the maximum and minimum counts is less than 64 then each asterisk equals one count. Originally it could do only 255 scans which was enough for the Sun, but experience in Tenerife with Ap stars led to it being modified so that it could do up to 65535 scans. The maximum number of counts for any one point can go up to a three byte number.

The above scanning routine was satisfactory with high count rate sources, such as the cadmium lamp or the Sun, but for dimmer stars it has a number of disadvantages. These were due to the number of scans it was going to do having to be chosen before starting scanning and not being able to see the results until it had finished. Consequently, if the wrong number of scans was chosen, (normally too few), then the whole process had to be repeated for a longer time. Also, if the scan was unsatisfactory in some way, this could only be found out when it had finished and, last but not least, it provided no entertainment for the observer.

Consequently a drastic rewrite was undertaken. The new program outputs the data every three points. The part that is actually controlling the etalon, photon counting etc., is completely new and is in an interrupt service routine. This is so the main program can be plotting whilst the scalers are counting, so that no time is wasted. It re-plots the data every three scans as this is about the fastest rate it can plot. The new plots are not done by simply scrolling, but by using the ASCII home code, and a combination of asterisks and blanks, each plot is plotted on top of the previous one, and seems to grow out of it, so providing suitable interest. Instead of inputting how many scans are required the scanning routine will keep on running until 'F' is pressed, so enabling the spectrum to be monitored as it is taken, and either, if it is unsatisfactory, stopped, or if it is satisfactory, left running until the required noise level is reached. The program also outputs the cumulative minimum, maximum and current, (the total over the last three scans, as an aid to guiding), counts. After 'F' has been confirmed, the program gives the option to store the scan on tape. The counts and final scan are then re-displayed and the initial starting positions etc. outputted.

The program is run from a menu with the following options on it:

(1) `Old scanning routine`—the original scanning routine.

(2) `New scanning routine`—the modified scanning routine.

(3) `Repeat scan`—repeats the new scanning routine with the last starting conditions.

(4) `Continue scan`—continues with the last scan.



Figure 5.9: Screen display for scanning routine. (Actually the multi-line scan from figure 6.18.)

(5) Return to main menu—self explanatory.

For an example of the output see figure 5.9

Finding the Star This is basically a routine that enables the etalon to remain at a chosen position, whilst the scalers count, and outputs the results every (selected), few seconds. It has proved to be very useful for lining up the fibre on the telescope and finding the best place to guide on. To escape from it press 'F'.

Improving the Finesse Generally the etalon has to be set up by eye before the interferometer is assembled. Though this can be very accurate, it is possible for the parallelism to drift, (though probably only by a small amount), and a final adjustment after assembly can usually give a slight improvement. Also, if the balance conditions change drastically for some reason, it would be useful to be able to improve the finesse whilst the interferometer is assembled.

The first part of this program allows offsets to be put in to the X and Y channels of the CS100 using the terminal's keyboard. The next option is a less than successful method of trying to maximize the finesse by hand. The intention was to keep the

etalon at the peak of an emission line by continually moving Z one way or the other, depending on whether the counts went up or down. This was supposed to enable the X and Y offsets to be altered by hand via the front panel of the CS100, whilst the etalon automatically remained on the peak of the line. However, because of the only form of feedback being the scalers, which are altered every 50 ms, it has proved to be difficult if not impossible to use. Integrating for longer, and displaying the result on the monitor would probably improve it.

A routine was written to improve the finesse automatically. It does this by counting on the peak of the line and four points either side for the present X and then for $X+\delta X$. To reduce the affect of the lamp changing in brightness, this is done by counting for 50ms on each point and repeating the process several times. If the maximum count occurs for the new X position, the process is repeated for another $X+\delta X$, shifting the Z value of the peak, if necessary. If it occurs for the original X position, the sign of δX is reversed and the process continues. On the second reversal of sign the routine is considered to have reached the best value of X for that value of δX, and the process is repeated for Y. δX is then halved and the counting time doubled and the routine continues until δX reaches one. The program starts with δX equal to thirty two. This program works up to a point, but it can only improve the finesse if the etalon is nearly parallel to start with, and, it takes a long time.

Probably the best method of improving the finesse was found to be trial and error using the finesse measuring routine. This first of all finds the peak of the line by running the original scanning routine three times with fifty, ten and one CS100 steps in between each point. The scanning routine originally used to find only the value of the maximum count rate and was slightly modified so that it kept the maximum count rate's position as well. Then it finds the half maxima points for this order to give the line width, and then one of the half maxima points of the next order to give the inter-order distance. From these it works out the finesse.

Chapter 6

Instrumental Tests

The tests can be divided into

- Stability of the single line Fabry-Perot with the optical reference.
- Alignment of the echelle pre-disperser.
- The multi-lined Fabry-Perot
- The multi-lined Michelson.

6.1 Stability Tests on the Single Line Fabry-Perot

Before joining the Fabry-Perot to the echelle spectrometer, it was decided to find out how stable the interferometer was as a single line instrument. All the tests were done using the cadmium blue line as both the 'stellar' line and the reference line. The justification for this was that the intention of the project was to measure the stability of the *interferometer*, not the lamp. Though it was possible that the lamp drifted in frequency, in a 'production' model a highly stable laser could have been used—e.g. an iodine stabilized laser, for which accuracies of one part in 10^{14} are claimed [100] or a laser using some form of polarization stabilization, for which stabilities of one part in 10^{10} have been achieved for periods of an hour [102]. Ignoring noise in the cadmium lamp, *(and if the optical servo is working correctly)*, the interferometer was able, by chopping on the reference line, to be set to the correct gap for the cadmium blue line. What was needed, however, was for the interferometer to be at the correct gap for the *stellar* line. As these two gaps are different, the CS100 has to move, (or offset), from one to the other. Consequently the stability of the interferometer, (ignoring noise in

the reference signal), depends on the ability of the CS100 to reproducibly move from the (corrected) reference position to the stellar line; therefore, *by measuring the offset stability of the CS100, the stability of the interferometer was being measured.* This could be done by using the *same* line in two Fabry-Perot orders to represent the stellar and reference lines. Offsetting between them then measured the radial velocity stability of the interferometer.

All of the initial tests, until the advent of the 'new' box, (section 6.1.4), were done with very little insulation being used. It would probably be best to describe it as glorified draught proofing. For most of the tests below, the interferometer was thermostatically temperature controlled using a 'foil' heater wrapped around the central bulge housing the etalon. This appeared to have no effect whatsoever—probably because the temperature control was only localized. (See section 6.1.4, however.)

6.1.1 Stability of the Cadmium Lamp

Pietraszewski *et al.* [77] had claimed noise levels of down to 20 cm s^{-1} with the Michelson interferometer stabilized using the cadmium lamp. Although this was greater than the r.m.s. signal from the Sun, it was of the required order.

Problems with the 50 Hz mains frequency

At first, however, there was a very high level of noise, (figure 6.1), with the fine-Z error being in the order of hundreds of points. Watching the data being outputted, showed the size of the noise increasing and decreasing. Beating of variations in mains frequency, (via the brightness of the cadmium lamp), with the chopping frequency was suspected. Consequently a lamp frequency controller was built. This enabled the direction of the current in the lamp to be changed, independent of mains frequency, using a signal generated in the computer. This reduced the noise in the signal enormously, (see later figures). Whilst it is suspected that using this reduces the lifetime of the lamps, the same lamp has been used for a few hundred hours with the lamp controller.

6.1.2 Selecting the Optimum Gain and Drift Terms

The first thing to establish was what were the optimum gain and drift terms. A series of runs were made chopping on the cadmium line in one order for the reference, and staying on the cadmium line in the *same* order to represent the 'star'. As the CS100 is

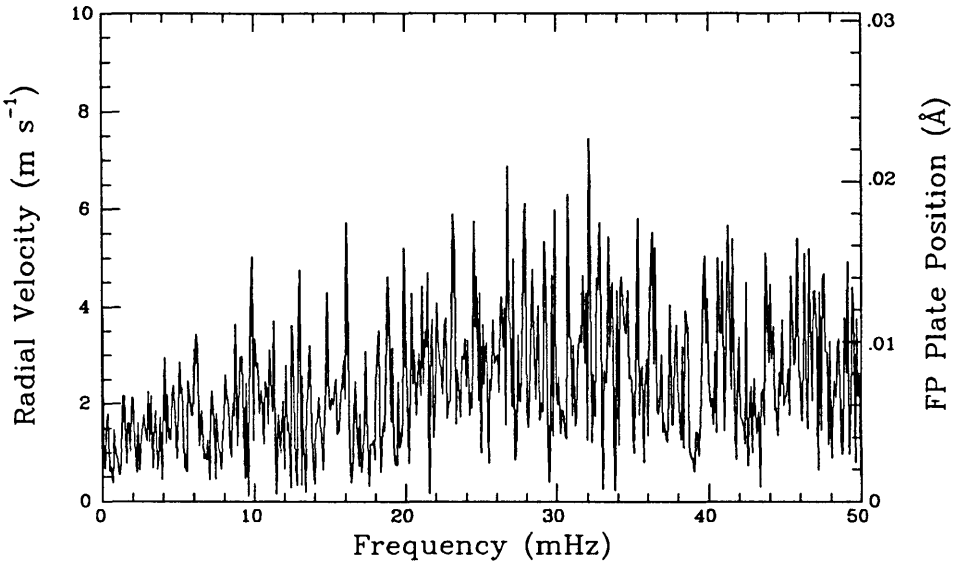


Figure 6.1: FFT of the signal without the lamp frequency controller.

only able to be stabilized at an offset equivalent to the reference line position, normally, for the 'stellar' line position, the CS100's offset stability has to be relied on. By staying on the *same* pair of chop points for both the reference and 'star' positions, drifts in the offset can be eliminated, (except between the two chop points on either side of the line), so leaving just the noise generated by the servo-system, (plus electronic noise and photon shot noise of course). Hence, the best gain and drift can be found.

Further Problems

Initially there were some peculiarities in the Fourier Transform. The first of these was a very sharp peak corresponding to every three points. This was puzzling as it appeared only in the 'stellar' data and remained what ever was tried with the servo gain etc. It was realized, however, that the data was being dumped to tape every three points. That this was the reason was confirmed by reducing the time that the etalon was spending on a 'stellar' point, which was when the instrument was dumping the data, so increasing the percentage of the counting time being potentially affected. This magnified the effect enormously. To test if it was pickup from the CS5, (presumably the motors), rather than noise generated in the computer program, the CS5 was moved to about fifteen feet away from the rest of the instrument. This solved the problem. To find out whether it was the photon counting or the CS100 being affected, the CS5 was returned to its

previous position, (*on top of the CS100*), and the interferometer set for zero chop on top of a deliberately low finesse peak to *minimize* any signal from pick up in the CS100. As no signal appeared, this seems to have confirmed the hypothesis that the CS100 was being affected.

Another peak was also present which corresponded to a period of about 26 seconds. This peak was only present if the lamp frequency controller was on, and was independent of the position of the lamp frequency controller. Using an oscilloscope to watch both the signal on one of the pins of the VIA controlling the etalon gap and the signal to the lamp frequency controller, showed that they were going in and out of phase with a period of approximately 52 seconds, (for 360° phase change). Carefully re-reading the data sheets implied that the T1 timer in free running mode took an extra 2 μs than the time that had been input to the timer so that the time can be loaded into the counters. This was confirmed by experimenting with very short time periods and looking at the results on an oscilloscope. Reducing the time put into the T1 timers by the necessary 2 μs, for both the chop period and lamp frequency controller, solved the problem.

A New Method of Handling the Drift, Plus Finding the Optimum Gain

Having dealt with the spurious peaks, the series of runs were continued. Drifts of one, a half, a quarter and zero were tried, with usually the gain calculated from the slope, (normally about thirteen thousand), and then with gains of around eleven thousand and around nine thousand. Higher gains than the 'theoretical' tended to be very noisy. Figure 6.2 shows some examples. Typically, increasing the gain tended to increase the high frequency noise, but possibly decreased the low frequency noise slightly. Reducing the drift term produced less noise, with the lowest noise occurring with zero drift. However, these were with quite small drifts. Experience in Tenerife had shown a zero drift term produced large errors with larger drifts, hence a slightly different strategy was adopted. This was that if the error was positive, the drift rate was increased by one, if the error was negative, the drift rate was decreased by one, and if zero, left the same. This seemed to give satisfactory results.

The different gains, so long as they were not much more than the theoretical optimum, do not appear to make much difference to the performance of the servo-system. Consequently, to benefit from the possible slight decrease in 'low' frequency noise, (actually the area of interest), it was decided to use just under the optimum gain.

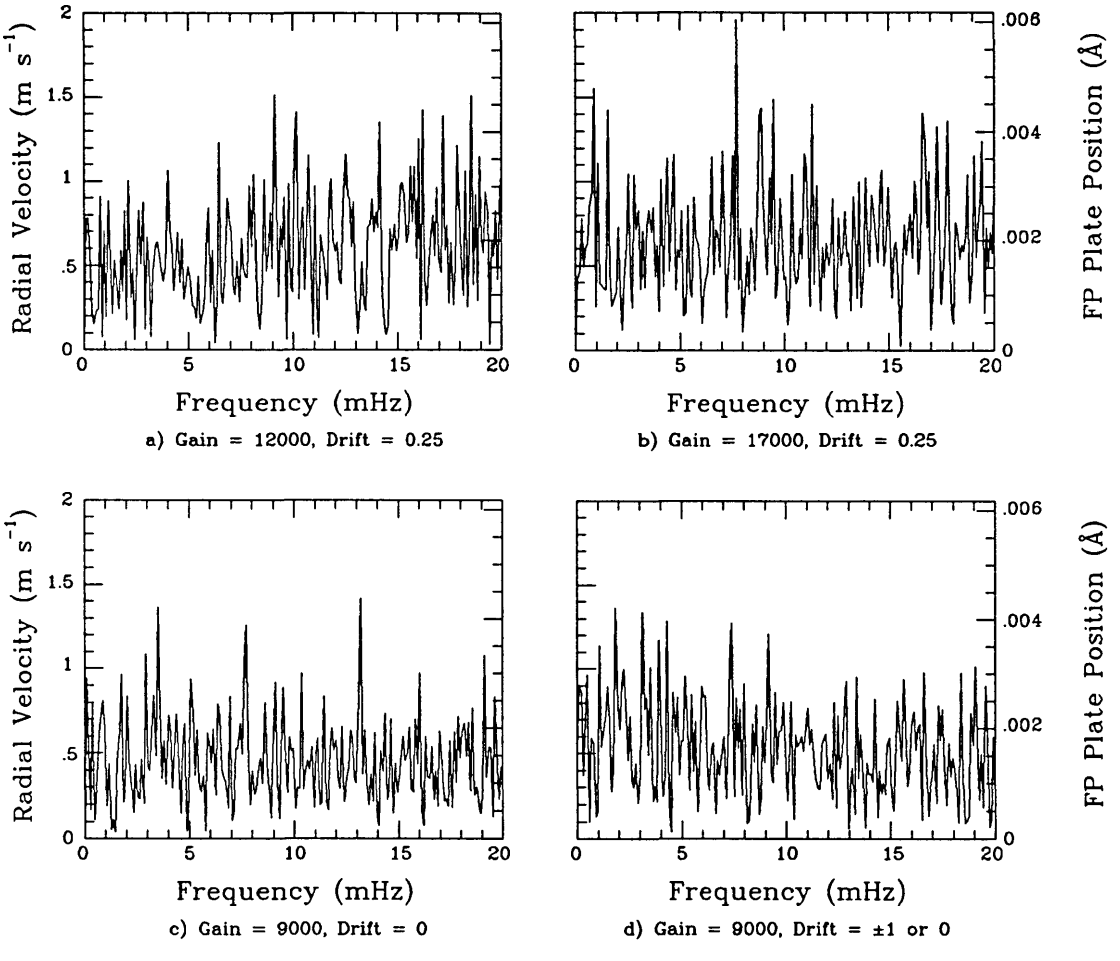


Figure 6.2: Finding the optimum gain and drift terms. A sample of the stability tests with zero chop distance. All had a 'theoretical' gain of $\approx$ 13000 and spent 1 s on the 'reference' line and 10 s on the 'stellar' line to represent the sort of time division which might be used with a star.

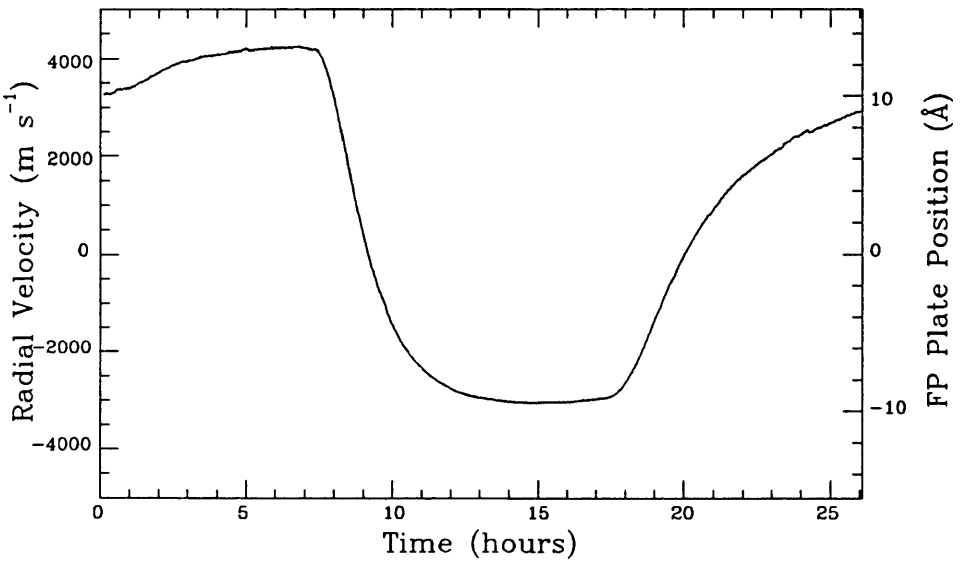


Figure 6.3: Radial velocity stability of the uninsulated etalon.

6.1.3 Radial Velocity Stability Tests

After establishing what gain to use, it was then a case of testing the offset stability of the instrument. As the stability of the interferometer was being tested, to remove problems with the lamp drifting, the cadmium blue line from the same lamp was used as both reference and 'stellar' line. To enable the offset stability to be measured, the reference was in one order and the 'stellar' line in another. Of course the *minimum* distance that the 'stellar' and reference lines could be apart is one order, whilst with two different lines, the *maximum necessary* distance apart would be half an order. This should, however, mean that it is a more exacting test of the offset stability.

Stability Without the Optical Reference

Before the offset stability could be tested, it was important to establish how the laboratory environment would affect the interferometer without any servo-control, if only to give a yardstick to measure the improvement with the reference system. For example, there was a change in the room temperature of about 2°C with a period of about fifteen hours because of the air conditioning.

Initially very little insulation was used around the etalon and pressure pot. Figure 6.3 shows the results of an over eighteen hour run on the cadmium blue line. The interfer-

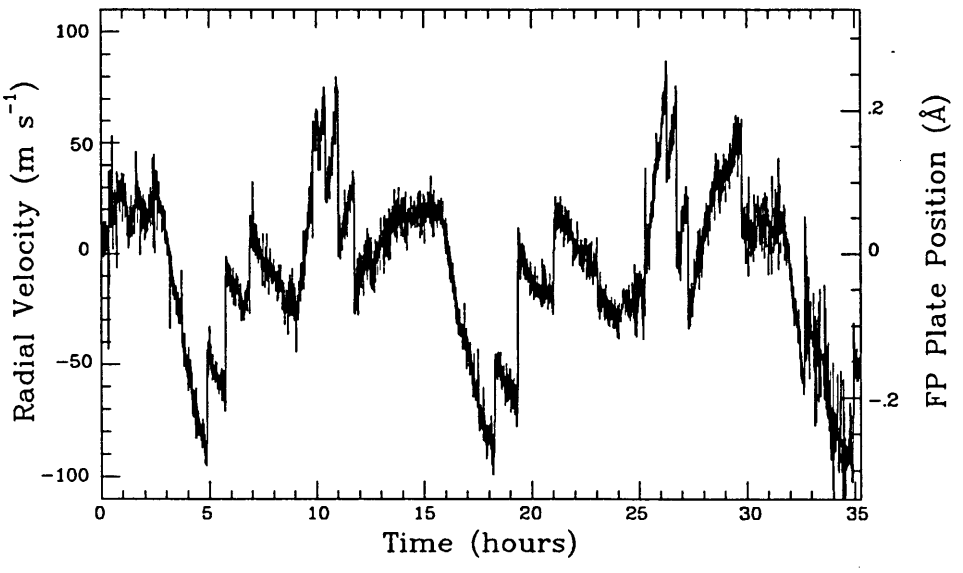


Figure 6.4: Offset stability over a 1 order chop for the uninsulated etalon.

ometer drifted by approximately 7 km s^{-1} because of an approximately 2°C change in the room temperature caused by the air conditioning. This was surprisingly large and is most probably because of the poor design of interferometer housing causing distortions with temperature.

Initial Offset stability Tests

The offset stability was tested and figure 6.4 shows the result. As can be seen, there are a lot of discontinuities. These correspond to changes in the coarse-Z position. Unfortunately the mdac's—multiplying digital to analogue converters—used have only 0.01% linearity of the full range [103]. As each step is $\approx$ 0.025% of the full range, it is possible for there to be an error of 40% of a step. Unfortunately this was not realised at the time the number of fine-Z steps to a coarse-Z step was chosen. With hindsight, it would probably have been better to choose the size of the fine-Z step so that the full range of the fine-Z would cover several coarse-Z steps. As an alternative to the above, it might be possible to use for the fine-Z control an mdac with higher resolution i.e. more bits. This would give the increased range without having to lose resolution. Note, however, that even with the problems of discontinuities when changing a coarse-Z step, the long term error has been reduced to $\approx \pm 90$ m s^{-1}.

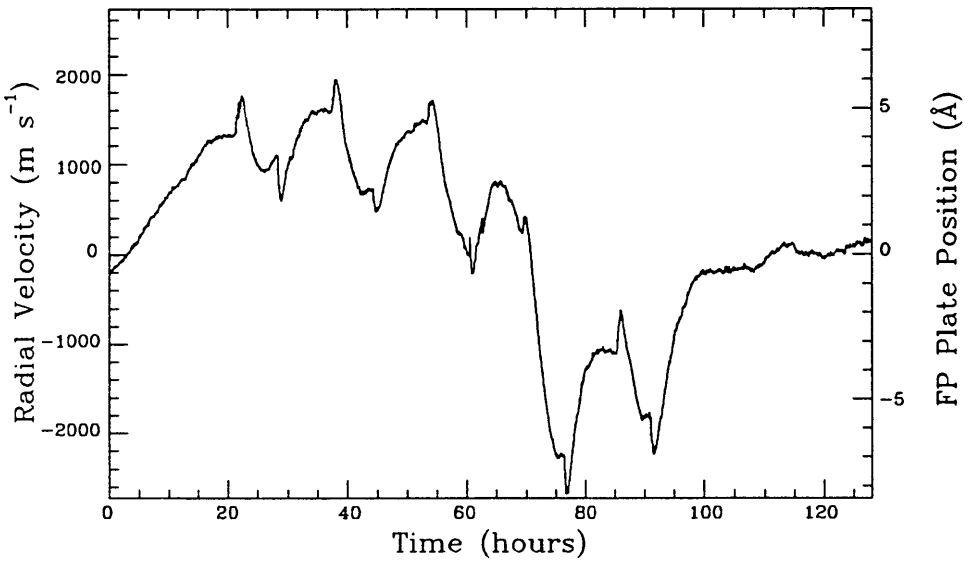


Figure 6.5: Radial velocity stability of the etalon inside the 'new' box.

6.1.4 Tests with the 'New' Box

As has been previously stated, in all the previous tests there was very little insulation around the etalon. As it was believed that the long term drifts were being caused by lack of temperature stability of the etalon and/or its housing, obviously the next thing to try was to insulate the pressure pot etc. A box was made out of 2″ thick 'styrofoam', to totally enclose the entire interferometer. To reduce the effect of convection currents inside the box, it was stuffed with scrap polystyrene blocks and packing chips. Also the electronic racks were turned round so that the draught from their fans did not affect the temperature of the interferometer. (Because of the length of the leads the interferometer had to be placed next to the CS100, and because of the lack of space, it had been placed behind two of the racks.)

Stabilty without the Optical Reference, but with the 'New' Box

Figure 6.5 shows the results with again, zero gain. This also illustrates one of the problems with the air conditioning; although it provided a useful simulation of the day/night cycle it kept being turned off, so producing a constant room temperature– which was presumably why the air conditioning was installed in the first place! The initial part of the graph is the response of the interferometer to the room temperature

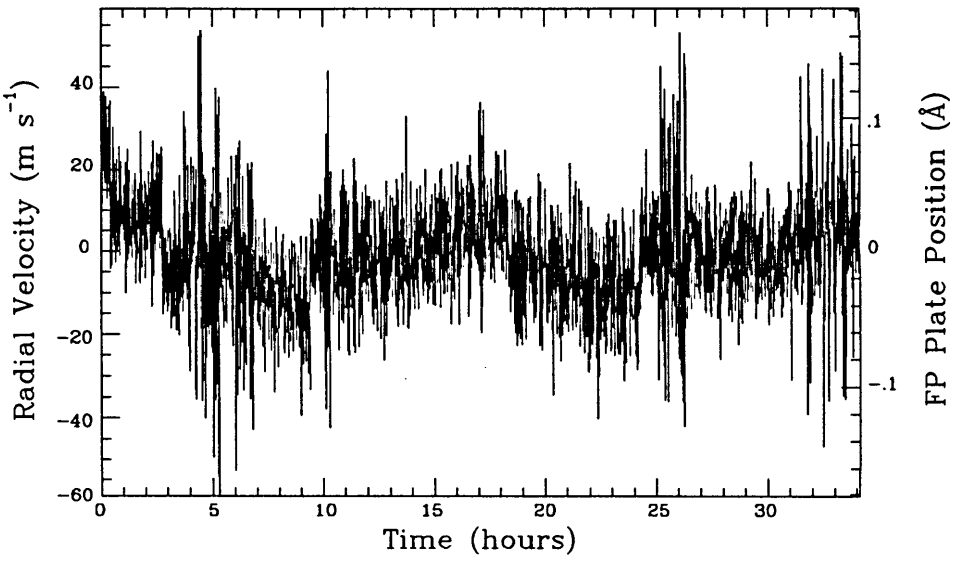


Figure 6.6: Radial velocity stability for a one order chop.

'locking' at the high end of the range. The latter part of the graph is where first the average temperature dropped, followed by the air conditioning being turned off. The wiggles in these parts of the graph are possibly caused by the temperature oscillations gradually travelling through the insulation. The structure in the middle part of the graph is very strange. It seems to be divided into two parts: an initial spike, which is coincidental with a reversal in the temperature change, and a smoother, approximately sine wave.

The initial conclusion was that the spike was being caused by temperature effects on the electronics and the smoother wave was caused by temperature effects on the interferometer through the insulation. There was always the possibility, however, that there was some effect being caused by temperature affecting the control circuit of the heater. This could then produce a distortion of the 'pot large enough to cause the apparent drift; therefore, the experiment was repeated with the heater turned off. This still gave the same sort of waveform with *possibly* higher amplitude sine wave like components, which, if this phenomenon is from the effect of temperature on the interferometer, and the temperature controller is being of any use whatsoever, is to be expected.

Offset Stability With the 'New' Box

Figure 6.6 shows the offset stability, (hence the radial velocity stability with the optical

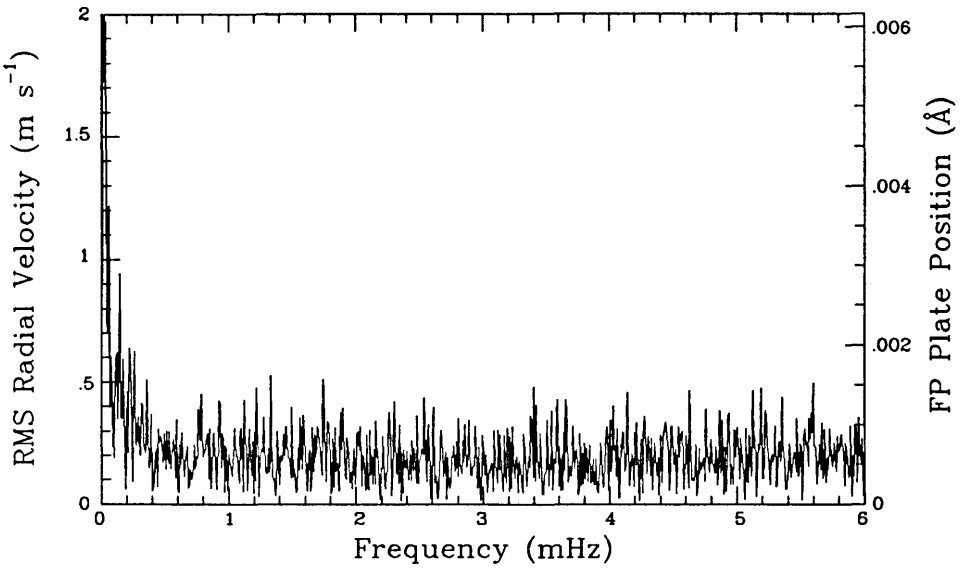


Figure 6.7: Radial velocity spectrum of figure 6.6.

reference for a one order chop), using the 'new', insulated box. As can be seen, this is a vast improvement. The temperature variations caused by the air-conditioning in the first part of the run had a smaller than normal amplitude of approximately 1°C. After the first 40 hours, however, the air-conditioning returned to its usual $\approx$ 2°C change in room temperature. Unfortunately the CS100 still cycled through two CS100 coarse-Z steps.

The radial velocity spectrum, (with the d.c. term removed), is shown in figure 6.7. The noise on the mean is less than 20 cm s^{-1} for periods of up to approximately 40 minutes, rising to $\approx$ 1 m s^{-1} by just under three hours, and with an (off-scale) maximum amplitude of just over 4 m s^{-1}. The 'white' noise part of the spectrum is from the inherent electronic noise of the CS100, whilst the '$1/f$' noise is from temperature etc. effects.

To demonstrate the hypothesis that the noise[1] increases with the size of offset, tests were done with the cadmium blue line being used as the reference line at one end of the CS100 range and as the 'stellar' line at the other end of the CS100 range. This gave a total chop size of six orders. Figures 6.8 and 6.9 show the radial velocity and the radial velocity spectrum respectively. As can be seen the drifts are higher for the six

[1]This refers to the low frequency '$1/f$' noise, the higher frequency 'white' noise should be the same for all offsets.

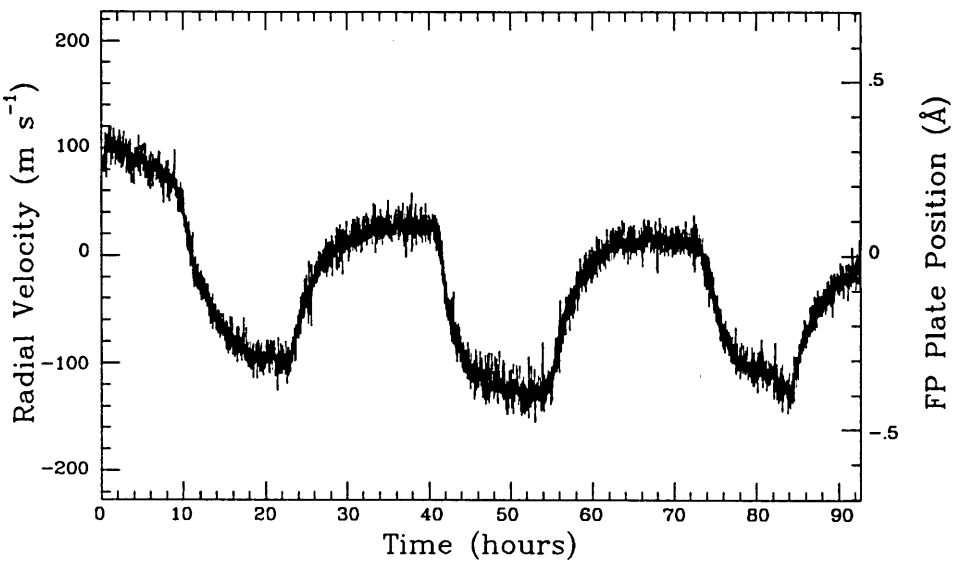


Figure 6.8: Radial velocity stability for a six order chop.

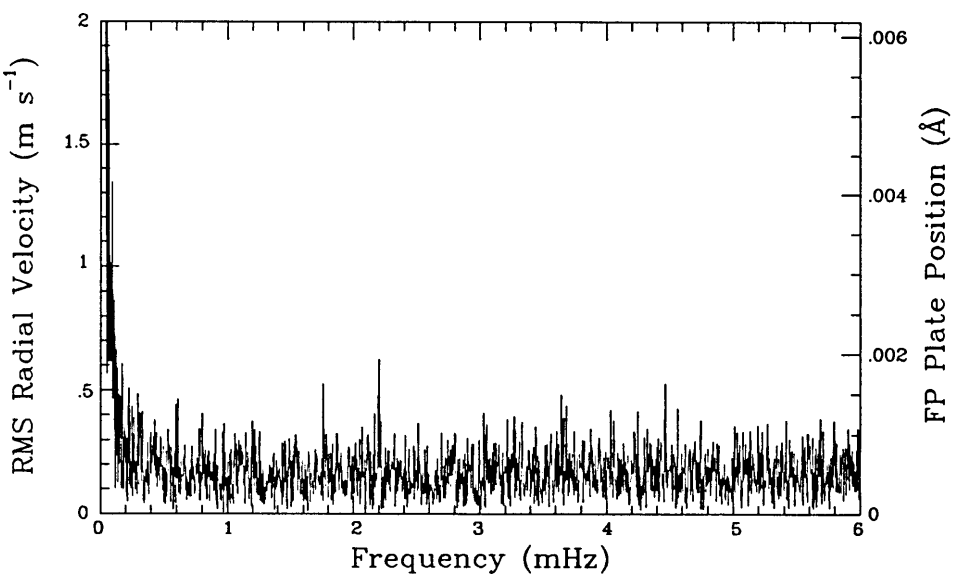


Figure 6.9: Radial velocity spectrum of figure 6.8.

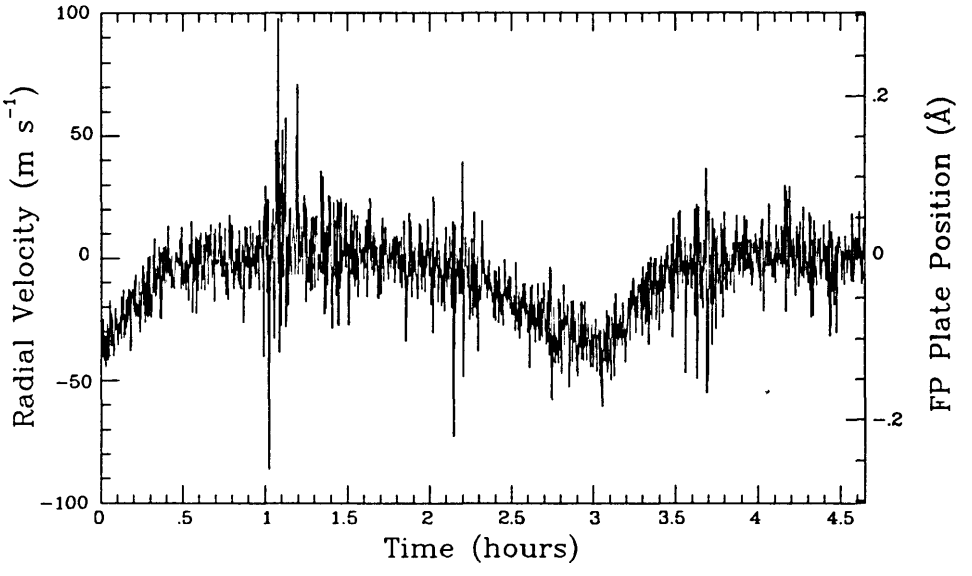


Figure 6.10: The effect of temperature on the offset electronics for a one order chop.

order chop than they are for the one order chop. In the radial velocity spectrum the low frequency terms go up to 50 m s^{-1}, (the graph having been truncated to 2 m s^{-1} to allow it to be compared to figure 6.7).

6.1.5 Effect of Temperature on the Offset Electronics

It was decided to take advantage of one of the periods when the air conditioning had been turned off to test the effect of temperature variations on the box of electronics which was responsible for the digital offset. The temperature of the offset electronics was measured by attaching a temperature probe to the outside of their box using heat sink compound. The temperature of the box was changed by putting a 'styrofoam' box over the offset module for about 90 minutes to allow it to warm up, and then taking it off for a similar time to allow it to cool down. One and a half cycles of this were done for each test.

Figure 6.10[2] shows the change in the offset for a one order chop. The change in temperature, (as measured by the temperature sensor), was about 2°C. The maximum change in radial velocity is equivalent to about ±22 m s^{-1}, which gives a radial velocity temperature coefficient of about 11 m s^{-1}°C^{-1}. The reason for the large 'glitches' after

[2]For historical reasons the tests were done in the opposite order but for aesthetical reasons they have been presented this way round. Which is why figure 6.10 starts with the temperature decreasing!

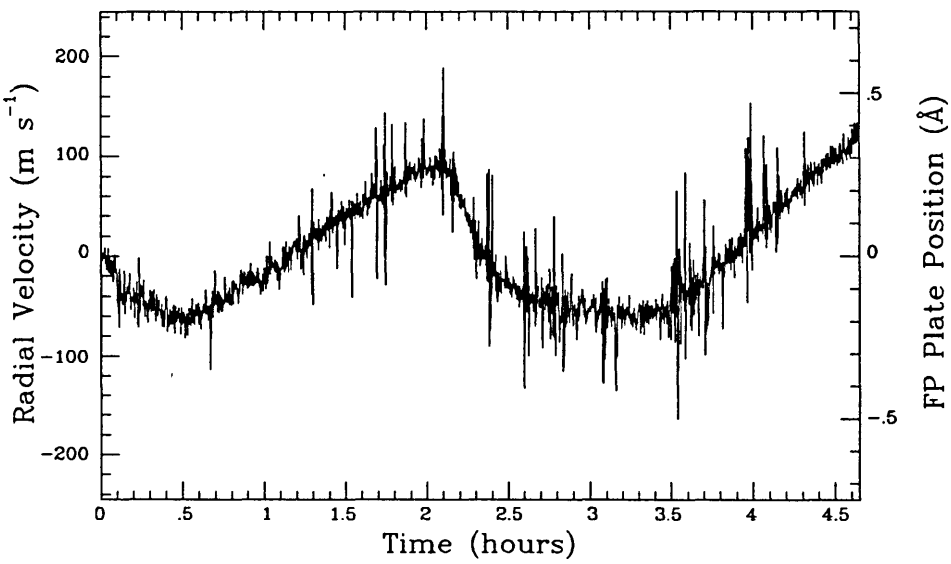


Figure 6.11: The effect of temperature on the offset electronics for a six order chop.

approximately one hour is unknown.

The effect of temperature on the electronics for a six order chop is shown in figure 6.11. There was a similar, approximately 2°C, temperature variation, giving a much larger radial velocity change of over ± 100 m s^{-1}. This is smaller than what would be expected for 6×22 m s^{-1}, the result with one order, but not drastically so.

6.2 The Echelle Pre-disperser

6.2.1 The Filter Profile

It was decided to measure the filter profile of two fibres in the echelle. This was done by making a plate to hold a fibre at the position of the mercury green line, (5461 Å). Using the stepper motor to drive the input slit, the output 'spot' of the mercury green light was scanned over a fibre mounted in the plate. (This had previously had its signal maximized by adjusting the vertical tilt of the grating.) Figure 6.12 shows the results. As can be seen from the dotted line, although the filter profile was not as good as theoretically predicted from scanning a 256×357 μm spot over a 600 μm diameter fibre, it was within 20% of it. Previously, it had been observed that the spot was bigger than expected, which could help explain the discrepancy. The input aperture was turned into a narrow slit by using two pieces of broken scalpel blades. There was

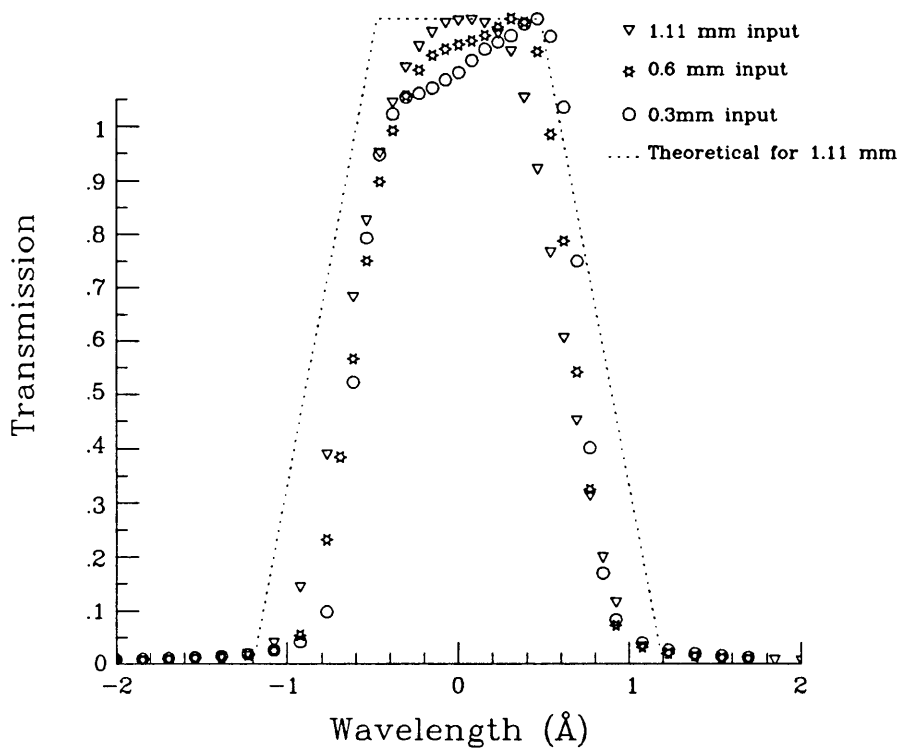


Figure 6.12: The measured filter profile of the echelle for differing slit sizes. The measurements were made using mercury green light and scanning by moving the input aperture.

no real improvement, even when a slit width of 0.1 mm, (equivalent to an image size of 26 μm), was used. For the smallest slits, however, there appeared to be 'structure' in the filter profile. This was believed to be caused by transmission variations across the fibre end and was investigated further.

(Attempts were also made to improve the image quality of the echelle. By severe readjustments, an spot size of $\approx$ 50 μm was obtainable. Unfortunately it then proved impossible to align the spectrum with the positions of the fibres on the plate. In the end, the best that could be done was to obtain a 'spot' 70×220 μm from a 100 μm input aperture. This gave with the 1.11 mm, (actually 1.17 mm), diameter input aperture an image size of 360 $\times$ 550 μm, cf. the new theoretical of 273 $\times$ 390 μm.)

Transmission Variations Across the Fibres

Figure 6.13 shows the results of scanning a $\approx$ 36 μm spot over various types of fibres. The fibres were being fed at about f2 and illuminated with mercury green light. In most cases the two scans are at right angles to one another; but in the case of figure 6.13d, the fibre was turned through 180° to test the method. (The scans have been plotted so that the direction the fibre moved across the fibre is the same in both cases.)

Possibly a large variation in transmission with the hand-cleaved fibre could be expected, (figure 4.3.2c), but with the polished ends, there was only a maximum of 15% change in transmission across the face. There appears to be very little information in the literature on transmission variations across the ends of fibres. The only information that was found is in a paper by Clayton [104], in which he images a, (presumably), f5 beam into a 140 μm spot onto the end of a 5 cm length of Quartz and Silice 400/600 AS fibre. (He was interested in investigating the image scrambling properties of short fibres.) By the time the spot had moved to $\approx$ 100μm, (scaled from his diagram), from the centre, the transmission had fallen to 0.74 of its on-axis value. Clayton had done a "very thorough" literature survey, (up until "Summer 1987"), and had found no further information. (C. A. Clayton, private communication.)

A Caveat A cleaving machine that was tried was one produced by York Technology Ltd., (and lent by the NPL). It was not designed for cleaving 600 μm fibres, so not surprisingly, it was not very successful for my purposes. They now manufacture, however, a newer version which can be modified to cleave 600 μm fibres. They offered to try and cleave a fibre. Unfortunately the fibre had "too high a quartz content" and "a

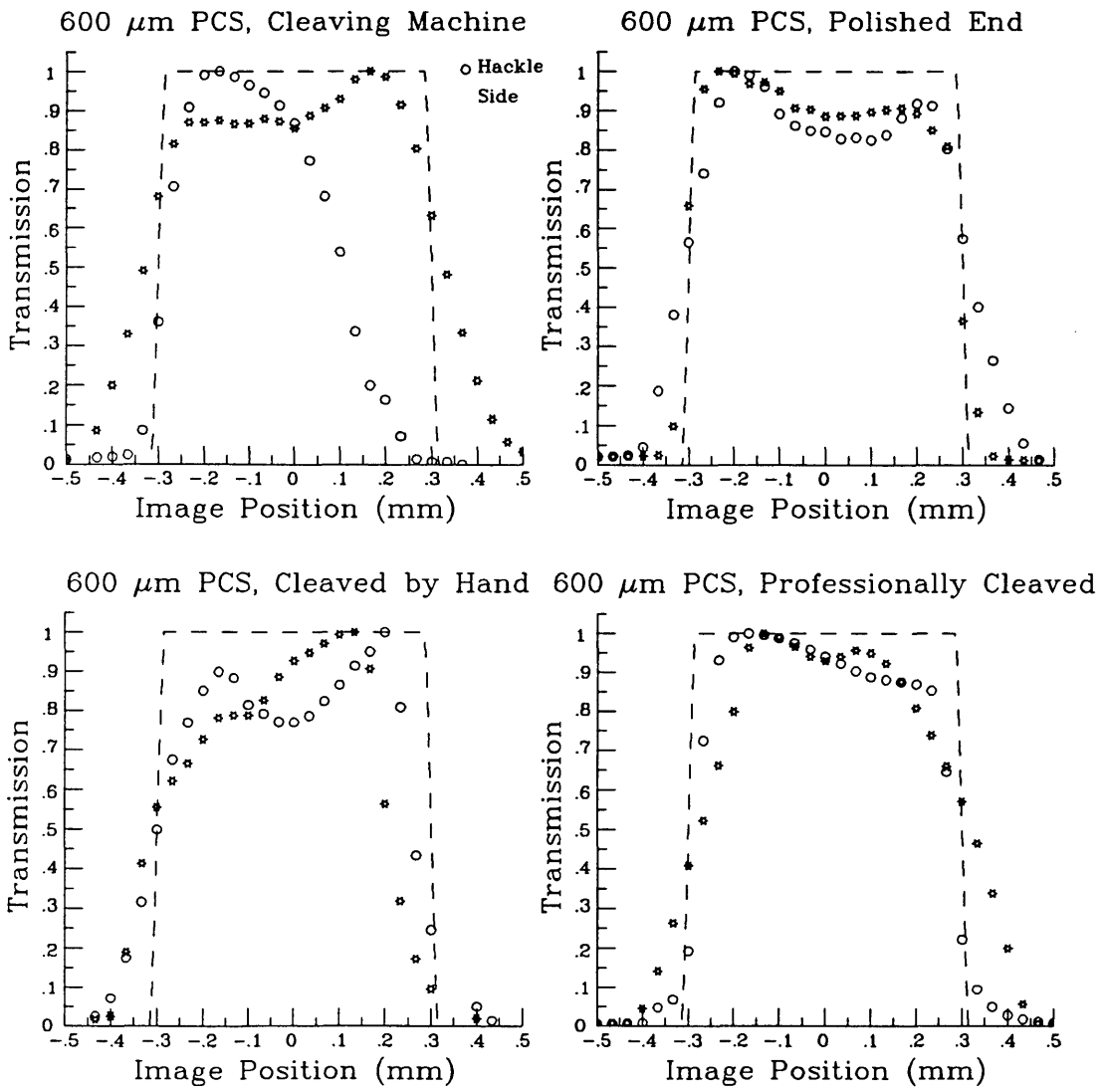


Figure 6.13: Variations in transmission with input position in optical fibres. These were made by scanning a 36 μm spot across the input.

large amount of internal stresses" which caused the fibre to "shatter" rather than cleave properly. (S. Coates[3] —private communication.) This could explain at least some of the variation in transmission with the cleaved ends.

6.2.2 Positioning Accuracy of the Optical Fibres in the echelle.

The optical fibres were assembled into the new plate, and each fibre was scanned using the Fabry-Perot Interferometer. The input aperture was adjusted, using the linear actuator, until the line appeared at the peak of the filter profile. This gave a measure of the positioning accuracy of the fibres. Ideally all the lines should appear at the peak of the filter profile for the same setting of the input aperture. Table 6.1 shows the degree of misalignment.

One step on the linear actuator was equivalent to one thousandth of an inch; i.e. approximately four steps equaled one thou' in the image plane. Obviously 'spotting through' had been an unsatisfactory method of producing the second plate. Also, the number of useable lines, with the problem of off-axis resolution, was less than had been hoped for, so the possibility of adding extra lines was looked at.

It was believed that part of the problem was that the echelle was not aligned identically to how it was when the photographic plate was originally taken. Consequently, the positions were found by using a piece of photographic film stuck to the original plate with double sided tape. The spectrum was taken, and to provide a datum, the back of the plate was 'flashed' with room light, so that the positions of the old holes were superimposed on the spectrum. The photographic film was enlarged, and the positions of the lines were measured.

Two possible methods of adjusting the position of the fibres were initially considered. The first was an optical method, using a tilted glass plate to move the line onto the fibre, (figure 6.14). The second was to use a slot drill to turn the holes into slots to correct major misalignments. Unfortunately, the 600 μm hole is much too small for this. Consequently, a new method of mounting for the extra fibres was tried.

Several different sizes of micro-tubes were obtained. The most useful appeared to be a $\frac{1}{16}''$ outer diameter, with a nominal inner diameter of $\frac{1}{32}''$. This is less than 800 μm, (the nominal diameter of the low refractive index coating), but at least one batch of fibres fitted them. Another size of micro-tubing, as well as fitting the low index

[3]Of York Technology Ltd., Chandlers Ford, Hampshire.

Table 6.1: Alignment accuracy for the fibres in the echelle with both the original and new plates. The alignment was measured by finding the positions of the input aperture necessary to centralize the filter profile with respect to the absorption lines.

Wavelength Å	Echelle Input Aperture Position (In stepper motor steps. 1 step≈ 0.016 Å)			
	New Plate	error	Original Plate	error
4602.9466	?[a]		578	0
4920.5104	542	7	573	-5
5068.7727	541	6	580	2
5133.6958	556	21	583	5
5162.2793	506	-29	572	-6
5232.9493	535	0	575	-3
5281.7979	527	-8	583	5
5324.1856	522	-13	577	-1
5339.9356	526	-9	575	-3
5367.4755	544	9	568	-10
5383.3792	539	4	588	10
5393.1744	531	-4	585	7
5400.5094	531	-4	578	0
5415.2108	557	22	588	10
5424.0764[b]	–		579	1
5446.9238[b]	–		559	-19
5569.6253	533	-2	598	20
5576.0970	?[a]		576	-2
5615.6536[b]	–		569	-9
Average σ_{n-1}	535 ± 13.3		578 ± 8.6	

[a]These lines could not be found when the measurements were being made.
[b]One of the new lines.

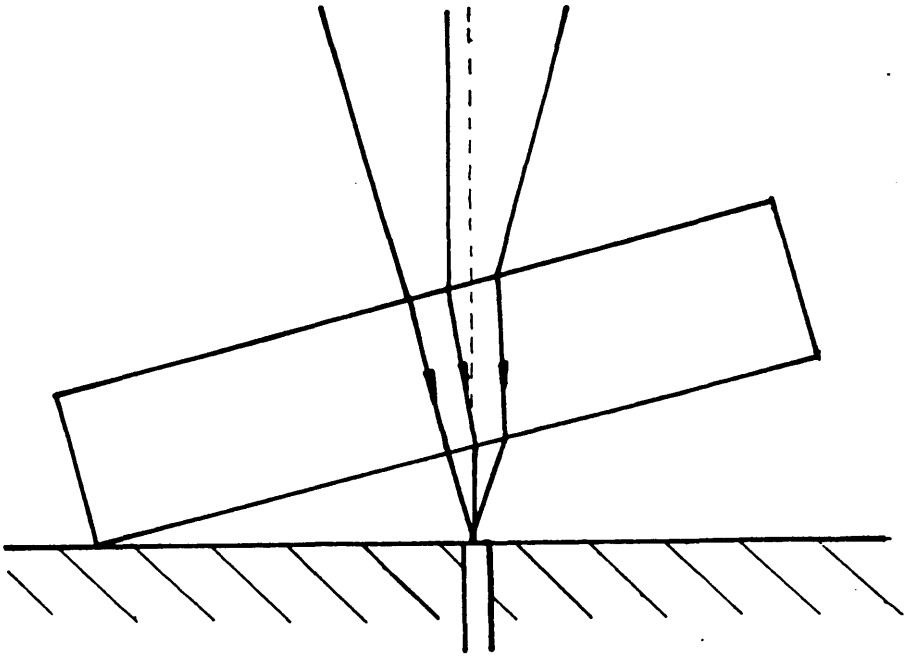


Figure 6.14: Using a glass plate to correct for misalignment in the fibres.

coating, slipped into the original tubing which was being used to support the fibres. This introduced the possibility of a two tube 'sandwich', ('telescope'?), figure 6.15, with the inner tube being used to centre the fibre in the 800 μm hole of the original plate, so preventing the low index coating being damaged. This of course meant that the original plate could be used, which it was hoped would have more accurately drilled holes.

The lines were rescanned and table 6.1 shows the results, (including the new lines). The spread of the lines is still too large but is much reduced from the previous set. Unfortunately, two of the new lines are amongst the ones that have the largest errors.

Correcting the positions using the glass plate was tried. Unfortunately, this was not very successful, with some of the lines being moved a long way for a small angle in the plate, whilst others seemed totally unaffected for quite large angles. As this seemed to be correlated with which way the fibres needed moving and which end of the plate they were at, presumably it was because the rays did not strike the plate perpendicularly. Even with the extra fibres mounted as per figure 6.15 the use of a slot drill was not tried as the feasibility of it was questionable.

As an alternative method, scalpel blades were broken up and used to adjust the position of the fibres by pushing them. The broken razor blades were then cemented in place using 'Super Glue'. Some of the fibres could not be moved far enough by this process, so the ends had to be stripped of the optical cladding. Though this method

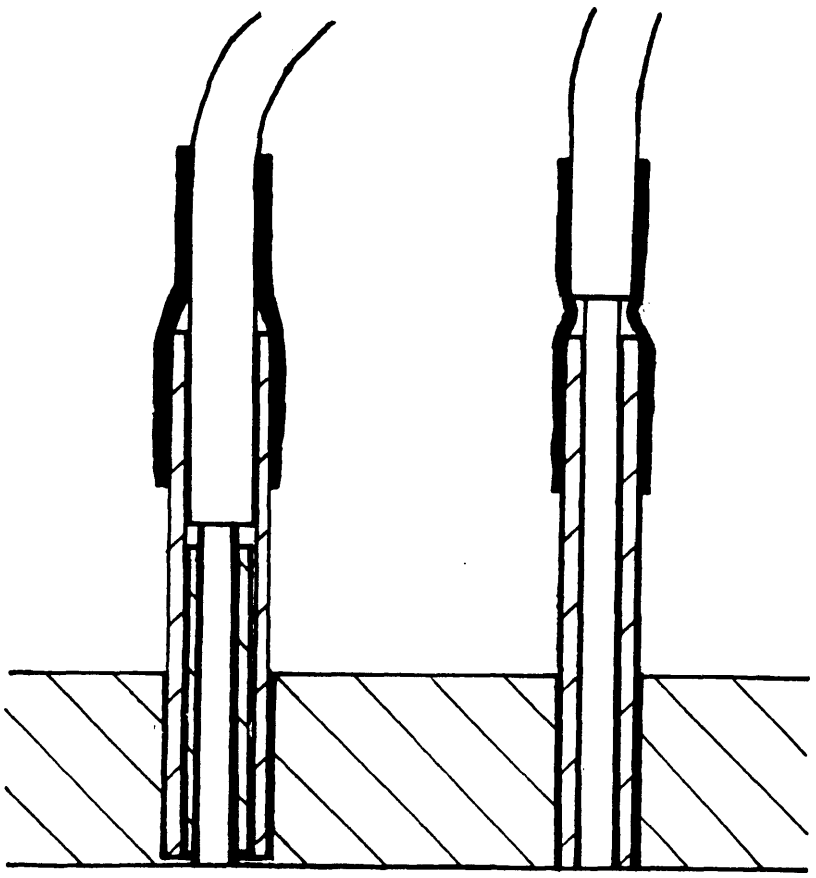


Figure 6.15: Other methods of holding the fibres.

has been relied on almost exclusively it does have problems. The main problems, (apart from fingers sticking to the plate), were the tendency for the glue to run and fill up the gaps around the fibres, plus the need for trial and error in the positioning of the fibres. The position of at least some of the fibres was not very stable. This appeared to be more from the method of holding the fibres, (they could sometimes slip in the heat-shrink), than from the method of repositioning them.

6.3 The Multi-Lined Fabry-Perot

6.3.1 Selection of the Lines

The results of the program, (see section 6.3.3), which from a given selection of lines, tried to select the largest number useable and work out their positions, had been viewed with some scepticism. So all the lines were scanned to find their line centres in CS100 steps. Then using the known size of a CS100 step, the positions of the lines, in CS100 steps, for other, (on-axis), orders were predicted. The maximum useable off-axis angle was converted into the equivalent number of on-axis CS100 steps, and the gap which had the maximum number of lines within this range searched for. This turned out to be in agreement with the previously predicted results, except it now included one of the new lines. Table 6.2 shows the results.

Because of availability, an etalon with a resolution of $\approx$ 0.37 Å was being used to measure lines of width down to $\approx$ 0.15 Å. This meant, of course, that the narrower lines were very shallow; some being less than 5% deep. As in a white light scan of the 'filter' profile, there was typically a 3% change in intensity over $\pm$ CS100 steps, the fibres needed careful alignment. Experience showed that at least some of the fibres needed to be aligned to better than half a thou'.

6.3.2 Positioning the fibres in the Fabry-Perot

Having found the best overall finesse for the etalon it was then a case of 'just' putting the lines in at the right off-axis angles. To find the best positions for the off-axis lines, the plan was to use a spring strip arrangement which had come off another instrument. This had a micrometer mounted on it to push the input slit, but to be able to cover the range necessary for my purposes, a locking screw was needed to keep the moving carriage against the micrometer. The slits were replaced by cementing, (with Araldite),

Table 6.2: Calculated positions for the useable lines with the available etalon with a gap of 93.706 μm.

Wavelength (Å)	Equivalent Width [97]	Order	Angle (degrees)	Position (mm)
5324.1856	59.5	352	0.00	0.00
5400.5094	21	347	0.71	2.49
5162.2793	31.4	363	0.84	2.95
5133.6958	30.4	365	1.06	3.68
5446.9238	42.8	344	1.14	3.98
5415.2108	37.5	346	1.27	4.43
5576.0970	21.9	336	1.39	4.84
5383.3792	36	348	1.56	5.45
4602.9466	22.2	407	1.59	5.54
5232.9493	64.9	358	1.61	5.62
5367.4755	29.1	349	1.74	6.06

an aluminium block onto the moving carriage, with a $\frac{1}{16}''$ diameter hole to take the $\frac{1}{16}''$ o.d.$\times\frac{1}{32}''$ i.d. micro-tubing. To locate it, the spring strip arrangement had been fitted with two $\frac{1}{8}''$ dowels. Pairs of dowel holes had previously been drilled in the end of the interferometer housing at 30° intervals to match. The idea was to be able to put the spring strip arrangement in the selected pair of dowel holes, slip the micro-tubing into the hole, and then while holding the fibres in the micro-tubing, scan until the correct position was reached, and record the micrometer reading. This was done for the on-axis 'master' fibre by finding the position at which the scan went to minimum CS100 steps, (i.e. maximum wavelength), and for the others by aligning their line profiles with the known position of the that of the on-axis 'master' fibre. When all the required fibre positions had been found, (the pairs of dowel holes at 30° intervals allowed the fibres to be fitted in a two dimensional (polar) array), the spring strip apparatus was to be put on the fibre mounting plate, which also had the corresponding dowel holes in it, the micro-tube removed, so allowing the position of the fibres, (found by setting the micrometer), to be spotted through. Depending on the amount of space for the fibres, either a hole of $\frac{1}{16}''$ or 1.08 mm diameter was drilled for the corresponding diameter micro-tube.

When this was tried with the 11 lines it was found to be nearly impossible to find

Table 6.3: Lines successfully used with the Fabry-Perot.

Wavelength (Å)	Predicted Position (mm)	Actual position (mm)
5162.2793	0.51	0
5615.6536	2.06	1.25
5133.6958	0	-0.95
5339.9356	–	3.75[a]
5324.1856	4.40	4.70
5232.9493	5.88	6.20

[a]This line was positioned on the next set of dowel holes at an angle of 30° and consequently, because of the method of measuring, this is only an approximation

the further out narrower off-axis lines. Even some of those quite close in were only $\lesssim$ 1.5% deep!

Another attempt at selecting lines was made, this time restricting the resolution to 0.4 Å and only selecting from the best 12 lines. This found an arrangement of five lines. Again, unfortunately, the most marginal candidate, (5415 Å), turned out to be virtually undetectable. Restricting the choice to the best six only gave selections with three lines in them. By relaxing the tolerance on the resolution to 0.5 Å, and selecting from the best eight, led to the program giving several selections of five lines, table 6.3. One in particular looked very hopeful, with the second, (5232.9 Å), and third, (5324 Å), widest lines being the furthest and second furthest out, respectively. Scanning the lines at their expected positions showed the shallowest depth to be 5.8%,[4] (for the 5232.9 Å line), which was hopeful.

As a variation, the on-axis position for the 'master' fibre was found by chopping on the nominal half maxima points and adjusting the position of the fibre until the ratio became smallest, (or most negative). Having established the position of the first line, which as can be seen from table 6.3 turned out to be 5162.3 Å, not the predicted 5133.7 Å, all the other lines were aligned with it. The lines were aligned on their individual best echelle input slit positions, which usually turned out to be different from the 'average' best echelle input slit position, with the intention to correct the (echelle) fibre positions afterwards. Some of the lines were slightly asymmetric, so the

[4]This was improved later by fine adjustment of the finesse.

fibres were positioned by finding the central twenty points, (so that the 'shoulders' were of equal heights), for the on-axis 5162.3 Å and adjusting the positions of the other lines until their 'shoulders' also matched, (table 6.3). 5339.9 Å was not in the original choice of lines, but the second program, (see section 6.3.1), had predicted that it would be in between the positions of 5133.7 Å and 5324.2 Å, so it was decided to try it. Though a little shallow, being 5% deep, it was included.

6.3.3 Line Profile Scans

Single Lines

Figure 6.16 shows scans of the selected lines at the best echelle position, (within the resolution of the linear actuator), working from the inner most outwards. The first column shows the on-axis scan, (or at least the hole used for the 5162.3 Å line), whilst the second column shows the scan for the fibre in the 'correct' off-axis position with the y-axis of the plots having the same proportions as the on-axis position to enable a comparison to be made. The first thing to be noticed is the rapid decrease in line depth[5] with increasing off-axis angle, particularly for the outer three lines, and especially in the case of 5232.9 Å, which goes from being nearly 30% deep to less than 10% deep. This was because of the use of an over generous tolerance for loss of resolution for off-axis angles, (0.5 Å, cf. $\approx$ 0.37 Å for the resolution of the on-axis etalon). The 5324.2 Å line was just inside the limit for a 0.37 Å loss of resolution. The other thing that is noticeable is the drop in count rate with increasing off-axis positions, (the low counts for 5162.3 Å are because it was on the edge of the output field of the echelle). Some vignetting was expected, but this seemed to be far worse. The output photomultiplier was removed and the brightness of the output 'spots' inspected by eye. They all seemed to be of approximately the same brightness. Consequently variations in the sensitivity across the photocathode was suspected.

Sensitivity variations across the photocathode

A 600 μm fibre, illuminated by cadmium blue light, was imaged onto the photomultiplier and scanned by moving the photomultiplier along an optical bench The results are shown

[5]Although in the matched filter theorem for optimal results, the line and filter widths are comparable, leading to a much reduced resultant line depth, in this case as the 'filter' is wider than optimum for all of the lines, the decreasing line depth provides a measure of the mismatch.

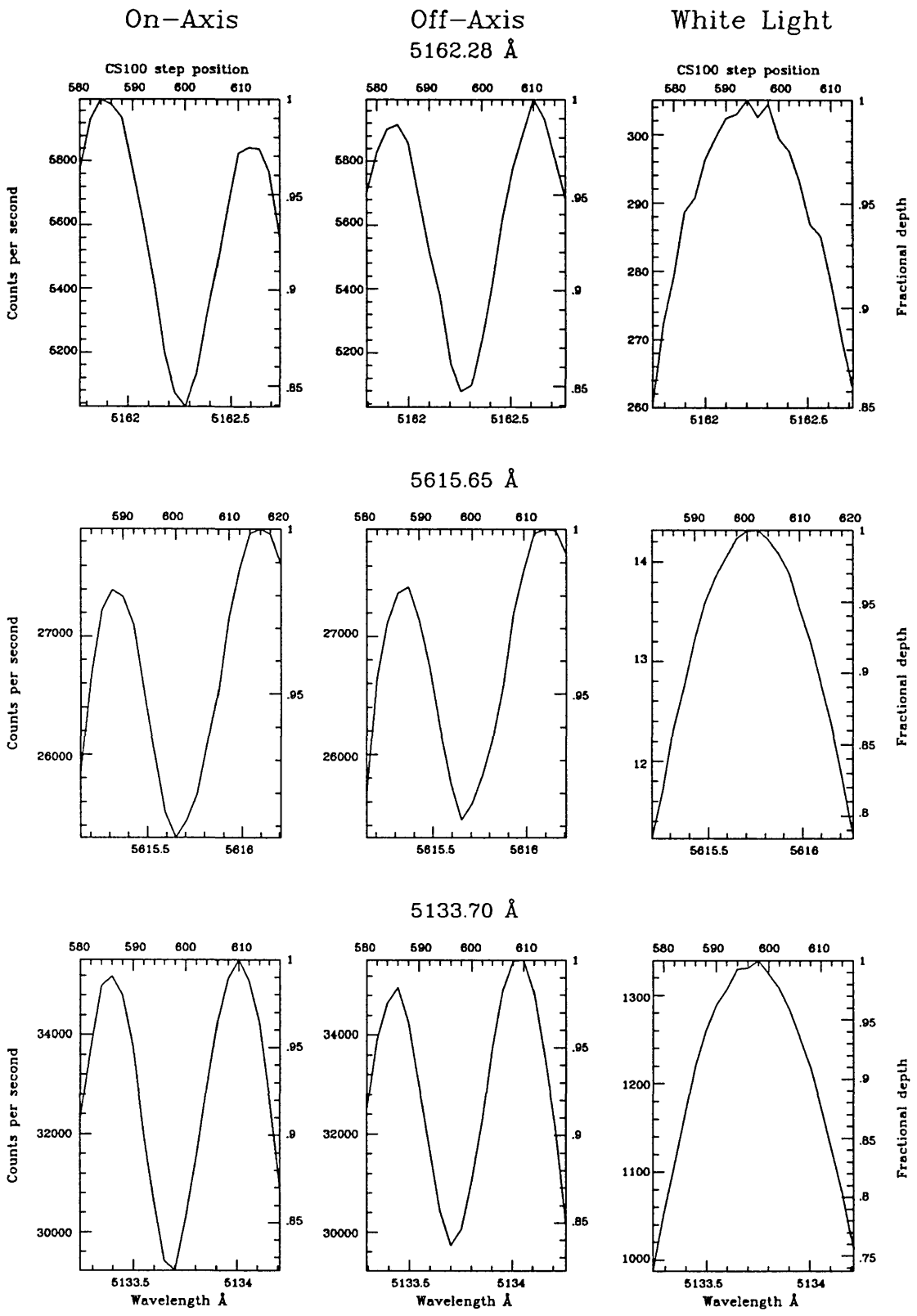
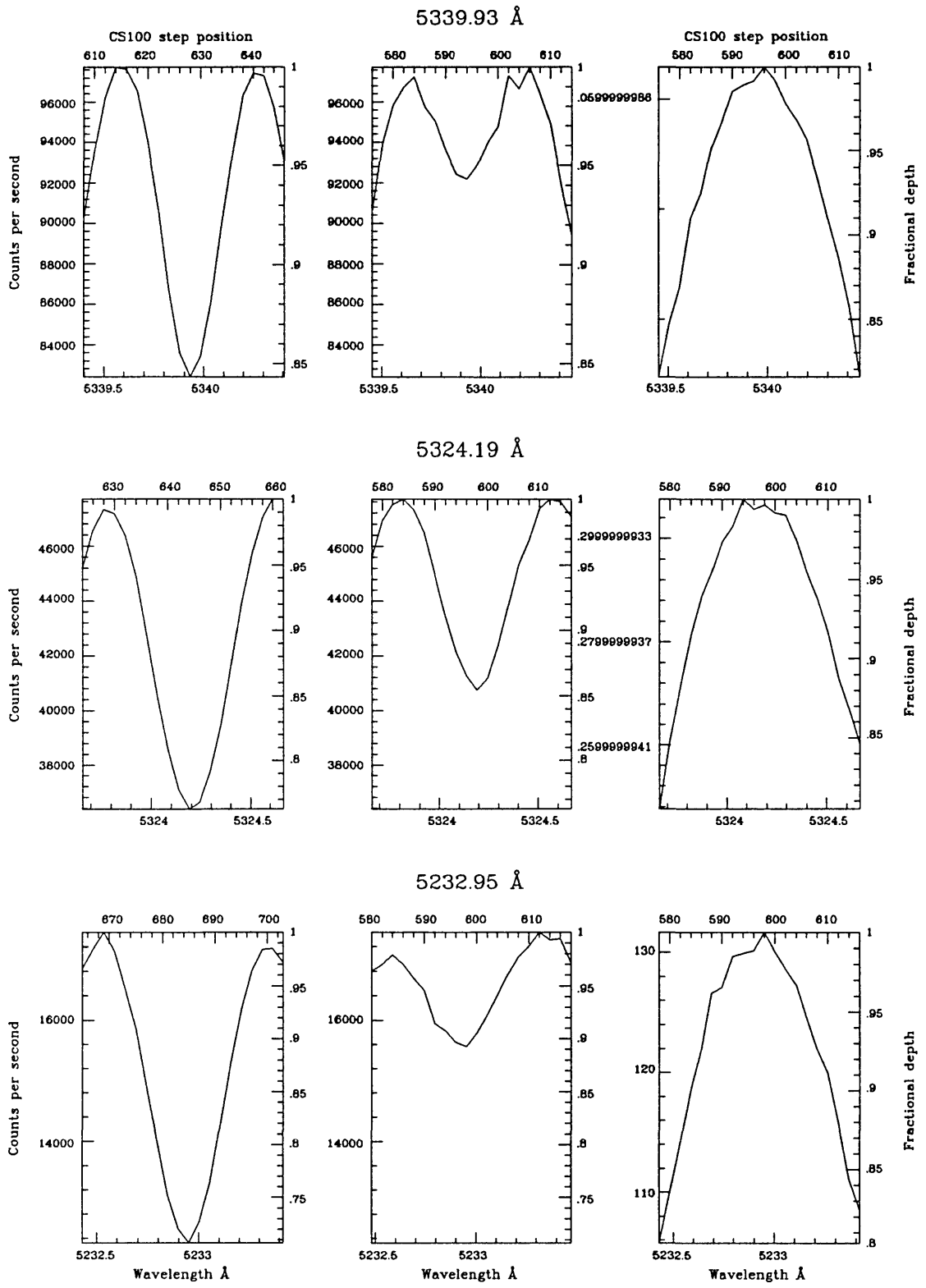


Figure 6.16: Scans of the on and off-axis line profiles, plus the filter profiles, of the lines eventually used.

Figure 6.16 continued.



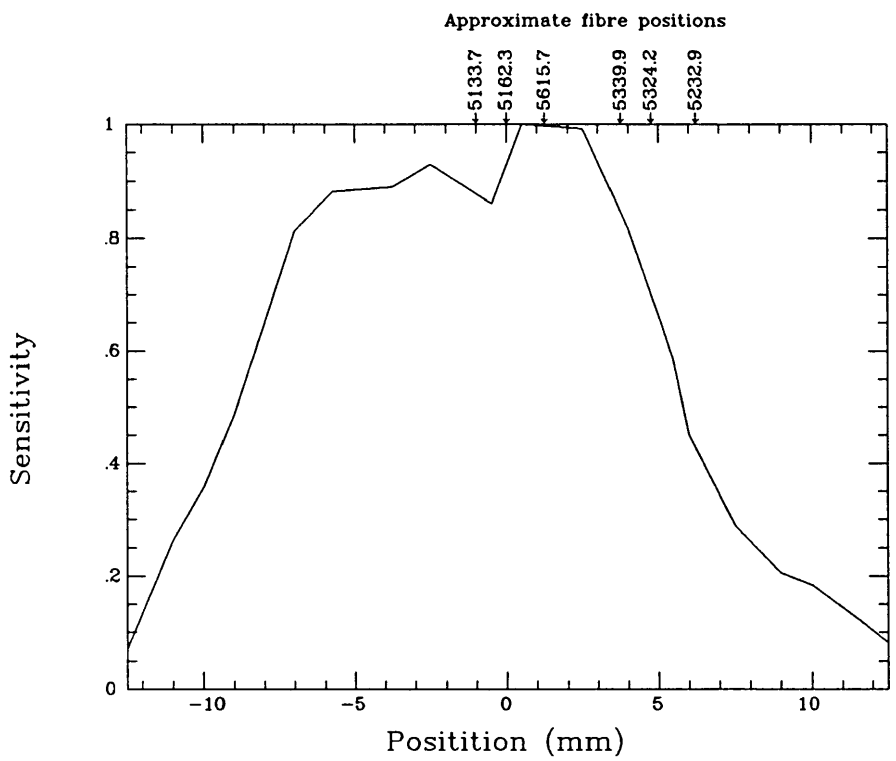


Figure 6.17: Sensitivity variations in the E.M.I. side window photocathode

in figure 6.17. As can be seen, the counts drop by 20% in $+3.5 - 6.5$ mm and fall off rapidly after that. It is not known precisely where the images of the fibres were falling, but at least the outer fibres were probably in the low count rate area. Obviously, this is somewhat unsatisfactory, however, this is possibly particular to this type of photomultiplier, apparently, changes of 20% are more usual across the photocathode, (T. J. Norton—private communication).

Unfortunately, this does not explain all the discrepancy between the on and off-axis count rates. Some of it could be from deteriorating weather affecting the intensity, some must be from vignetting and some may even be from deposits of bits of the fibre cladding on the field lens!

The third column of figure 6.16 shows white light scans of the off-axis fibres.

The Multi-Line Line Profile

Having had the plate drilled to take the fibres, it was then necessary to re-adjust the echelle-end fibre positions to try and arrange for the lines to be centred on top of the filter profiles at the same time. Figure 6.18 shows the results. All the lines have been scanned over the same CS100 range. The three 'scans' at the bottom of figure 6.18 show the multi-lined scan. The central one is the measured result, produced by putting all the lines in and scanning them simultaneously. On its left, for comparison, is all the above lines summed. The right hand 'scan' was produced by summing all the off-axis column scans from figure 6.16, which are at their best echelle positions and were 'aligned', (in the computer), to give the maximum line depth. The difference between the 'summed' and the 'scanned' is possibly caused by the effects of clouds. Ignoring the different count rates, (which are, at least to some extent because of the weather), there is not too much difference between the actual measured and the most nearly optimal result possible for the present set-up, (though, of course, the optimum was again vulnerable to the effect of clouds).

6.3.4 Improvement in Signal-to-Noise.

Of course using multiple lines increases the number of photons, and hence, the signal-to-noise. Unfortunately, it also leads to a degradation in the line profile, leading to a loss of sensitivity to radial velocity changes, compared with using single lines. The question is though, can the increase in photons offset the loss of sensitivity due to a degradation

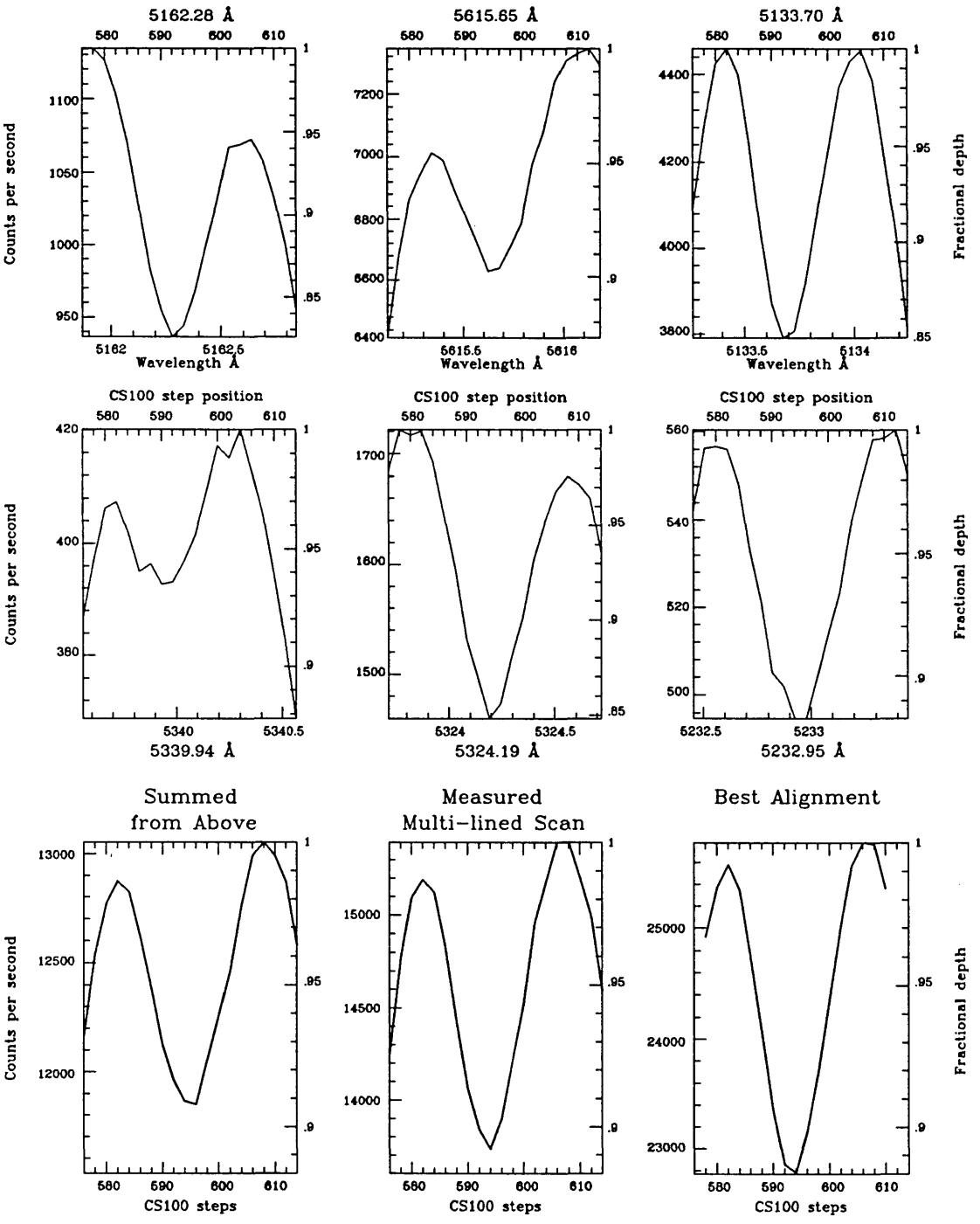


Figure 6.18: Addition of the lines. The top two rows show the individual lines scanned over the same CS100 range and at the same echelle position. The first scan in the bottom row is the summation of the above individual lines, the next is the actual scan of the multi-lined Fabry-Perot, and the final one is the optimum summation of the lines from figure 6.16.

Table 6.4: Radial velocity sensitivity of the Fabry-Perot.

Wavelength Å.	On-Axis			Off-Axis		
	Counts (kHz).	Change in ratio for 1 step.	Radial velocity in 1 sec ($m\,s^{-1}$).	Counts (kHz).	Change in ratio for 1 step.	Radial velocity in 1 sec ($m\,s^{-1}$).
5162	142	0.0171	237	62	0.0137	450
5615	310	0.0102	248	416	0.0086	254
5133	304	0.0241	116	250	0.0175	176
5339	422	0.0201	113	24	0.0016	6080
5324	366	0.0265	92	97	0.0158	301
5233	278	0.0313	91	32	0.0126	669
All lines[a]				750	0.0101	170

[a]Calculated using an average wavelength of 5300 Å.

in the line profile; and if so, has this project demonstrated it?

Table 6.4 shows the radial velocity that was measured in one second for both the on and off-axis positions of the fibres. It also shows the the radial velocity that was obtained using multiple lines. As can be seen, whilst the result was (just) better than that from any of the off-axis fibres, it was not as good as that obtained with most of the on-axis fibres. However, as has been previously stated, the present set up is far from the ideal, especially for the Sun. It has several, probably solvable, defects which makes the comparison unfair.

Differing count rates for the different lines makes it difficult to make a fair comparison with the multi-line case. They occur because of the change in efficiency of the echelle blaze with angle and (probably) differing fibre transmissions. Obviously, as a blazed grating will almost inevitably have to be used, the first problem is insurmountable, whilst the second is possibly a case of treating the fibres with more respect! As well as the above, there is the variation in transmission of the interferometer with off-axis angle. Some of this is from using a Fabry-Perot off-axis, but most is from variations in sensitivity across the photomultiplier and vignetting in the optics.

It should be possible to 'design-out' the latter two problems. Summing the individual count rates for the line would lead to an improvement in the signal to noise from 170 to 118 $m\,s^{-1}$ in one second. (This has ignored the potential worsening of the line profile because of the increased contribution of the outer lines.)

Table 6.5: Comparison of the sensitivity of the multi-lined Fabry-Perot. The average and 'summed' results are from the maximum values for the individual lines.

	Counts (kHz).	Change in Ratio for 1 Step.	Radial Velocity in 1 sec ($m\,s^{-1}$).
Best on-axis line (5233 Å)	278	0.0313	91
Average on-axis line	304	0.0219	123
Summing all on-axis lines	1822	0.0219	50
Average off-axis line	147	0.0122	318
Summing all off-axis line	881	0.0122	130
Experimental Results	750	0.0101	170

Still, the biggest source of the apparent loss of sensitivity, however, is the Fabry-Perot not being matched to the Solar line widths. The 5232.9 Å line is by far the best, (at least as far as sensitivity is concerned), as it is the broadest,[6] and hence, the most nearly resolved. Consequently the *present* multi-lined Fabry-Perot comes off worse in any comparison with this line, (though this is probably the most obvious comparison), because of, at least to some extent, the presence of all the other much less well matched lines, and not from any inherent problems with the technique. If the current etalon was more nearly matched to the lines, (or visa-versa), then this would have much less of an effect.

Possibly it would be fairer to compare the sensitivity to radial velocity of the multi-lined etalon with the *average* sensitivities of all the lines. Table 6.5 gives the change in ratio for one CS100 step for the average on-axis line and that actually achieved. As the 'average' single line has approximately twice the sensitivity as the multi-lined 'line', four times the flux would be needed with multiple lines before the signal-to-noise ratios would be the same.

Table 6.5 also shows the results of summing the individual off-axis lines. Note that the change in ratio for one CS100 step so produced is only 1.2 times larger than that which was actually attained. The highest count rate lines were closest to the centre, (because of lack of vignetting etc.), hence they were less affected by misalignment. On the other hand the sensitivity would be reduced because of the different line widths; the maximum slope for the individual lines occur at different distances from the line

[6]Generally, for *resolved* lines of equal depth, narrow is better. It is only in the case of *unresolved* lines that broader lines have the advantage.

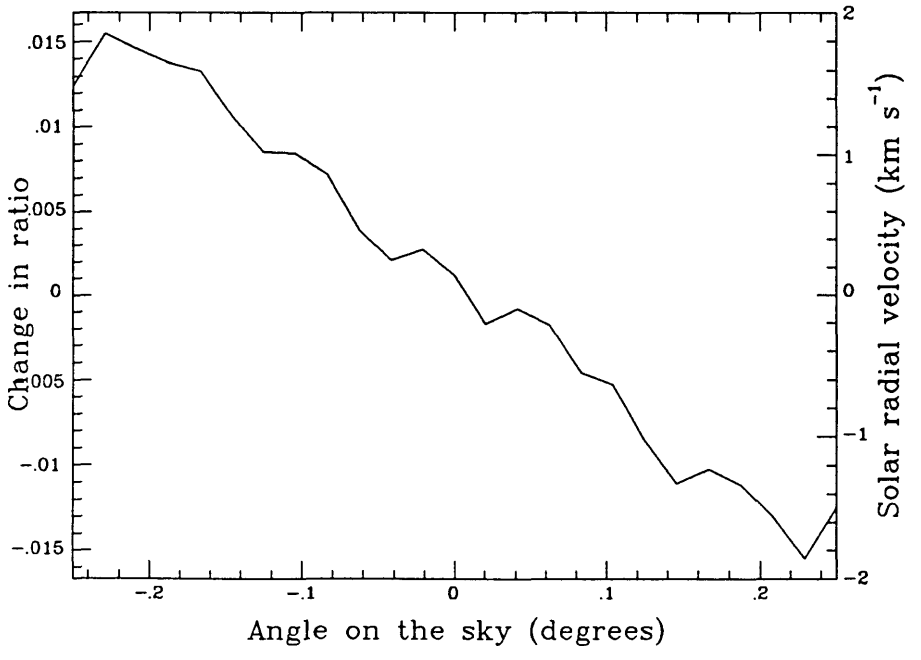


Figure 6.19: Drifts across the Sun showing the Solar rotation. These were obtained by stopping the drive on a telescope and allowing the rotation of the Earth to carry the Sun across the fibre. The Sun's rotational velocity should be 1350 m s^{-1}.

centres.

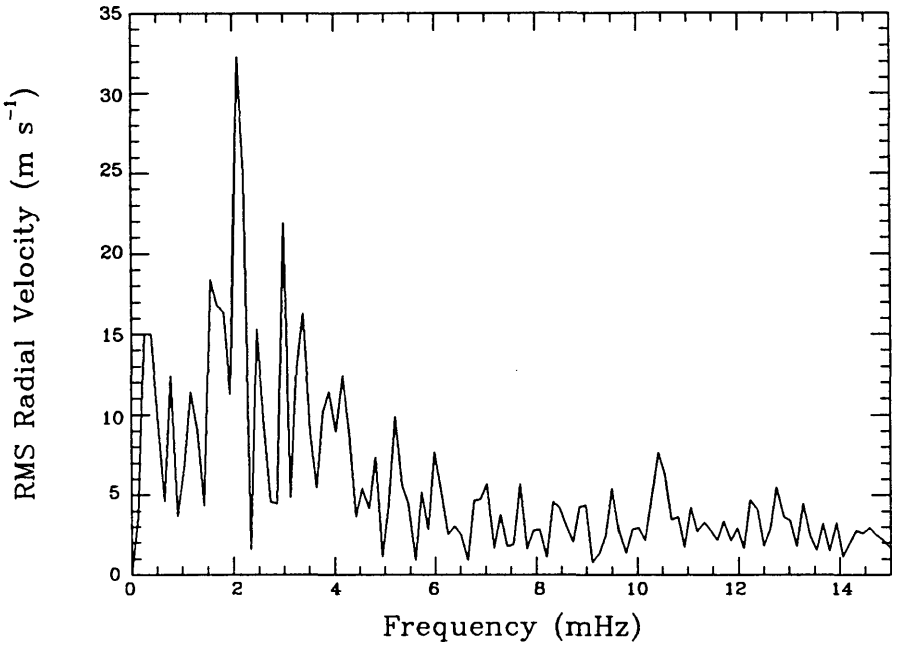
6.3.5 Radial Velocity Measurements on the Sun

Previously, all the stability tests with the instrument had been done on a single emission line from a cadmium lamp. By using the sun as a source of radial velocity variations, some idea of the performance of the multi-lined Fabry-Perot on a star can be gained.

With the particular etalon gap being used, the interferometer is incapable of detecting the 15 cm s^{-1} r.m.s. signal from the 'Sun as a star' because of the white noise from the CS100. Fortunately there are other, larger amplitude signals available from the Sun.

Detection of the Sun's Rotation

With its radius of 6.96 x 10^8 m and rotational period with respect to the Earth of $\approx$ 27.28 days [105, page 75], it has a change in radial velocity of $\approx$ 3711 m s^{-1} across its diameter. Figure 6.19 shows the result of several scans across the Sun. They were



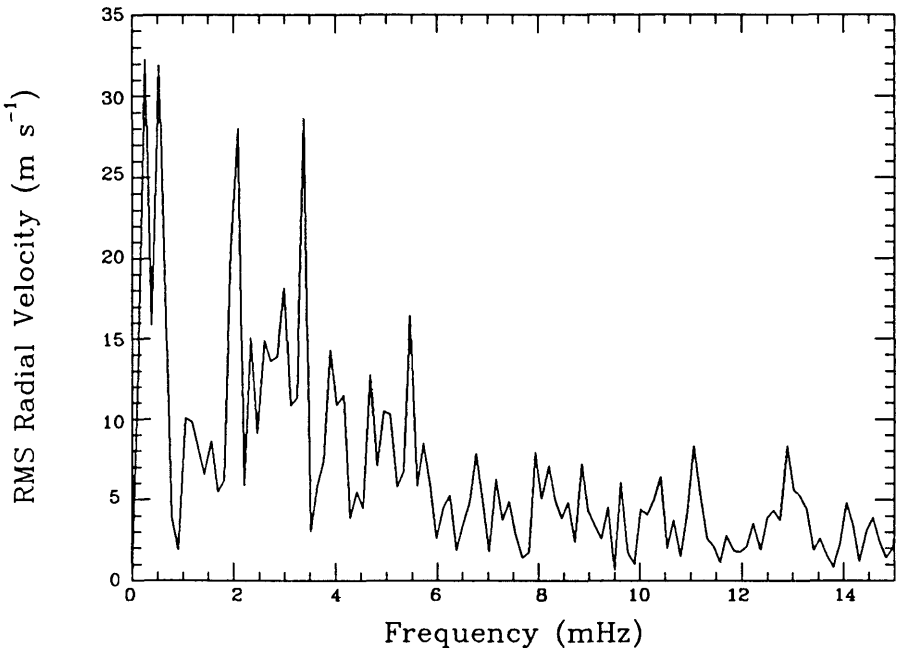
See Appendix B, p153

Figure 6.20: Five minute oscillation from a small part of the Sun's surface (128 points at 30s/point).

all taken by switching off the drive to the telescope and letting the Sun drift through the position of the fibre. Possibly the best use for these is as a calibration for the radial velocity sensitivity of the interferometer. This seems to be somewhat more sensitive than that calculated from knowing the change in ratio per step, ($\approx$ 106000 m s^{-1} cf $\approx$ 147500 m s^{-1} typically), though this could be because of departures from linearity of the ratio over the $\approx \pm 0.03$ Å change in wavelength, (plus possible limb affects).

The 5-Minute Oscillation from Part of the Sun (See also Appendix B)

Whilst the individual modes have r.m.s. velocities of less than 15 cm s^{-1}, over small areas many modes can add together to give much larger velocities. By imaging part of the Sun, using a small telescope, onto the fibre, it was possible to detect these. Figures 6.20 and 6.21 give examples of the detection of the five minute oscillation at the approximately 10–20 m s^{-1} level. The noise in both cases is about 2.5 m s^{-1}. This is within agreement with that which would be predicted from the count rate, (which would give $\approx$ 2 m s^{-1}), the slight discrepancy could be because of noise from surface features on the Sun. The long term linear drift in both cases was $\approx$ 100 m s^{-1}, (this



See Appendix B, p 153

Figure 6.21: Five minute oscillation from a small part of the Sun's surface (256 points at 30s/point).

was removed before taking the Fourier transforms).

6.4 Multi-Lining the Michelson[7]

After some initial tests on adding the cadmium blue and green and the mercury green lines, to show the beating of multiple line fringes, (figure 6.22 and [106]), the Michelson was tested using lines from the echelle. The Michelson was designed for use with linewidths typical of the Sun. Consequently, it apparently had difficulty detecting the wider lines; no fringes being found for the three widest: 5324.2, 5232.9 and 4920.5 Å, plus the 4602.9 Å line.

As was described in chapter 5, the fibres were held in an array of previously drilled holes in a plate. The lines were scanned on-axis and their approximate phases measured to give an estimate of the best off-axis positions. 5281.8 Å was chosen as the on-axis, 'master' fibre. Table 6.6 shows the fringe depths for the various lines, both on-axis and at the correct off-axis distance along with the 'master' fibre. It also gives the off-axis

[7]The following results were obtained by Dr. K.A.R.B. Pietraszewski, using the Michelson plus echelle as described above.

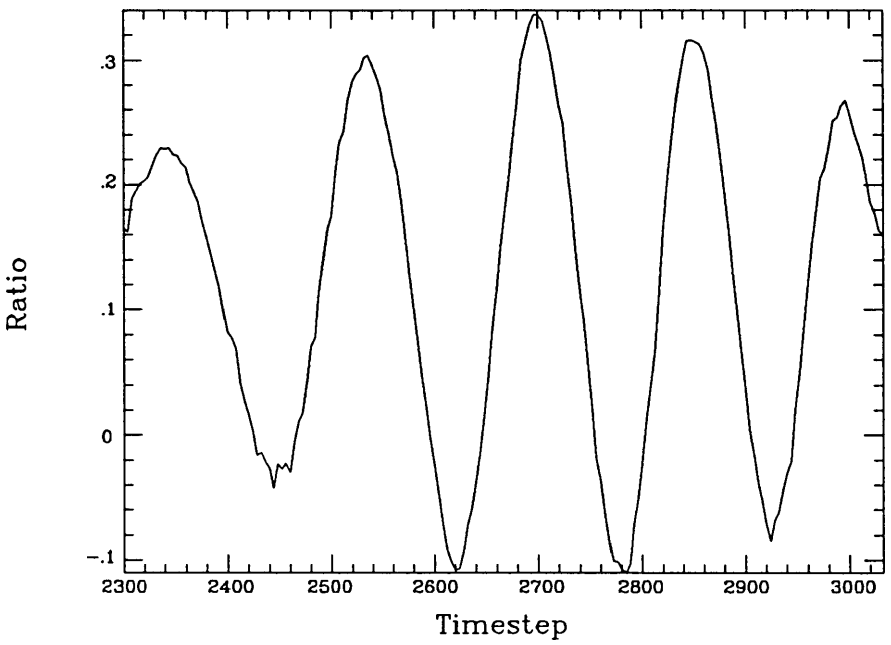


Figure 6.22: Beating of the cadmium blue and green and mercury green lines in the Michelson *ISOS*.

Table 6.6: Lines used with the multi-lined Michelson.

Wavelength Å	Equivalent Width [97]	Fringe Depth	Depth +5281.8 Å	Off-Axis Position (mm)
5576.0970	21.9	0.018	0.015	-1.5
5068.7727	25.4	0.022	0.015	-1.1
5281.7979[a]	36	0.02	–	0.0
5133.6958[a]	30.1	0.023	0.019	0.4
5367.4755	27.2	0.025	0.015	1.0
5415.2108[a]	21.9	0.020	0.019	2.1
5393.1744[a]	37.5	0.020	0.018	2.1
5383.3792	21	0.020	0.020	3.9
5400.5094	30.3	0.020	0.014	4.6
Multi-lined	–	0.012	–	–

[a]Used in the four line tests.

Table 6.7: Improvement in sensitivity of the multi-lined Michelson compared to the single (5281.8 Å) lined case.

Number of Lines	Fringe Depth	Relative Sensitivity	Counts (kHz)	Improvement in Sensitivity
1	0.0195	2.51×10^{-4}	40	1
4	0.0149	2.09×10^{-4}	155–173	1.69
9	0.0121	1.47×10^{-4}	368–414	2.91

distances used. The depth of the fringe from the Michelson with nine lines is shown as well.

To provide a calibration and to demonstrate the sucess of the method, Pietraszewski relied on detection of the Solar rotation. As well as using nine lines, he also, as a comparison, repeated it with four lines and a single line, (5281.8 Å). Rather than letting the Sun drift across the fibre he varied the telescope drive rate. Figure 6.4 shows the results, (along with the $\cos^2$ scans). Why there is a 'hump' in the nine line scans is unknown.

Table 6.7 shows the increase in sensitivity of the Michelson with increasing number of lines. As can be seen, there was an improvement in sensitivity of 2.91 times compared to the 5281.8 Å line, very close to the hoped for three times from nine lines. Even taking into account that the counts with a single line are possibly unrepresentatively low—the 5281.8 Å line being close to one of the edges of the echelle's spectrum—there appears to be an unambiguous improvement in the sensitivity of the multi-lined Michelson.

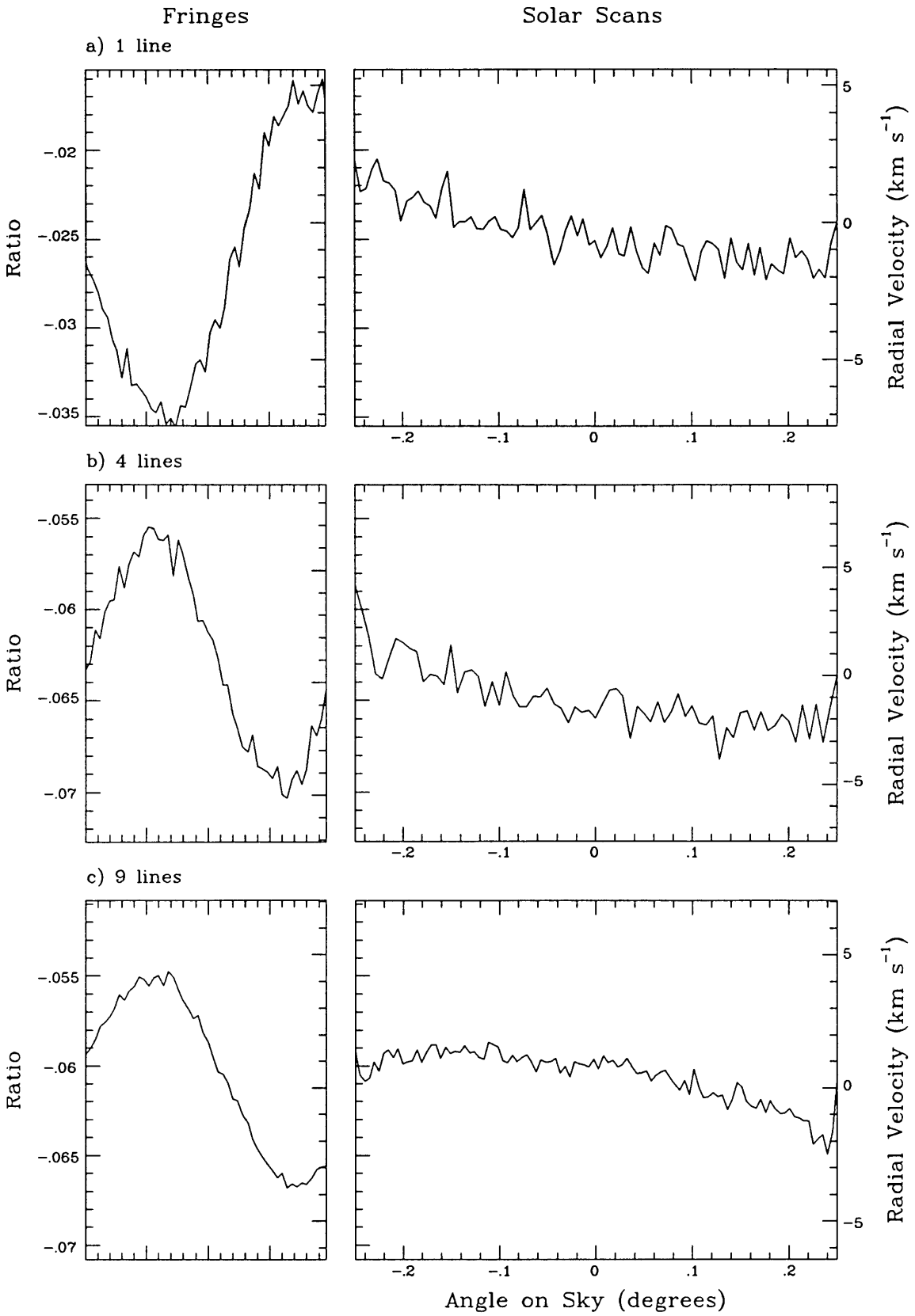


Figure 6.23: Scans across the Sun using the Michelson + $\cos^2$ fringes.

Chapter 7

Conclusions and Future Developments

The project can be divided into four sections.

1. The single-line Fabry-Perot.
2. The pre-disperser.
3. Multi-lining the Fabry-Perot.
4. Multi-lining the Michelson.

It is proposed to discuss each of these in turn.

7.1 The Single-Line Fabry-Perot

It has been shown that by the addition of an optical reference system, the CS100/etalon combination is capable of sub-metre per second stability for time periods of over an hour—an improvement of 50–100×'s the results previously obtained. Unfortunately, because it only uses a single line, this accuracy would only be attainable using the largest telescopes. The single line Fabry-Perot, however, would still be suitable for measuring radial velocity changes in hotter stars, (e.g. roAp stars). As they have only a few lines in their spectra, the potential advantage of using multiple lines is much reduced. With the extra losses in the pre-disperser of a multi-lined interferometer, any improvement could be negligible.

Apart from selecting a suitable etalon, a filter to isolate the absorption would be needed, held in a variable angle mount to allow for wavelength tuning. To eliminate

errors caused by relative movements of the two fibres, (from temperature fluctuations), a single fibre could be used. This would mean that the the reference light would have to be introduced at the telescope, using a dichroic mirror.

7.2 The Echelle Pre-Filter

It can be expected that the echelle will be more susceptible to drifts than a filter, if only because it is much larger, and hence, harder to temperature control. Paradoxically, its size will probably prove advantageous, in that it will only change temperature, (and hence, drift slowly). The echelle will also be effected by changes in pressure and humidity altering the refractive index of the air. Again, these can be expected to be slow changes. Unfortunately, in the present echelle, the only way to reduce their effects would be to introduce some form of optical reference system. Of course, the filter width can be increased by using bigger fibres. Although 1 mm diameter fibres are available, they are expensive, and particularly in the case of the Michelson, would lead to an increase in non-signal continuum, and in the Fabry-Perot, still further reduce the size of the entrance aperture useable, leading to an even larger etalon being needed.

The present pre-disperser was designed for imaging a very large spectral range onto an image tube. Consequently, each order of the spectrum had to be very short, so cross-dispersion had to be used. Gratings are available that have an inter-order distance of ≈ 400 Å at 5500 Å. Rather than going for the complication of a cross-dispersed design, (with all the alignment problems etc. that entails), it would possibly be better to use a single order from a grating with a similar specification to the above, with a broad-band filter to isolate the most suitable order.

The simplest arrangement would be to have the grating mounted in Litrow, using the same lens as both the collimator and camera. Rather than producing a collimated beam to put the broad-band filter in, an option would be to mount the filter in the telescope, just in front of the fibre. Although this is not in a parallel beam, for, say, an f11 focus, there would only be a shift of 1.5% of the passband in a 400 Å filter at 5500 Å from the edge to the centre of the beam.

As a cheaper, (and possibly more efficient), alternative a parabolic mirror could be used. Because of the geometry of the system, whilst it would be possible to make a spring strip arrangement to move the input fibre in the focal plane of the mirror, it would be much simpler to reimage the input beam onto a 45° mirror, so allowing a

much more compact mount outside the beam to be used. Advantage of this could be taken to produce a collimated beam to put the pre-filter in. Unfortunately, the output fibres would have to be in the beam, but by using a narrow mounting bar, only a small fraction of the light would be lost.

7.3 The Multi-Lined Fabry-Perot

This unfortunately, has proved to be the least successful part of the project. The count rate of the multi-lined system was only three times that of the best, (i.e. most sensitive), on-axis line and about twice the count rate of the highest count on-axis line, as opposed to the hoped for six times. Even worse, the change in ratio in the multi-line case was only a third of the best from the on-axis lines, or just under half of the best off-axis. This led to the multi-lined case being able to give only approximately half the precision of the single line etalon, (in a given time). This was because

- Variations in the sensitivity across the photomultiplier (and probably vignetting) caused a reduction in counts for off-axis lines.
- The resolution of the available etalon *on-axis* was unsuitable for use with the vast majority of the absorption lines found in the Sun, (and more or less unuseable off-axis with most of them).
- The total number of lines that could be used was further reduced by the small fraction of a Fabry-Perot order that was useable.
- Because of the high finesse in the Fabry-Perot, the fibres had to be positioned extremely accurately.

What the project *did* show is that it was possible to align fibres to give a sensitivity of approximately 70% of that expected from summing line profiles. Hence, for equal efficiencies in the echelle/Fabry-Perot compared with a filter/Fabry-Perot combination, the increase in signal-to-noise, at best, would probably be only half that theoretically available.

7.3.1 A Possible Multi-lined Fabry-Perot

The biggest problem with the current etalon is the large diameter fibres that have been used to interface it to the present pre-disperser. These were chosen so that the

Table 7.1: Possible interferometer parts of a Fabry-Perot based multi-lined system

Stellar line width	0.1 Å	0.4 Å
'Flat-top'[a]	0.25 Å	1 Å
Maximum filter width	0.5 Å	2 Å
Inter-order distance	1 Å	4 Å
Resolution of etalon	0.04 Å	0.16 Å
Finesse	25	25
Order, m, (for 5000Å)	5000	1250
Gap, d	1.25 mm	0.3125 mm
Maximum off-axis angle	1.15°	2.29°
Maximum fibre size	0.023°	0.046°
Collimator (200 μm fibres)	500 mm	250 mm
Etalon diameter, (f3 beam)	167 mm	83 mm
Max. off-axis fibre distance	10 mm	10 mm
Positioning Accuracy at edge[b]	25 μm	25 μm

[a]Based on the good image criteria from section 3.4.2.
[b]From equation 3.80 for 90% of maximum improvement. The maximum tolerance is $\approx$ 300 μm.

instrument could be (theoretically) used with the largest available telescopes. As has been argued before, it is better (and more likely) that a given number of photons are counted by observing for a long time on a small telescope than for a short time on a large telescope. This provides the justification for reducing the size of the fibres, to (say) 100 μm for the input from the telescope to the pre-disperser and 200 μm from the pre-disperser to the Fabry-Perot. Table 7.1 gives two possible etalons, suitable for 0.1 and 0.4 Å line width stars.

7.4 The Multi-lined Michelson

This has proven to be the interferometer that has been by far the easiest to multi-line. Because of the linear change in phase and the large input aperture produced by field widening there were no restrictions on which wavelengths could be selected. The above, combined with the $\cos^2$ fringes from the Michelson meant that there was an extremely wide tolerance for positioning the fibres. Also, as the Michelson has the correct resolution for use with the Sun, it has given an unambiguous improvement in signal to noise, with a gain approaching that expected. As an added bonus, it automatically has a gain of $\sqrt{2}$ over the Fabry-Perot, as both sides of the 'line' are

observed simultaneously.

There has been no detailed study of the noise levels achievable with the multi-lined Michelson, (at least as described above). The single line Michelson, however, had previously given noise levels of below 20 $cm\,s^{-1}$. The major difference between the multi-lined Michelson and the original version are:

- The introduction of multiple fibres in the input aperture.
- The replacement of the 1.5 Å pre-filter with the echelle.

As there were no alteration necessary for the current Michelson to be able to use multiple lines, (because of the fortuitous accidental existence of the correct phase shift across the entrance aperture in the single line version), the noise levels should be very similar to those obtained previously. The only extra source of noise is the possibility of the fibres drifting with respect to one another, because of variations in temperature. As the input aperture plate is small, it should be easy to temperature stabilize.

The one big disadvantage of the Michelson over the Fabry-Perot, is for a given resolution, it has a much larger 'filter profile', equal to the full pre-filter width. If a large number of lines are used on a bright star, (a 0 m star, with a 2 m telescope and 25 lines using a similar passband to the present system and an efficiency of 1%), count rates of $\approx$ 6 MHz per channel could be obtained. These would cause non-linearities in the photon counting system. For use under these conditions some form of analogue system might have to be used.

The Michelson is very suitable for multi-lined radial velocity measurements as it stands. For improved stability instead of using a cadmium lamp, some form of stabilized laser is needed. Long term drifts could be reduced by the introduction of temperature stabilization. In the 'nice to have' section, eliminating hysteresis in the positioning of the moveable cube corner by the use of capacitance micrometry would allow, by rapid scanning, the 'line profile' to be measured more accurately. (Even though both beams are observed simultaneously, the differing non-linearities of the two channels lead to variations in measured radial velocities with count rate.)

7.5 Conclusion

It has been demonstrated that a field-widened Michelson is very suitable for modification to use multiple lines. The present Fabry-Perot *ISOS* has not been multi-lined

successfully; this was because it had the wrong resolution for use with the Sun and it was not large enough to be able to go off-axis for a full order, hence use all the available lines. It is possible to devise a Fabry-Perot based system which, on paper, could be used with multiple lines, (particularly for stars with greater line widths than the Sun), and the project has demonstrated that the fibres can be positioned to the required degree of accuracy. Compared to the Michelson, however, the Fabry-Perot is much more difficult to multi-line successfully, and as the problems in the Michelson have been largely solved, continuing with the Fabry-Perot seems to be of questionable value.

In conclusion, to find Solar-type oscillations in other stars, a method of measuring radial velocities on small telescopes to better than 15 $\mathrm{cm\,s^{-1}}$ is needed. Currently, the best option for this appears to be a multi-lined Michelson interferometer.

Appendix A

Field-Widening the Michelson Interferometer

In conventional interferometers, (and spectrometers), there is a rapid decrease in resolution with increasing off-axis angle—-the resolution/luminosity product, RL. By using more complicated optics in the Michelson Interferometer, it is possible to produce a much greater than usual RL product [107].

In a classical Michelson, when the image of one reflector is superimposed on the other, the path difference is identical for all possible rays. When one of the mirrors is displaced, a variation in path difference with angle appears. By introducing optical elements into the system, which allow the image of one of the reflectors to be superimposed on the other, the changes in path difference with angle can be much reduced, so leading to a greatly increased RL product. This is known as *field-widening* or, alternatively, *field-compensation.*

Consider a solid Michelson interferometer which has a small air gap in one of the beams. The path difference is then

$$\Delta = nAB + nBC + nCD + nDH - AG - nGK - nKL - LI - IF. \qquad \text{(A.1)}$$

For the two images to be superimposed, the output ray from one mirror must lie on top of the other, i.e. $IH = 0$, hence, $IF = 0$. This gives, (after simplification),

$$\Delta = 2[e(n\cos i - \cos r) + nd\cos i]. \qquad \text{(A.2)}$$

By expanding the cosines and using the approximations $i \approx \sin i$ and $r \approx \sin r$, and equating the terms in $\sin^2 i$ to zero,

$$d = e(n-1) \qquad \text{(A.3)}$$

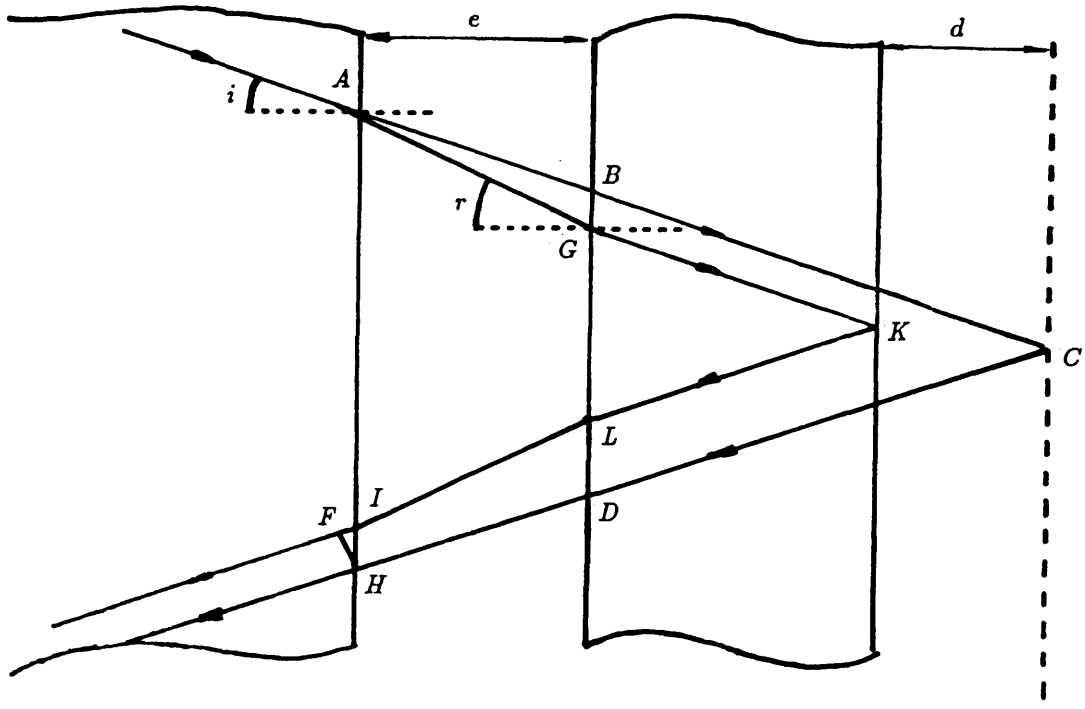


Figure A.1: Condition for field-widening

can be obtained. Substituting this in

$$\Delta_0 = 2[e(n-1) + nd], \tag{A.4}$$

the on-axis path difference, leads to an air gap of

$$e = \frac{\Delta_0}{2(n^2-1)} \tag{A.5}$$

and a value for the extra thickness of glass of

$$d = \frac{\Delta_0}{2(n+1)}. \tag{A.6}$$

Appendix B

Discussion on the Detection of the 5-minute Oscillation

Both of the plots given in figures 6.20 and 6.21 were obtained by using a 200 μm fibre to collect light from a $\approx$ 17 mm diameter image of the Sun. Consequently they were integrated over a disc of diameter 22″, which is equivalent to $\approx$ 1% of the Sun's diameter.

B.1 Expected Results

The global 5-minute oscillation's frequency spectrum normally presented in the literature is obtained from long integrations over several months. Consequently the spectrum consists of well resolved peaks, forming an approximately 1.5 mHz bandwidth comb, with maximum power at $\approx$ 3.3 mHz. For results collected over short integration periods of a few hours however, the structure in the frequency spectrum is not resolved. If many such short integration period frequency spectra were simply added together and averaged, the envelope of the power distribution in the oscillations would be obtained. This technique was used by Fossat and Ricort [8] in obtaining their results with different sized areas on the Sun, and for their 22″ diameter disc they found an r.m.s. amplitude of 133 ± 14 m s^{-1}. Without averaging, as is demonstrated by Christensen-Dalsgaard and Gough [52] for the whole Sun, the resultant power spectra are dominated by a few peaks in each (short) run. These results of Christensen-Dalsgaard and Gough should hold equally well for short runs on small areas of the Sun, and consequently, it can be expected that the frequency spectra which should have been obtained would consist of a series of 'random' peaks, decaying in average amplitude either size of 3.3 mHz.

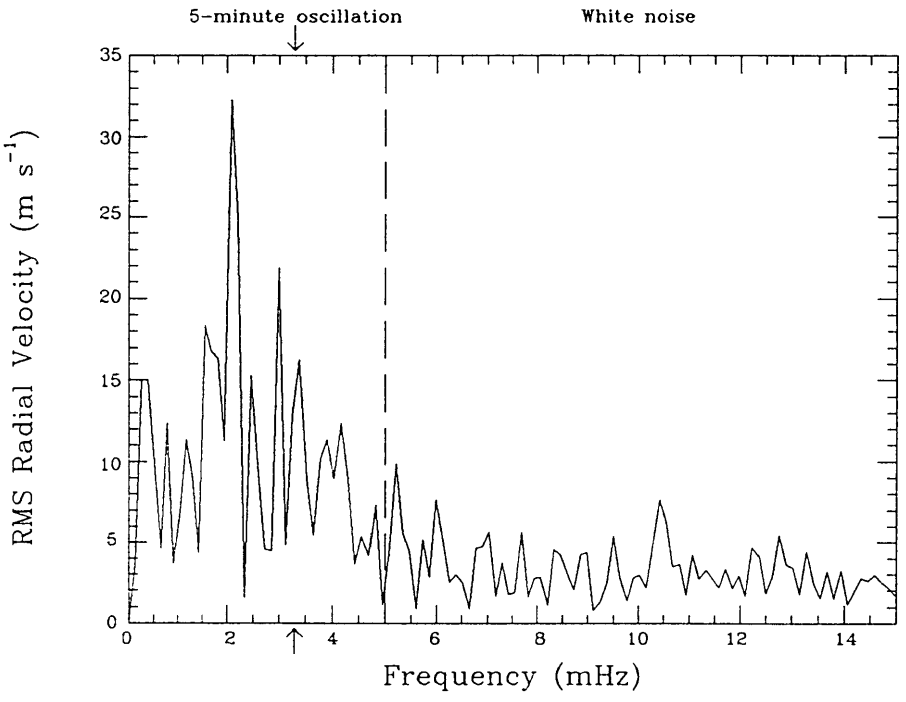


Figure B.1: Data from figure 6.20.

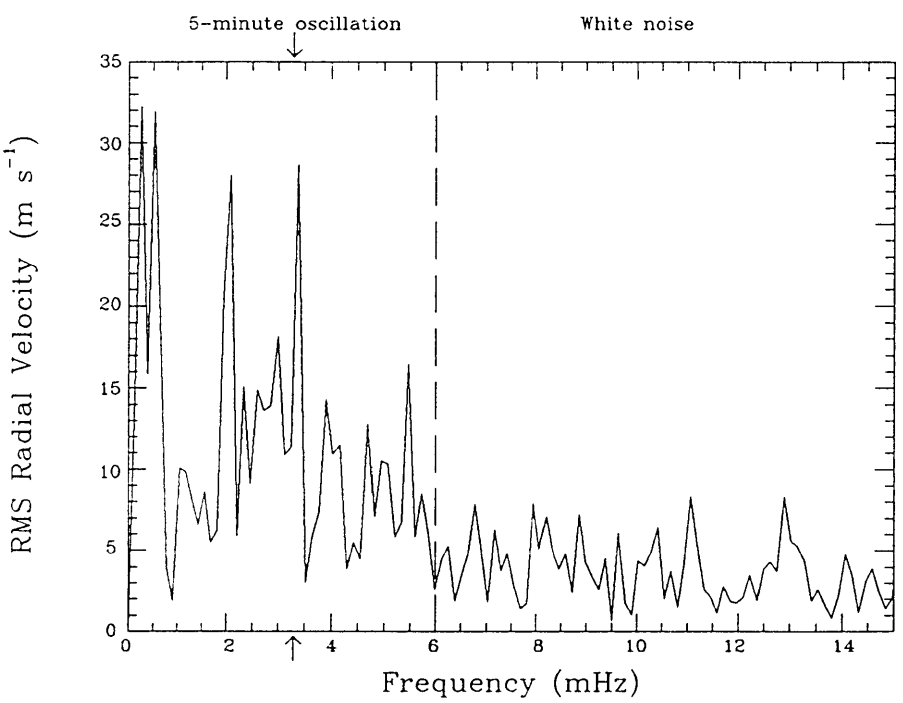


Figure B.2: Data from figure 6.21.

B.2 Results Obtained

Both plots can be divided by inspection into two parts, at around 5 mHz for figure 6.20 and 6 mHz for figure 6.21. For frequencies above the divide, the 'signal' appears to consist of 'white noise' which is presumably dominated by photon statistics. In both of the frequency spectra this is approximately 2.5 $\mathrm{m\,s^{-1}}$, which is similar to the predicted 2 $\mathrm{m\,s^{-1}}$, (predicted from the number of photons). For frequencies below the divide, there is an increase in the amplitude of the 'signal', with a peak value in both cases of $\approx 30\ \mathrm{m\,s^{-1}}$. Whilst some of this increase in amplitude is in the expected frequency region for the 5-minute oscillation, ($\approx$ 2.5–4.0 mHz), there are also large amplitude peaks which are outside this region. If it is accepted that the 'signal' in the 3.3 mHz region is a manifestation of the 5-minute oscillation, one possible explanation for these might be that they are being caused by errors in guiding, (the telescope drive was relied on, with only erratic periodic corrections frequency determined by difficult operating conditions), because then the telescope pointing would drift across regions containing many different modes. This would also explain why the signal is smaller than that found by Fossat and Ricort. For diameters of 5% that of the Sun's disc they obtained $38 \pm 4.5\ \mathrm{m\,s^{-1}}$ and for 10% they obtained $21.8 \pm 1.8\ \mathrm{m\,s^{-1}}$.

Finally, the low frequency peaks in figure 6.21 at approximately 0.5 mHz are I believe the remains of the slope in the data, (which had been previously removed), caused by instability in the pre-disperser. The instability is most likely to be thermal in origin, particularly in view of the fact that this part of the equipment was not insulated.

Bibliography

[1] Unno, W., Osaki, Y., Ando, H., Shibahashi, H. 1979, *Nonradial Oscillations of Stars*, University of Tokyo Press.

[2] Lesh, J. R., Morris, L.A. 1978, The observational status of the β Cephei stars, in *Annu. Rev. Astron. Astrophys.*, ed. G. Burbridge, Annual Review Inc., Pallo Alto, Ca., p. 215.

[3] Christensen-Dalsgaard, J. 1984, What will asteroseismology teach us?, in *Space Research Prospects in Stellar Activity and Variability*, ed. A. Mangeney and F. Praderie, Observatoire de Paris, Meudon, p. 11.

[4] Leighton, R. B., Noyes, R. W., Simon, G. W. 1962, Velocity fields in the Solar atmosphere. I. Preliminary report, *Astrophys. J.*, **135**, 474.

[5] Ulrich, R. K. 1970, The five-minute oscillation on the Solar surface, *Astrophys. J.*, **162**, 933

[6] Leibacher, J. W., Stein, R. F., 1971, A new description of the Solar five-minute oscillation, *Astrophys. Letters*, **7**, 191.

[7] Deubner, F.-L., 1975, Observations of low wavenumber nonradial eigenmodes of the Sun, *Astron. Astrophys.*, **44**, 191.

[8] Fossat, E., Ricort, G. 1975, Photospheric oscillations. 1. Large scale observations by optical resonance method, *Astron. Astrophys.*, **43**, 243.

[9] Brookes, J. R., Isaak, G. R., van der Raay, H. B., 1976, Observations of free oscillations of the Sun, *Nature*, **259**, 92.

[10] Brookes, J. R., Isaak, G. R., van der Raay, H. B., 1978, A resonant-scattering Solar spectrometer, *Mon. Not. R. astron. Soc.*, **185**, 1.

[11] Severny, A. B., Kotov, V. A., Tsap, T. T. 1976, Observations of Solar Pulsations, *Nature*, **259**, 87.

[12] Scherrer, P. H., 1980, Further evidence of Solar oscillations with a period of 160 minutes, *Astrophys. J., Lett.*, **237**, L97.

[13] van der Raay, H. B. 1988, Long period Solar oscillations, in *Seismology of the Sun and Sun-like stars*, ESA SP–286, ed. E. J. Rolfe, ESA Publications Division, Noordwijk, p. 339.

[14] Claverie, A., Isaak, G. R., McLeod, C. P., van der Raay, H. B., Roca Cortés, T. 1979, Solar structure from global studies of the 5-minute oscillation, *Nature*, **282**, 591.

[15] Gough, D. 1987, Seismological measurement of stellar ages, *Nature*, **326**, 257.

[16] Christensen-Dalsgaard, J. 1988, An overview of Helio- and asteroseismology, in *Advances in Helio- and Asteroseismology*, IAU Symp. 123, ed. J. Christensen-Dalsgaard and S. Frandsen, D. Reidel, Dordrecht, p. 3.

[17] Gough, D. 1985, Beginnings of asteroseismology, *Nature*, **314**, 14.

[18] Kurtz, D. W. 1986, A review of the rapidly oscillating Ap stars, in *Seismology of the Sun and the Distant Stars*, ed. D. O. Gough, D.Reidel, Dordrecht, p. 417.

[19] Matthews, J. M., Wehlau, W. H., Walker, G. A. H., Yang, S. 1988, Detection of radial velocity variations on the rapidly oscillating Ap star HR 1217, *Astrophys. J.*, **324**, 1099.

[20] Leeper, M., Bell, C. R., Pietraszewski, K. A. R. B., Renton, R. E., Belmonte, J. A., Pallé, P. L., Roca Cortés, T. 1988, The search for radial velocity variations in rapidly oscillating Ap stars using the Fabry-Perot interferometric stellar oscillation spectrometer *(FP-ISOS)*, in *Seismology of the Sun and Sun-like stars*, ESA SP–286, ed. E. J. Rolfe, ESA Publications Division, Noordwijk, p. 587.

[21] Belmonte, J. A., Pallé, P. L., Roca Cortés, T. Bell, C. R., Leeper, M., Pietraszewski, K. A. R. B., Renton, R. E., 1988, Search for radial velocity variations in rapidly oscillating Ap stars using the Fabry-Perot interferometric stellar oscillation spectrometer, *Astron. Astrophys.*, accepted.

[22] Bell, C. R., Leeper, M., Pietraszewski, K. A. R. B. 1988, A Fabry-Perot interferometric stellar oscillation spectrometer, in *Seismology of the Sun and Sun-like stars*, ESA SP–286, ed. E. J. Rolfe, ESA Publications Division, Noordwijk, p. 613.

[23] Libbrecht, K. G. 1988, Radial velocity observations reveal multimode oscillations in Gamma Equulei, *Astrophys. J., Lett.*, **330**, L51.

[24] Scargle, J. D. 1982, Studies in astronomical time series analysis. II. Statistical aspects of spectral analysis of unevenly spaced data, *Astrophys. J.*, **263**, 835.

[25] Fossat, E. 1984, Stellar seismology: five-minute p-modes detected on Alpha Centauri, *Messenger*, **No. 36**, 20.

[26] Noyes, R. W., Baliunas, S. L., Belsrene, E., Duncan, D. K., Horne, J., Widrow, L. 1984, Evidence for global oscillations in the K2 dwarf Epsilon Eridani, *Astrophys. J., Lett.*, **285**, L23.

[27] Gelly, B., Grec, G., Fossat, E. 1988, Evidence for global pressure oscillations in Procyon and α Centauri, in *Advances in Helio- and Asteroseismology*, IAU Symp. 123, ed. J. Christensen-Dalsgaard and S. Frandsen, D. Reidel, Dordrecht, p. 249.

[28] Gelly, B., Grec, G., Fossat, E. 1986, Evidence for global pressure oscillations in Procyon and α Centauri, *Astron. Astrophys.*, **164**, 383.

[29] Guenther, D. B., Demarque, P. 1985, The stelar seismology of ϵ Eridani, *Astrophys. J.*, **301**, 207.

[30] Guenther, D. B. 1987, A discussion of Epsilon Eridani's age, composition and oscillation frequencies, *Astrophys. J.*, **312**, 211.

[31] Guenther, D. B. 1988, Stellar models of ϵ Eridani constrained by stellar seismology, in *Advances in Helio- and Asteroseismology*, IAU Symp. 123, ed. J. Christensen-Dalsgaard and S. Frandsen, D. Reidel, Dordrecht, p. 285.

[32] Soderblom, D., Däppen, W. 1988, Modeling the global oscillations of Epsilon Eridani, in *Advances in Helio- and Asteroseismology*, IAU Symp. 123, ed. J. Christensen-Dalsgaard and S. Frandsen, D. Reidel, Dordrecht, p. 281.

[33] Däppen, W., Soderblom, D. 1988, Epsilon Eridani revisited, in *Seismology of the Sun and Sun-like stars*, ESA SP–286, ed. E. J. Rolfe, ESA Publications Division, Noordwijk, p. 653.

[34] Soderblom, D., Däppen, W. 1988, Modeling Epsilon Eridani and its oscillations, *Astrophys. J.*, **342**, 945.

[35] Christensen-Dalsgaard, J., Frandsen, S. 1983, Stellar 5 min oscillations, *Sol. Phys.*, **82**, 469.

[36] Lang, K. R. 1980, *Astrophysical Formulae*, Springe Verlag, Berlin.

[37] Baliunas, S. L., Hartmann, L., Vaughan, A. H., Liller, W., Duprec, A. K. 1981, Short time-scale variability of chromospheric Ca II in late type stars, *Astrophys. J.*, **246**, 473.

[38] Schmider, F. X., Fossat, E., Grec, G., Gelly, G. 1988, The Nice university stellar seismometer, in *Seismology of the Sun and Sun-like stars*, ESA SP–286, ed. E. J. Rolfe, ESA Publications Division, Noordwijk, p. 605.

[39] Innis, J. L., Isaak, G. R. 1988, High precision velocity measurements of Procyon using the 7699 Å line of potassium, in *Seismology of the Sun and Sun-like stars*, ESA SP–286, ed. E. J. Rolfe, ESA Publications Division, Noordwijk, p. 583.

[40] Demarque, P., Guenther, D. B., van Altena, W. F. 1986, The case of α Centauri: mass age and p-mode oscillation spectrum, *Astrophys. J.*, **300**, 773.

[41] Demarque, P., Guenther, D. B. 1988, Internal constitution and oscillation spectrum of Procyon, in *Advances in Helio- and Asteroseismology*, IAU Symp. 123, ed. J. Christensen-Dalsgaard and S. Frandsen, D. Reidel, Dordrecht, p. 287.

[42] Libbrecht, K. G. 1988, A search for radial velocity oscillations in Procyon, in *The Impact of Very High S/N Spectroscopy on Stellar Physics*, IAU Symp. 132, ed. G. Cayrel de Strobel and M. Spite, Kluwer Academic Publishers, Dordrecht, p. 83.

[43] Loumos, G. L., Deeming, T. J. 1978, Spurious results from Fourier analysis of data with closely spaced frequencies, *Astrophys. and Space Sci.*, **56**, 285.

[44] Grec, G., Fossat, E., Pomerantz, M. 1980, Solar oscillations: full disk observations from the geographic South Pole, *Nature*, **288**, 541.

[45] Claverie, A., Isaak, G. R., McLeod, C. P., van der Raay, Pallé, P. L., Roca Cortés, T. 1984, Continuous observations of Solar oscillations from two suitably spaced ground stations, *Mem. Soc. Astron. Ital.*, **55**, 63.

[46] Elsworth, Y. P., Isaak, G. R., Jeffries, S. M., McLeod, C. P., New, R., van der Raay, H. B., Pallé, P. L., Regulo, C., Roca Cortés, T. 1988, Experience in operating a limited global network of stations measuring full-disc oscillations of the Sun, in *Advances in Helio- and Asteroseismology*, IAU Symp. 123, ed. J. Christensen-Dalsgaard and S. Frandsen, D. Reidel, Dordrecht, p. 535.

[47] Aindow, A., Elsworth, Y. P., Isaak, G. R., Mcleod, C. P., New, R., van der Raay, H. B. 1988, The current status of the Birmingham Solar seismology network, in *Seismology of the Sun and Sun-like stars*, ESA SP–286, ed. E. J. Rolfe, ESA Publications Division, Noordwijk, p. 157.

[48] Fossat, E. 1988, I.R.I.S.: a network for full disk Helioseismology, in *Seismology of the Sun and Sun-like stars*, ESA SP–286, ed. E. J. Rolfe, ESA Publications Division, Noordwijk, p. 161.

[49] Harvey, J., *et al.* 1988, The *GONG* instrument, in *Seismology of the Sun and Sun-like stars*, ESA SP–286, ed. E. J. Rolfe, ESA Publications Division, Noordwijk, p. 203.

[50] Hill, F., *et al.* 1988, The *GONG* site survey, in *Seismology of the Sun and Sun-like stars*, ESA SP–286, ed. E. J. Rolfe, ESA Publications Division, Noordwijk, p. 209.

[51] Pintar, J. A., *et al.* 1988, The *GONG* data reduction and analysis system, in *Seismology of the Sun and Sun-like stars*, ESA SP–286, ed. E. J. Rolfe, ESA Publications Division, Noordwijk, p. 653.

[52] Christensen-Dalsgaard, J., Gough, D. O. 1982, On the interpretation of five-minute oscillations in Solar spectrum line shifts, *Mon. Not. R. astr. Soc.*, **198**, 141.

[53] Harvey, J. W. 1988, Techniques for observing stellar oscillations, in *Advances in Helio- and Asteroseismology*, IAU Symp. 123, ed. J. Christensen-Dalsgaard and S. Frandsen, D. Reidel, Dordrecht, p. 497.

[54] Woodard, M., Hudson, H. S. 1983, Frequencies, amplitudes and linewidths of Solar oscillations from total irradiance observations, *Nature*, **305**, 589.

[55] Taylor, J. 1806, The Star, *Rhymes for the Nursery.*

[56] Warner, B. 1988, *High Speed Astronomical Photometry*, Cambridge Astrophysics Series, Cambridge University Press, Cambridge.

[57] Fossat, E. 1984, Should one measure radial velocity or brightness fluctuations?, in *Space Research Prospects in Stellar Activity and Variability*, ed. A. Mangeney and F. Praderie, Observatoire de Paris, Meudon, p. 77.

[58] Fossat, E. 1985, Atmospheric limitations in stellar seismology. Should one measure radial velocity or brightness fluctuations?, in *Proc. of the Workshop on Improvements to Photometry*, NASA CP–2350, ed. W. J. Borucki and A. Young, NASA Conf. Publ., p. 68.

[59] Kurtz, D. W. 1985, The ground based photometric limitations to the search for light variations due to the 5-minute Solar-type oscillations in other stars, in *Proc. of the Workshop on Improvements to Photometry*, NASA CP–2350, ed. W. J. Borucki and A. Young, NASA Conf. Publ., p. 56.

[60] Frandsen, S. 1987, An upper limit on p-mode amplitudes in β Hyi, *Astron. Astrophys.*, **181**, 289.

[61] Griffin, R. F. 1967, A photoelectric radial-velocity spectrometer, *Astrophys. J.*, **148**, 465.

[62] Baranne, A., Mayor, M., Poncet, J. L. 1979, Coravel—a new tool for radial velocity measurement, *Vistas. Astron.*, **23**, 279.

[63] Griffin, R. and R. 1973, On the possibility of determining stellar radial velocities to 0.01 $\mathrm{km\,s^{-1}}$, *Mon. Not. R. astr. Soc.*, **162**, 243.

[64] Smith, M.A. 1982, Precise radial velocities. I. A preliminary search for oscillations in Arcturus, *Astrophys. J.*, **253**, 727.

[65] Campbell, B., Walker, G. A. H. 1984, Stellar radial velocities of high precision—techniques and results, in *Stellar Radial Velocities*, IAU colloq. 88, ed. A. G. D. Philip and D. W. Latham, L. Davis Press, Schenectady, N. Y., p. 5.

[66] Isaak, G. R. 1961, An atomic beam spectrophotometer, *Nature*, **189**, 373.

[67] Fossat, E., Rodier, F. 1971, A sodium experiment for photospheric velocity field observations, *Solar Physics*, **18**, 204.

[68] Cimino, M., Cacciani, A., Sopranzi, N. 1968, An instrument to measure Solar magnetic fields by an atomic-beam method, *Sol. Phys.*, **3**, 618.

[69] Isaak, G. R., Jones, A. R. 1988, A spectroscopic search for oscillations in the 769.9 nm potassium line of Procyon, in *Advances in Helio- and Asteroseismology*, IAU Symp. 123, ed. J. Christensen-Dalsgaard and S. Frandsen, D. Reidel, Dordrecht, p. 255.

[70] High precision observations of Arcturus using the 7699 Å line of potassium, in *Seismology of the Sun and Sun-like stars*, ESA SP–286, ed. E. J. Rolfe, ESA Publications Division, Noordwijk, p. 569.

[71] Isaak, G. R., Jones, A. R. 1988, Continuous magnetic calibration of (velocity) sensitivity of oscillation spectrometers, in *Advances in Helio- and Asteroseismology*, IAU Symp. 123, ed. J. Christensen-Dalsgaard and S. Frandsen, D. Reidel, Dordrecht, p. 467.

[72] Cacciani, A., Catalano, S., Rodonó, M., Costa, G. 1988, A prototype photometer for magnetic field and Doppler measurements, in *Seismology of the Sun and Sun-like stars*, ESA SP–286, ed. E. J. Rolfe, ESA Publications Division, Noordwijk, p. 601.

[73] Traub, W. A., Mariska, J. T., Carleton, N. P. 1978, A search for stellar oscillations, *Astrophys. J.*, **223**, 583.

[74] Hegyi, D. J., Traub, W. A., Carleton, N. P. 1972, Cosmic background radiation at 1.32 mm, *Phys. Rev. Lett.*, **28**, 1541.

[75] Forrest, A. K. 1982, *An interferometric stellar oscillation spectrometer*, Ph.D. thesis, Univ. of London.

[76] Forrest, A. K. 1984, Ultra high resolution radial velocity spectrometer, in *Instrumentation in Astronomy V*, Proc. SPIE 445, ed. A. Boksenberg and D. L. Crawford, p. 543.

[77] Pietraszewski, K. A. R. B., Ring, J., Forrest, A. K. 1986, Interferometric stellar oscillation spectrometry, in *Seismology of the Sun and the Distant Stars*, ed. D. O. Gough, D.Reidel, Dordrecht, p. 391.

[78] Pietraszewski, K. A. R. B. 1984, *Studies of stellar oscillations using a Fabry-Perot interferometer*, Ph.D. thesis, Univ. of London.

[79] Pietraszewski, K. A. R. B., Reay, N. K., Ring, J. 1986, A new Fabry-Perot radial velocity spectrometer, in *Seismology of the Sun and the Distant Stars*, ed. D. O. Gough, D.Reidel, Dordrecht, p. 377.

[80] Bevington, P. R. 1969, *Data Reduction and Error Analysis for the Physical Sciences*, McGraw-Hill Book Company, New York.

[81] Zambeck, M. V. 1982, *Handbook of Space, Astronomy and Astrophysics*, Cambridge.

[82] Allen, C. W. 1976, *Astrophysical Quantities*, The Athlone Press, London.

[83] Butcher, H. R., Hicks, T. R. 1986, A Fabry-Perot based stellar seismometer, in *Seismology of the Sun and the Distant Stars*, ed. D. O. Gough, D. Reidel Publishing Company, Dordrecht, Holland, p. 347.

[84] Jaquinot, P. 1954, The luminosity of spectrometers with prisms, gratings, or Fabry-Perot Etalons, *J. Opt. Soc. Am.*, 44, 761.

[85] Vaughan, A. H., Jr. 1967, Astronomical Fabry-Perot Interference Spectroscopy, in *Annu. Rev. Astro. Astrophys.*, Vol. 5, ed. L. Goldberd, Annual Review Inc., Palo Alto, Ca., p. 139.

[86] Longhurst, R.S. 1973, *Geometrical and Physical Optics*, Longman, London and New York.

[87] Hill, J. M., Angel, J. R. P. 1984, Optical matching for fiber optic spectroscopy, in *Instrumentation in Astronomy V*, Proc. SPIE 445, ed. A. Boksenberg and D. L. Crawford, p. 85.

[88] Powell, J. R. 1984, Application of optical fibres to astronomical instrumentation, in *Instrumentation in Astronomy V*, Proc. SPIE 445, ed. A. Boksenberg and D. L. Crawford, p. 77.

[89] Heacox W.D. 1980, An optical fibre spectrograph coupler, in *Optical and Infra-red Telescopes for the 1990s*, Vol. II, ed. A. Hewitt, p. 702.

[90] Gray, P. M. 1984, Fibre optic coupled aperture plate (FOCAP) system at the AAO, in *Instrumentation in Astronomy V*, Proc. SPIE 445, ed. A. Boksenberg and D. L. Crawford, p. 57.

[91] Enard, D., Lund, G., Tarenghi, M. 1983, Fiber optics at ESO. Part 2: Fiber optics multiple object spectroscopy at the 3.6 m telescope, *Messenger*, **No. 33**, 32.

[92] Learner, R. C. M. 1972, Echelle grating spectrometer, in *Auxiliary Instrumentation for Large Telescopes*, ed. S. Lausten and A. Reiz, p. 131.

[93] Walraven, T. and J. H. 1972, Some features of the Leiden radial velocity instrument, in *Auxiliary Instrumentation for Large Telescopes*, ed. S. Lausten and A. Reiz, p. 175.

[94] Jones, R. V. 1951, Parallel and rectilinear spring movements, *Journal of Scientific Instruments*, **28**, 38.

[95] Jones, R. V. 1956, Some parasitic deflexions in parallel spring movements, *Journal of Scientific Instruments*, **33**, 11.

[96] Minnaert, M., Mulders, G., Houtgast, J. 1940, *Photometric Atlas of the Solar Spectrum from λ 3612 to λ 8771*, Sterrewacht Sonnenborgh, Utrecht.

[97] Pierce, A. K., Breckinridge, J. B. 1973, *The Kitt peak table of Photographic Solar Spectrum Wavelengths*, Kitt Peak National Observatory, Arizona.

[98] East, I. R. 1983, *Doppler-Shifts in the Spectrum of the Zodiacal Light*, Ph.D. thesis, University of London.

[99] Queensgate Instruments Ltd. 1981, *Stability Tests on the CS100 Stabilization System*, Internal report

[100] Layer, H. P. 1980, A portable iodine stabilized helium-neon laser, *IEEE Trans. Instrum. Meas.*, **IM29**, 358.

[101] Leventhal, L. A., Saville W. 1982, *6502 Assembly Language Subroutines*, Osborne/McGraw-Hill, Berkley, Ca.

[102] Niebauer, T. M., Faller, J. E., Goodwin, H. M., Hall, J. L., Barger, R. L. 1988, Frequency stability measurements on polarization-stabilized He-Ne lasers, *Appl. Opt.*, **27**, 1285.

[103] Analog Devices, 1982, *CMOS 12-bit Monolithic Multiplying DAC*, **AD7541**.

[104] Clayton, C. A. 1989, The implications of image scrambling and focal ratio degradation in fibre optics on the design of astronomical instrumentation, *Astron. Astrophys.*, **213**, 502.

[105] Tennent, R. M. 1976, *Science Data Book*, Oliver and Boyd, Edinburgh.

[106] Pietraszewski, K. A. R. B., Bell, C. R., Ring, J., Reay, N. K., Leeper, M. 1988, Multiplexed interferometric stellar oscillation spectrometry—*MISOS*, in *Advances in Helio- and Asteroseismology*, IAU Symp. 123, ed. J. Christensen-Dalsgaard and S. Frandsen, D. Reidel, Dordrecht, p. 517.

[107] Ring, J., Schofield, J. W. 1972, Field-compensated Michelson spectrometers, *Appl. Opt.*, **11**, 507.